Università degli Studi di Torino
Scuola di Dottorato in Scienza ed Alta Tecnologia

PHD THESIS

Study of muon bundles from extensive air showers with ALICE detector at the LHC

Katherin Shtejer Diaz

Advisors: Dr. Bruno Alessandro, Prof. Massimo Masera

External reviewer: Prof. Nicola Giglietto

Tesi di Dottorato di Ricerca in Scienza ed Alta Tecnologia
Indirizzo di Fisica ed Astrofisica
Academic years: 2013 – 2015
Ciclo XXVIII

To my mother Nury

To the memory of my father Guennady

To Emilio

Abstract

The ALICE experiment was mainly designed to study a new phase of matter, the Quark-Gluon-Plasma (QGP), created in ultra-relativistic heavy-ion collisions. It is one of the four large experiments at the CERN Large Hadron Collider (LHC), located in a cavern 52 meters underground with 28 meters of overburden rock. This specific underground location and the excellent tracking capability of the ALICE Time Projection Chamber (TPC) have been the cornerstone for a long term program of cosmic ray physics.

Between 2010 and 2013, during pauses in collider operations when there was no beam circulating in the LHC, ALICE collected approximately 22.6 million events with at least one reconstructed muon in the TPC, being these muons a component of the extensive air showers (EAS) created by cosmic ray interactions in the upper atmosphere. The total accumulated live time was 30.8 days.

In this thesis, the muon multiplicity distribution was measured and compared with predictions from modern Monte Carlo models. A special attention was dedicated to the study of high multiplicity events, containing more than 100 reconstructed muons, and corresponding to a muon areal density $\rho_\mu > 5.9 \pm 0.4\ \mathrm{m}^{-2}$. Similar events were studied in previous underground experiments, comprised also of accelerator based detectors, such as ALEPH and DELPHI during the LEP era. While these experiments were able to reproduce the measured muon multiplicity distribution with Monte Carlo simulations at low and intermediate multiplicities, their simulations failed to describe the frequency of the highest multiplicity events.

The results of this thesis demonstrated that multi-muon events collected

in ALICE are due to primary cosmic rays with mixed composition and energies above 10^{14} eV, where the average mass of the primary cosmic rays increases at larger energies. Additionally, the high multiplicity events observed in ALICE stem from primary cosmic rays with energies above 10^{16} eV. Our results successfully described the frequency of these events by assuming a heavy mass composition of primary cosmic rays in this energy range.

The development of the resulting air showers was simulated using the latest versions of QGSJET (QGSJET II-03 and QGSJET II-04) to model hadronic interactions. The predictions of QGSJET II-04, whose parameters were tuned using the early LHC data, reproduced better the measured rate of the high multiplicity events.

The reliability of the ALICE experiment to collect cosmic ray data, and to explain them with Monte Carlo simulations using the latest hadronic interaction models, is confirmed by this study. In particular, for the first time, the rate of high muon multiplicity events has been reproduced using conventional models. This result puts stringent limits on alternative, more exotic, and non-conventional muon production mechanisms.

Contents

1 Introduction

ALICE (A Large Ion Collider Experiment) [1] was designed to study Quark-Gluon-Plasma formation in ultra-relativistic heavy-ion collisions at the CERN Large Hadron Collider. The QGP is a high temperature and high density phase of strongly interacting matter, predicted by quantum chromodynamics (QCD) and whose existence is now firmly established experimentally [2]. Although its main purpose is to explore the properties of the QGP, the ALICE spectrometer has been also used to perform studies of relevance in cosmic-ray physics.

The ALICE location at 52 meters underground with 28 meters of overburden rock, results very convenient to measure muons produced by cosmic ray interactions in the atmosphere. During pauses in collider operations when there was no beam circulating in the LHC, ALICE undertook a programme of cosmic ray data taking between 2010 and 2013, taking advantage of the large size and excellent tracking capability of its Time Projection Chamber [3]. The total accumulated run time amounted to 30.8 days, resulting in approximately 22.6 million events with at least one reconstructed muon in the ALICE TPC.

Cosmic ray muons are created in Extensive Air Showers (EAS) following the interaction of cosmic ray primaries (protons and heavier nuclei) with nuclei of the upper atmosphere. Primary cosmic rays span a broad energy range, from approximately 10^9 eV to about 10^{21} eV. At energies lower than 10^{15} eV, the high flux of cosmic rays can be measured directly at different altitudes of the atmosphere. At energies in the range $10^{14} < E < 10^{21}$ eV, where direct measurements are no longer possible, larger detector areas are needed to achieve reasonable statistics. These indirect measurements detect secondary particles produced in EAS. In this thesis we will cover indirect measurements since ALICE detects the muonic component of EAS at energies around 10^{15} eV.

Several experiments have been devoted to study the EAS development through the detection of its components. Many of them such as large-area detector arrays at ground level [4–6] and underground facilities [7–9] perform

indirect measurements of cosmic rays at energies in the knee region ($E \sim 10^{15}$ eV), while others study cosmic rays at energies well above the knee, covering the ultra-energetic cosmic rays [10–13].

The study of the mass composition and the energy spectrum of primary cosmic rays around and above the knee is crucial to explore the sources of cosmic rays arriving at the Earth. Although the composition of primary cosmic rays around this energy is a mixture of many species of nuclei in a ratio that is not well known, measurements indicate that a notable change of the chemical composition takes place at this energy, favouring heavier components as the energy of primary particles increases.

In the spite of their small size, compared with the standard cosmic-ray experiments, the use of underground accelerator-based detectors to study the high-energy muonic component of the EAS becomes a promising opportunity to understand the early shower development, since energetic muons are produced in the very first interactions, thus carrying valuable information about the primary cosmic particles. The use of high-energy physics detectors for cosmic ray physics was pioneered by ALEPH[14], DELPHI [15] and L3 [16] during the Large Electron-Positron (LEP) collider [17] era at CERN.

The muon multiplicity distribution (MMD) was measured at LEP with the ALEPH detector [14]. This study concluded that the bulk of data can be successfully described using standard hadronic production mechanisms, but that the highest multiplicity events containing around 75-150 muons, occur with a frequency which is almost an order of magnitude above the expectation, even when assuming that the primary cosmic rays are purely composed of iron nuclei. A similar study was carried out by DELPHI detector, which also found that Monte Carlo simulations were unable to account for the abundance of high muon multiplicity events [15]. An extension of these earlier studies is now possible at the LHC, where the ALICE capabilities are exploited with this purpose.

I participated in the cosmic-ray data taking of 2012 and 2013 and worked in the analysis of the atmospheric muon events detected in the ALICE experiment in the whole period 2010-2013. My research activities were mainly focused to the study of the measured muon multiplicity distribution and its comparison with Monte Carlo simulations. I have also investigated in details the high muon multiplicity (HMM) events found with data, that is, events with a number of reconstructed muons in the TPC larger than 100 ($N_\mu > 100$).

The description of the shower in the Monte Carlo simulations is based upon two of the latest versions of QGSJET [18, 19], a hadronic interaction model commonly used in EAS simulations.

In the following chapter [2] I summarize the properties of cosmic rays and present the characteristics of the shower development at different stages, as well as a brief description of its measurement methods. Results of cosmic-ray studies performed by previous experiments based upon high-energy physics detectors, are presented in chapter 3. In chapter 4, a general description of the ALICE experiment is presented, specifically of the detector subsystems used to perform cosmic ray physics. Chapter 5 introduces the methods implemented to reconstruct events and the track selection criteria. In addition, the Monte Carlo simulations to reproduce the experimental results required a careful selection of the event generator and models to describe the extensive air showers, as well as the strategy to assure the accuracy and efficiency of the simulations. This is described in chapter 6. In chapter 7, the characteristics of the data sample analysed in this thesis are presented. The analysis of the MMD from data and simulations is discussed, as well as the measurements and interpretation of the frequency of HMM events. The systematic and statistical uncertainties are described during the analysis evolution. The discussion of the final results from the comparison between data and model predictions are discussed in chapter 8, where also the final summary is given.

2 Cosmic rays

2.1 Overview of cosmic rays

Cosmic rays became one of the most fascinating research subjects in modern physics and astronomy since its revolutionary discovery by Victor Franz Hess in 1912. Today, more than one hundred years later the question about the origin of the cosmic radiation still remains unanswered. The main sources of cosmic rays are considered to be the stars, supernova remnants, pulsars, active galactic nuclei, black holes and gamma ray bursts.

Cosmic ray physics has played an important role in the formation of our current understanding of the universe evolution, representing a vast and wide field of research. Hess's discovery contributed to develop the modern physics and astronomy with new fields of research such as particle physics, modern astrophysics and cosmology. The importance of cosmic rays for different branches of sciences started to be better understood in 1932 with the discovery of the positron, and since then many new particles were first reported to occur in cosmic rays. Such is the case of elementary particles like mesons and hyperons, new types of nuclear reactions at high energies, formation of nuclear-meson and electromagnetic cascades in the atmosphere. All of this was discovered during the investigation of cosmic rays, which became a great tool for exploring the fundamental building blocks of matter.

Another important branch of physics that has rapidly evolved together with space exploration, concerns the cosmic-ray energy spectrum, as well as the origin, acceleration and propagation of the cosmic radiation, representing a real challenge for astrophysics, astronomy and cosmology. At present other relevant fields have rapidly evolved, such as high-energy gamma ray and neutrino astronomy. Moreover, geophysical researches of the interior of the Earth are starting under high-energy neutrino astronomy which is likely a spin-off neutrino tomography of the Earth. Finally, of considerable interest are the biological and medical aspects of the cosmic radiation, because of its ioniz-

ing character and the fact of being the unavoidable radiation to which we are exposed.

Since the investigations of air conductivity, started by Coulomb in 1785, physics faced the problem of explaining the leakage of electrical charge from very isolated bodies. At the beginning of 20^{th} century, in connection with the discovery of natural radioactivity, many ingenious experiments were performed in order to solve the puzzle of the nature of such radiation responsible for the electric charge loss observed in isolated electroscopes. The question of whether it was of terrestrial or extraterrestrial origin was crucial. In the spite of the terrestrial origin as the simplest hypothesis considered in that time, Wilson made a suggestion without precedents that such extremely penetrating radiation could have extraterrestrial origin. However this idea was not supported by his experiments. During 2011 the Italian physicist Domenico Pacini demonstrated that a non-negligible part of the mentioned radiations was not coming from the Earth's crust [20]. This was confirmed by measuring the variations of an electroscope's discharge rate as a function of the underwater depth. Paccini's conclusions about the presence of a non terrestrial radiation at sea level were supported by the results from other scientists pointing to the dependence of the radioactivity on the altitude. By following different and complementary methods, these radiations were evidenced by Victor F. Hess during its historical hydrogen-filled balloon flights in 1912 [21]. The expectation was that the flux would decrease with the altitude, precisely the opposite of what Hess found. He determined that up to approximately one Km the ionization was unchanged, however with the increasing altitude up to approximately 5.3 Km the ionization rates escalated several times. Hess drew the conclusion that certain unknown radiation source of ionization of extraterrestrial origin exists, meaning that particles arrived to the Earth from space. This radiation was first named "cosmic rays" by Millikan in 1926 [22]. In absorption measurements of the radiation at different depths and altitudes, Cameron and Millikan concluded that the radiation consisted of high-energy gamma rays. Nevertheless, Bothe and Kolhörster demonstrated that cosmic rays consist mainly of charged particles, by using for the first time a coincidence technique with Geiger Müller counters [23]. The highly penetrating power of cosmic rays was proved by making them traverse a gold absorber placed between two Geiger Müller counters. In 1929 Skobelzyn registered the deviation suffered by cosmic ray in a bubble detector with magnetic field.

He also suggested that these particles were produced in showers [24] while in 1937 Pierre Auger concluded that the extensive particle showers are generated by high-energy primary cosmic-ray particles that interact with air nuclei high in the atmosphere, initiating a cascade of secondary interactions that finally yield a shower of electrons, photons and muons that reach ground level [25]. Later in 1941 was established that cosmic rays are composed mostly by energetic protons constituting $\sim 89\%$, about 10% He nuclei, $\sim 1\%$ heavier nuclei like C, N, O and Fe, while less than 1% energetic electrons and gamma rays [26].

Today, after one hundred years since the discovery of cosmic radiation, its origin remains unknown. Various objects in our Galaxy have been proposed as particle injectors and different acceleration mechanisms are known to have the ability to accelerate or possibly reaccelerate cosmic rays to energies of about 10^{14}-10^{18} eV, although propagation mechanisms are subject of intense debate. Actually, it is a mystery where and how the most energetic particles with more than 10^{18} eV acquire their energies, though various exotic models and processes have been proposed.

2.2 Primary cosmic ray spectrum

The term *cosmic radiation* is referred to the flux of high energy particles, that enter the Earth's atmosphere from the outer space. It includes all stable particles and nuclei with lifetimes of the order of 10^6 years or longer. Technically, "primary" cosmic rays are those particles accelerated at astrophysical sources whereas "secondaries" are those particles produced in interactions of the primaries with interstellar gas. Most of cosmic radiation comes from outside the Solar System, except from particles associated with solar flares. The Solar System is permanently exposed to a flux of these primary particles, with a spectrum extending over many orders of magnitude from about 10^9 eV to at least 10^{20} eV, while the secondaries generated in these first encounters have still enough energy to produce further particles. Cosmic rays are exposed to different magnetic fields in their trajectory from the origin to the Earth, i.e., magnetic field of Earth, Solar System and Galaxy. Consequently the cosmic rays cannot point to the source since they are composed by charged particles being constantly deflected by the magnetic fields.

In the following we call "primary" cosmic rays to all high energy particles

arriving to the Earth atmosphere from the outer space, with either galactic or extragalactic origin. The interaction of primary cosmic rays with the nuclei of the air constituent elements in the upper Earth atmosphere, gives rise to the so-called Extensive Air Showers (EAS) which evolve until ionization processes dominate and the cascade dies out.

2.2.1 Spectrum

The differential cosmic ray spectrum, i.e. the number of primary atomic nuclei arriving at the Earth per unit time, area, solid angle and kinetic energy, follows a relatively smooth power law $dN/dE \propto E^{\gamma}$ over a wide energy range (Fig. 2.1) [27]. At low energies this flux is modulated by the solar cycle through the magnetic field of the Sun[1], which shields the Solar System from charged particles below 10^9 eV. In the range of several GeV ($\sim 10^9$ eV) to about $E_k = 3 \times 10^{15}$ eV, the primary cosmic-ray energy spectrum is well described by a power law with spectral index $\gamma \approx$-2.7. At higher energies the spectrum index changes rapidly to $\gamma \approx$-3.1 creating a 'transition' region at $E = E_k$ called the "knee". The further steepening indicates a second "knee" which is observed at $E_{kk} = 4 \times 10^{17}$ eV. At about $E_a = 3 \times 10^{18}$ eV the spectrum hardens again giving rise to a feature called the "ankle". Beyond the ankle the spectrum is more difficult to quantify.

The mentioned features (knees and ankle) of the primary cosmic ray spectrum are better evidenced when the ordinate is multiplied by some power of the particle energy as shown in figure 2.2. In this figure the total flux is the result of data obtained by several experiments whereas the energy is compared with the equivalent centre-of-mass energy of proton induced collisions at various accelerators. As shown in figure 2.2, the flux at energies below $\sim 10^{14}$ eV was obtained from results of direct measurements like ATIC, PROTON and RUNJOB. Data from direct measurements together with results from the ground array Tibet AS-gamma experiment aimed to measure the EAS, helped to shape the flux at $10^{14} < E < 10^{15}$ eV. The energies around the knee ($E \sim 3 \times 10^{15}$ eV) and beyond, just up to $E \sim 10^{20}$ eV, were covered by several results from EAS measurements compared with hadronic interaction models. This is the case of KASCADE, KASCADE-Grande, Tibet AS-gamma, IceTop, HiRes,

[1] At energies $E < 10^9$ eV the screening effect of the solar wind prevents galactic cosmic rays from penetrating the heliosphere [28], so that the low energy particle flux decreases during periods of high solar activity and reaches its maximum during phases of low solar activity. This phenomenon is known as *solar modulation*.

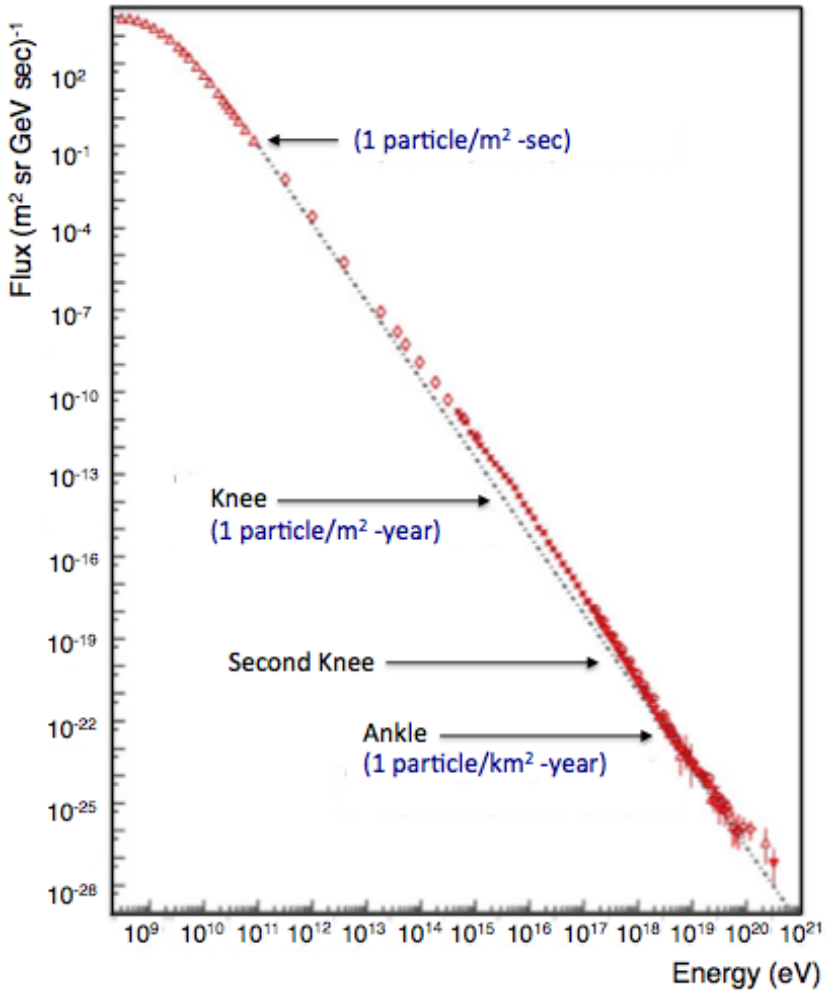

Figure 2.1: Spectra of cosmic rays measured by various experiments above 100 MeV. Direct measurements with detectors in satellites ($E < 10^{15}$ eV) and air shower measurements ($E > 10^{14}$ eV) with large detector arrays. Figure adapted from the plot based on the data compiled by Simon Swordy [27, 29]

the combination HiRes/MIA, Auger and Telescope Array. The last four mentioned experiments reported the results about ultra high energy cosmic rays in the flux spectrum.

The knee ($E \sim 3 \times 10^{15}$ eV) (Fig. 2.2) is an evident feature in the spectrum, however its origin remains controversial [30]. Most models, to explain this energy region, involve a change of chemical composition which implies a change of energy-per-particle. Such a change has been observed by various experiments [31] but systematic uncertainties are too large to discriminate individual descriptions.

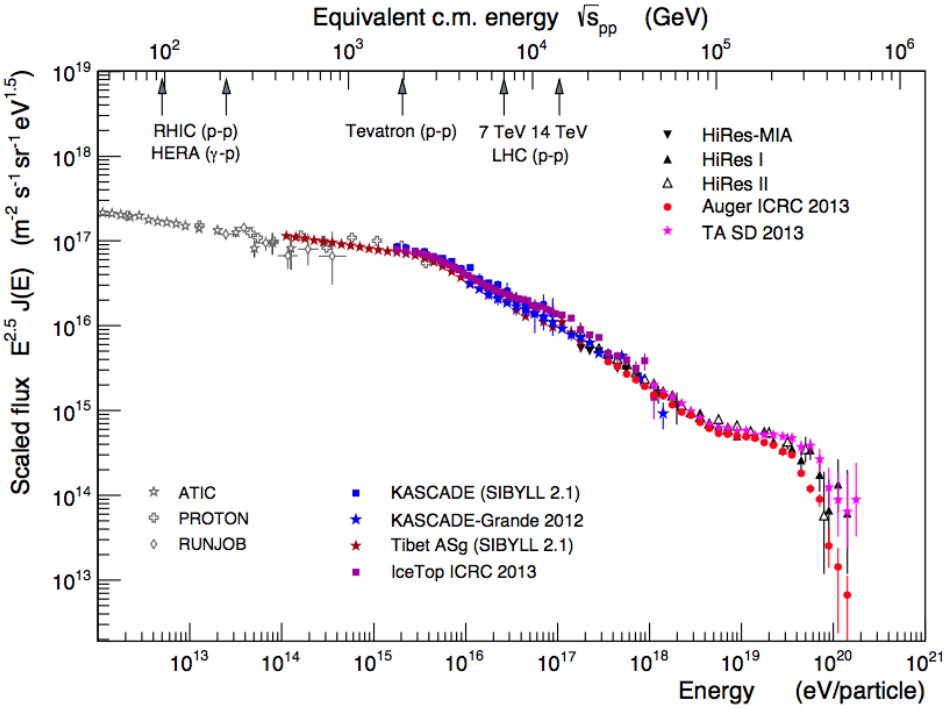

Figure 2.2: All-particle cosmic-ray energy spectrum derived from from direct and indirect (air shower experiments) measurements, as well as results from different hadronic models

2.2.2 Composition

The chemical composition of primary cosmic rays, ranges from protons to actinide elements and is rather close to that of the Solar System. Light elements are the most abundant, leaded by protons which is followed by helium in an order of magnitude less. Among the heavy elements, which have an abundance of 4 orders of magnitude less than light elements, the iron nuclei predominates. The nucleosynthesis is responsible for the galactic abundances of elements from carbon to iron. The relative abundance of a large range of elements is illustrated in figure 2.3. Some pronounced changes in this compositional trend reveal differences between the element abundances in the cosmic rays and the Solar System abundances. For example, the *sub-iron* elements composed by Sc, Ti, V, Cr and Mn (Z = 21 - 25), are more abundant in cosmic rays than in the Solar System. The same happens with lighter elements like Li, Be and B (Z = 3, 4 and 5) which are not abundant end-products of stellar nucleosynthesis. These elements are created by the spallation caused by nuclear interactions of primary cosmic rays with the interstellar matter. The measurement of these nuclei is useful to probe propagation models, since the comparison between their energy spectra and their parent energy spectra provides fundamental in-

formation about the secondary production and propagation of cosmic rays and their dependence from the energy.

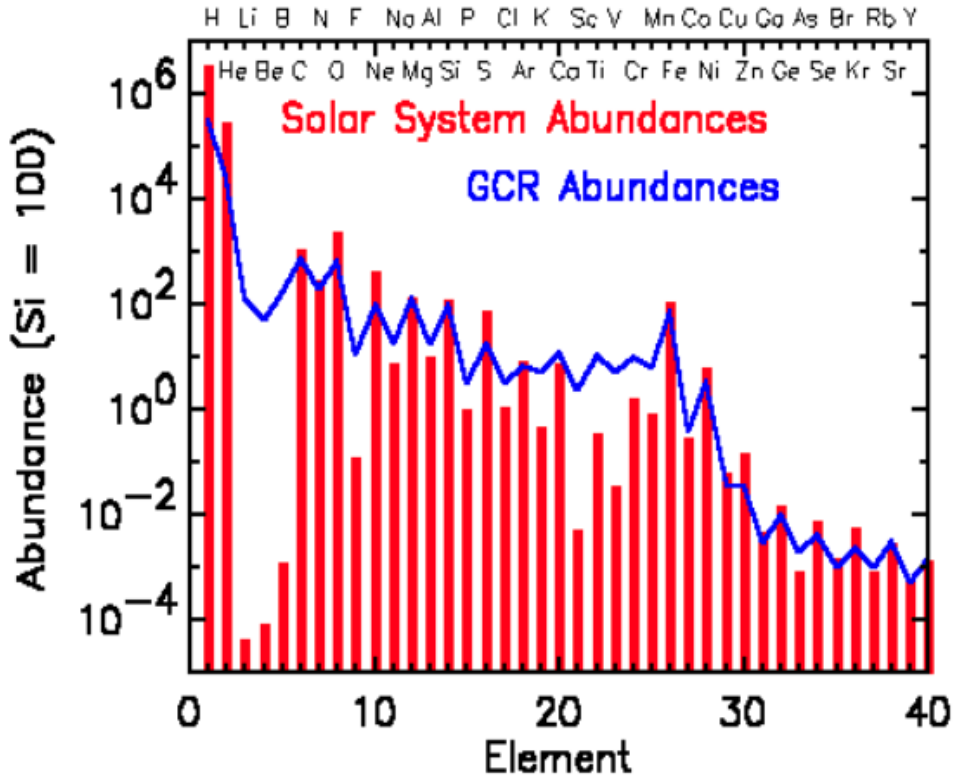

Figure 2.3: Relative abundance distribution of the elements in galactic cosmic rays, compared to the Solar System abundances, normalised to Si = 100. Data taken from [32].

In relation to the flux of cosmic rays arriving at the Earth atmosphere (see the spectrum in figure 2.2), it is known from data of many experiments, that at lower energies mostly protons and light elements dominate the spectrum, while the fraction of heavy elements increases with the increasing energy and thus the average mass of primaries [33]. This trend seems to reverse at ultra-high energies where there are indications, from air shower experiments, that the composition seems to favour lighter nuclei and protons [34, 35].

The primary cosmic ray spectrum for individual group mass compositions is represented in figure 2.4. The kinetic energy ranges from 10^{11} eV to 10^{20} eV [36]. Data of mass group fluxes were collected with direct methods like balloon-borne and satellites up to energies $E \sim 10^{15}$ eV, and from the EAS experiment KASCADE around the knee. The continuous line in figure 2.4 is the fit of all data through a parameterisation described in [36]. Data and fit are compared with the *poly-gonato* model which is described in the next section. The cosmic ray flux at ultra high energy is represented with the fit of the data

measured at the Pierre Auger Observatory at $E > 10^{18}$ eV. These data were fitted and extrapolated downward to 10^{17} eV.

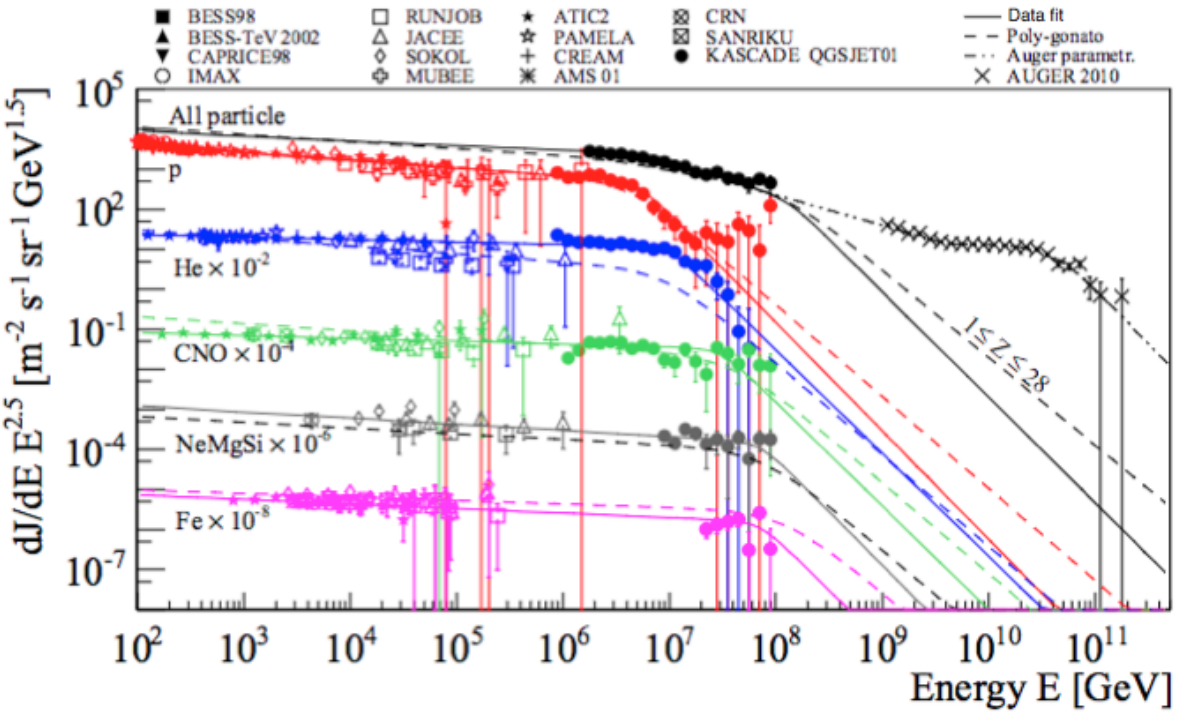

Figure 2.4: Composition of the primary cosmic ray as function of the energy. Data obtained from direct measurements and from shower measurements with KASCADE (legend indicated in the figure) and compared with predictions from *poly-gonato* model (dashed lines) and fit to data (continuous lines). This figure is taken from [36].

All experiments represented in this figure exhibit a similar shape of the spectrum whose continuity was assured with the KASCADE data despite of being measured through the muonic and electromagnetic components of the EAS. The knee of the all-particle spectrum is recognisable at 3×10^{15} eV coinciding with the knee of protons and is extended to around 10^{17} eV for iron, thus showing the knee dependence upon the mass composition. The knee indicates a change of the spectral slope. Protons dominate the composition of primary cosmic rays indicating a ratio of several orders of magnitude of the light composition to the heavier nuclei. There is a transition to a heavier composition at $E \sim 10^{15}$ eV. The increasing contribution of heavy nuclei with increasing energy has been experimentally confirmed by EAS measurements performed by EAS-TOP, EAS-TOP/MACRO, KASCADE, KASCADE-GRANDE, MSU, TUNKA, SPASE/AMANDA, CASAMIA and IceCube experiments, between others [5, 12, 37–46].

2.2.3 Models

The understanding of the origin of the knee in the all-particle spectrum of primary cosmic rays has been a long-standing problem in astrophysics, since it is probably related to the source composition and the mechanisms of acceleration and propagation in the Galaxy (see [47] and references therein).

In the following, there is a general and summarised picture about some theoretical models devoted to explain the knee issue, as well as the phenomenological model called *poly-gonato*.

Theoretical models

Different models offer possible explanations to the change of the slope in the energy spectrum of primary cosmic rays. They interpret the knee in different ways:

- The knee as an indication of a limit where the acceleration mechanisms start to be less efficient.
- The knee as a consequence of the cosmic ray escaping from the galaxy.
- The knee connected with physics processes during the EAS evolution.

The first two items are respectively related to the *acceleration* and *diffusive propagation* of cosmic rays produced in supernova explosions through the Galaxy. Several approaches can be found in the literature, where different *acceleration mechanisms* have been addressed as responsible for the existence of the knee. The common idea is that a substantial amount of the energy released in the supernova explosion is transferred to the ionized particles in form of kinetic energy. According to that, the reachable energy in the acceleration process is proportional to the charge Z of the nuclei, albeit it also depends on the strength of the magnetic field and the characteristic time of acceleration. Some models considering the acceleration of supernova remnants as responsible of the knee, suggest that cosmic rays may reach energies of $Z \times 10^{14}$ eV, which has been also stablished by experimental observations and is consistently described by the theory of diffusive shock acceleration. In other models the injection efficiency is expected to be a function of the mass to charge ratio, such that the heavy elements are accelerated more efficiently and enrich the cosmic rays making the spectrum harder [48].

In alternative approaches, the cause of the knee consists of the outwardly propagating supernova shocks that travel down a steady stellar wind with a Parker spiral structure[2] of the magnetic field. Particles cross the shock wave several times, thus gaining energy proportional to the speed of the wave. The direction of the shock propagation can be assumed parallel to the magnetic field [49], or different angles can be considered [50]. With oblique shocks the individual knees are determined from the dependence of the maximum energy, reached by a given element, on the angle between the shock and the magnetic field. This case was found to accelerate particles more efficiently than parallel shocks, thus increasing the maximum energy attainable by the cosmic rays.

The acceleration in supernova remnants has been also described by models based on observations of different energies and types of supernova explosions. Between them, the model developed by Sveshnikova [51] has the flexibility of considering the most energetic supernova, which results in cosmic rays composed by heavier elements at energies in the range $10^{16} < E < 10^{17}$ eV.

On the other hand, a different explanation of the knee is adopted by models that expect the knee to be a consequence of leakage of cosmic rays from Galaxy [52]. There is a probability of cosmic ray escaping that depends on the magnetic rigidity[3], which in turn depends on the diffusion path lengh. In this case the knee occurs at lower energies for light nuclei compared to heavy ones, which could represent a confinement limit of cosmic rays in the Galactic magnetic field, meaning the transition from confined trajectories to trajectories that escape the Galaxy.

Different interpretations of a kind of "anomalous" diffusive propagation of cosmic ray particles through the Galaxy have been modelled to interpret the knee. Lagutin and collaborators [53] proposed in 2001 a fractal geometry to characterise the interstellar medium and the magnetic field, such that the knee in the primary cosmic ray spectrum is explained by superdifussion propagation. Variants of similar ideas have been implemented in other models to describe the diffusion of cosmic rays in the Galaxy taking into account the regular or irregular magnetic field, a random component, and antisymmetric

[2] Under certain conditions the heliospheric magnetic field can be assumed as twisted into an Archimedean spiral in the solar equatorial plane. This is the so-called Parker spiral structure.

[3] Rigidity: $R = \frac{pc}{Ze}$, where p is the momentum, c is the speed of light and Ze is the charge. The magnetic field causes a deflection of the charge cosmic rays, which is characterized by the gyro-radius with in turn depends on the rigidity as follows: $\rho_{\text{gyro}} = R\frac{sen\theta}{Bc}$ (θ is the angle between the velocity vector of the cosmic ray and the magnetic induction vector).

or Hall diffusion [54–56].

The essential common feature of the processes of particle reaccelerating and diffusion is the magnetic rigidity dependence. From the astrophysical point of view a rigidity dependent cutoff ($E_Z \propto Z$) is most likely the description, but since the origin of the knee is still under discussion other explanations for the change of the spectra slope are possible.

Following a different point of view, there are models that do not "see" the source of the knee in the interstellar medium but in the Earth atmosphere (see third item at the beginning of this section). They suggest that a new type of interaction transfers energy to an unknown or not yet observed component of air showers. The threshold of these new interactions is proposed to be in the knee region. Particles undetected by experimental apparatus, like possible lightest supersymmetric particles and gravitons produced in a sort of "new" EAS interactions, have been suggested by Kazanas [57, 58] as responsible of the steepening at the knee. These approaches have in common that the knee for individual elements scales with their mass number A and not with their nuclear change Z.

Most of the models produce similar all-particle spectra although their basis suggest different theoretical origins of the knee. In general the maximum energy attainable by a nucleus of charge Z differs on the model and types of supernovae considered. The spectra of individual group compositions do not necessarily agree, however most of the models suggest that the knee would result from the convolution of various cutoffs while the spectra composition become heavier, establishing different kind of relationships with particular aspects of acceleration and propagation mechanisms. Maybe the explanation about the cause of the knee in the cosmic ray spectrum comes from the integration of various model basis, e.g. by including injection, acceleration and propagation. The most feasible explanation for the knee seems to be a combination of the maximum energy reached during acceleration and leakage from the Galaxy during propagation, however at present no model can be excluded.

Poly-gonato model

One of the more accepted models, that explains the slope changes in the knee region is the *poly-gonato*[4] phenomenological model [47]. The model assumes

[4] From Greek: "many knees".

power laws and includes solar modulations of nuclei at low energies. The power-law to describe the spectrum is based on the fact that the cosmic rays are most likely to experience diffusive shock acceleration, i.e. first order Fermi mechanism, produced by supernova shock waves propagating in the interstellar medium. Fermi accelerations produce a power-law energy spectrum, which is close to the observed one.

The *poly-gonato* model parametrises the energy spectra of individual elemental compositions based on data from direct measurements where measurements are more precise. It assures a power-law behaviour for the energy spectra of individual nuclei with a cutoff at specific energy E_Z indicating that the knee energy scales with the charge of the individual nuclei. As explained by Hörandel in 2003 [47], the parametrisation of the spectra follows:

$$\frac{d\Phi_Z}{dE_0}(E_0) = \Phi_Z^0 E_0^{\gamma_Z} \left[1 + \left(\frac{E_0}{Z \cdot E_\mathrm{k}} \right)^{\varepsilon_c} \right]^{(\gamma_c - \gamma_Z)/\varepsilon_c}, \tag{2.1}$$

where ϕ_Z^0 and γ_Z are the flux and spectral index respectively, which are obtained from direct measurements. The hypothetical slope beyond the knee is γ_c, whereas ε_c describes the smoothness of the transition from the first to the second power law. The parameters γ_c and ε_c characterise the change of the spectrum above the cutoff energy $E_\mathrm{knee}(Z) = Z \cdot E_\mathrm{k}$, and are assumed to be identical for all the spectra.

A rigidity dependent knee ($\hat{E}_Z = Z \cdot E_\mathrm{k}$) is the parameterization that better describes data, otherwise a mass dependent knee ($\hat{E}_Z = A \cdot E_\mathrm{k}$) or a constant energy ($\hat{E}_Z = E_\mathrm{k}$) can be used.

The parameters γ_c, ε_c and $\hat{E}_Z$ are derived from a fit to the all-particle spectrum as obtained by air shower measurements.

The modelled flux of the all-particle spectrum is then obtained by summing the individual fluxes of the main chemical elements:

$$\frac{d\Phi}{dE_0}(E_0) = \sum_{Z=1}^{92} \frac{d\Phi_Z}{dE_0}(E_0). \tag{2.2}$$

The knee is explained as the successive cutoffs of the individual galactic elements, starting with protons. The second knee seems to indicate the end of the stable elements of the galactic component. This cutoff behaviour of the knee is shown in figure 2.4 where the measured energy spectra from

KASCADE experiment, is compared with the spectra obtained from the *poly-gonato* model [47]. The sum of model fits is consistent with the sum of all measured data. The *poly-gonato* model produce spectra which are more compatible with acceleration in supernova remnants as described in [51], specially when heavy nuclei are considered, and with diffusive propagation as presented in [56]. In addition, with this model the rigidity dependent approach is favoured, assuming that the knee of the cosmic ray spectrum depends on the particle rigidity and consequently the composition becomes heavier above the knee. This rigidity dependence implies that a particle with charge Z, in a Galactic magnetic field may reach a maximum energy $E_{\max}(Z) = Z \cdot E_{\mathrm{k}}$ and above $E_{\max}(Z)$ the particle escapes the Galactic magnetic field. Also various analyses from KASCADE have suggested a rigidity dependent cutoff for individual elements.

2.2.4 Origin

As briefly described in the previous section, most of models point to the idea about a composition and energy spectra of cosmic rays observed at Earth, resulting from the combined effects of acceleration and propagation, starting from sources which are located within the galaxy [31].

The bulk of primary cosmic rays, which are of hadronic nature, is believed to have galactic origin up to energies of about 10^{17} to 10^{18} eV. The sources of the galactic cosmic rays are located in our galaxy, outside the Solar System and different acceleration mechanisms are believed to be the main causes of the acceleration or possibly reaccelerating cosmic rays to energies of about 10^{15} eV to 10^{16} eV, some even to 10^{18} eV. Stellar flakes, stellar coronal mass ejections, supernova explosions and pulsars have been proposed as sources of galactic cosmic rays. However, it is not well known where and how the most energetic particles with energies of 10^{19} eV and beyond acquire their energy [59]. The ultra energetic tail of the spectrum with energies beyond the ankle are probably of extragalactic origin. The rapid fall of the spectrum to energies $E_a > 10^{18}$ eV results in poor statistics, thus preventing us to know more details about the composition of the extragalactic cosmic rays. Furthermore, technical limitations related to the particle identification and energy momentum measurements are present.

The arrival directions of the cosmic rays to the Earth are quite isotropic because their trajectories after have traversed the magnetic fields of our galaxy

are randomly bent. However, at a certain energy threshold of the order of 10^{18} eV the cosmic rays escape the galaxy following trajectories which are almost straight lines. Their sources must be very distant in order to allow for directional randomisation by magnetic fields in space. This reinforces the idea about their extragalactic origin, in whose case it is a puzzle how these particles can reach our part of the universe across large distances without being subject to the Greisen-Zatsepin-Kuzmin (GZK) cutoff, expected to occur around $E = 3 - 5 \times 10^{19}$ eV for protons [60, 61]. This cutoff is due to interactions of the cosmic rays with the cosmic microwave background (CMBR), predicted since 1948 [62] and discovered by Penzias and Wilson in 1965 [63], that degrade the energy of particles via photo-pion production and fragment nuclei until their energies fall below the GZK-limit.

2.3 Interaction of cosmic radiation with the atmosphere

Primary cosmic rays coming from the outer space interact with the nuclei of the atmosphere, usually in the upper part of the atmosphere (top 10%) [64], corresponding to 15-20 Km above the sea level.

The first interaction produces the hadronic component, which consequently interacts again with other air molecules giving rise to a shower of particles called EAS (Fig. 2.5). The EAS consists of three parts:

- *electromagnetic* component composed by photons, electrons and positrons
- *muonic* component composed by muons
- *hadronic* component composed by baryons and mesons

The longitudinal and lateral development of the different components depends on the nature of the primary cosmic ray, its energy and the altitude of the first interactions.

The secondary particles produced in the EAS can be detected by several kind of instruments at different altitudes or by ground/underground level detectors.

Taking into account that around ∼90% of cosmic radiation consists of protons, the most relevant reactions are:

$$\mathrm{p}+\mathrm{p} \longrightarrow \mathrm{p}+\mathrm{n}+\pi^{+}, \qquad \mathrm{p}+\mathrm{p} \longrightarrow \mathrm{p}+\mathrm{p}+\pi^{0}, \tag{2.3}$$

$$\mathrm{p}+\mathrm{n} \longrightarrow \mathrm{p}+\mathrm{p}+\pi^{-}, \qquad \mathrm{p}+\mathrm{n} \longrightarrow \mathrm{p}+\mathrm{n}+\pi^{0}, \qquad \mathrm{p}+\mathrm{n} \longrightarrow \mathrm{n}+\mathrm{n}+\pi^{+} \tag{2.4}$$

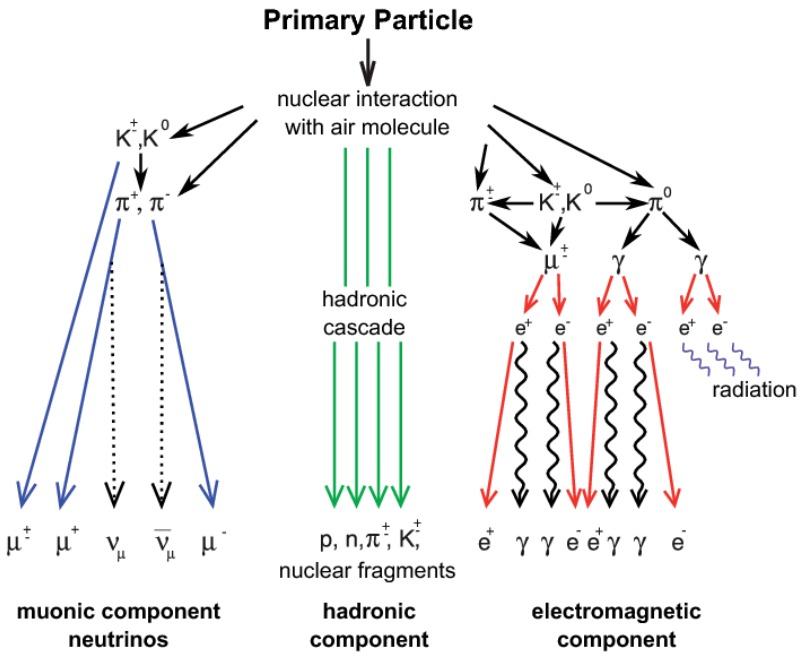

Figure 2.5: Schematic view of a Extensive Air Shower (EAS) generated by a primary cosmic ray in the top atmosphere. This figure is taken from [65].

Other reactions, though less relevant, give rise to particles like kaons, η particles and even resonances.

In the reactions 2.3 and 2.4 all the secondary particles are hadrons, namely protons, neutrons and pions in all their charge states ($\pi^{\pm}$, π^0). The long mean lifetime of charge pions ($\tau_{\pi^{\pm}}$ = 26 ns) guaranties subsequent $\pi^{\pm}$ collisions with air nuclei before decaying. However, in the higher atmosphere where the air density is low, the pion decay dominates over the pion interaction. Almost 100% of charged pions in turn decay to muons (and neutrinos), thus contributing to the *muonic component* of the EAS:

$$\pi^+ \longrightarrow \mu^+ + \nu_\mu, \qquad \pi^- \longrightarrow \mu^- + \overline{\nu}_\mu, \tag{2.5}$$

The *muonic component*, characterised by a very small cross section and a long mean life time ($\tau_{\mu^{\pm}}$ = 2.2 $\times 10^{-6}$ s), loses energy by ionization crossing the atmosphere almost without interaction.

Kaons created by primary cosmic rays, although in less extent and lower mean life time ($\tau_{K^{\pm}} \approx 1.2 \times 10^{-8}$ s), also contribute to the muon multiplicity with leptonic decays (Eq. 2.6), semileptonic decays (Eq. 2.7) and even by decaying in $\pi^{\pm}$, π^0 (hadronic decay mode) (Eq. 2.8) with the consequent muon

production from $\pi^{\pm}$.

$$K^+ \longrightarrow \mu^+ + \nu_\mu, \qquad K^- \longrightarrow \mu^- + \overline{\nu}_\mu, \tag{2.6}$$

$$K^+ \longrightarrow \pi^0 + \mu^+ + \nu_\mu, \quad K^- \longrightarrow \pi^0 + \mu^- + \overline{\nu}_\mu, \tag{2.7}$$

$$K^+ \longrightarrow \pi^+ + \pi^0, \qquad K^- \longrightarrow \pi^- + \pi^0, \tag{2.8}$$

The major contribution to the *electromagnetic* component comes from neutral pions by decaying in two photons in a very short mean life time ($\tau_{\pi^0} = 10^{-16}$ s):

$$\pi^0 \longrightarrow \gamma + \gamma, \tag{2.9}$$

although the following muon decay channels contribute to the positron and electron production as well:

$$\mu^+ \longrightarrow e^+ + \nu_e + \overline{\nu}_\mu \quad \textit{and} \quad \mu^- \longrightarrow e^- + \overline{\nu}_e + \nu_\mu. \tag{2.10}$$

The two photons created from neutral pions (Eq. 2.9), give rise to electron-positron pairs, thus emitting bremsstrahlung photons when the mean electron energies are above a critical energy E_e = 84 MeV. Below E_e, ionization processes dominate over radiative losses.

The vertical fluxes of the major cosmic ray components in the atmosphere are shown in figure 2.6. Except for protons near the top of the atmosphere, all particles are produced in interactions of the primary cosmic rays in the air (Eqs. 2.5–2.9).

The *hadronic* component of the EAS constitutes the core of the cascade. Since high hadron energies assure a longitudinal momentum larger than the transverse momentum, the *hadronic* component stays relatively close to the shower central axis and acts as a collimated source of electromagnetic sub-cascades. The study of the longitudinal and lateral development of EAS is important to determine the number of particles at different observation levels. The longitudinal development represents the number of secondary particles as a function of the atmospheric depth. Observations of the longitudinal development of each shower allow to obtain the energy E_0 of primary cosmic rays by integrating the energy deposition in the atmosphere. The lateral development of EAS gives information concerning to the number of particles as function of the distance from the shower core. The lateral extent of the EAS can be determined in terms of charge particle density as function of the lateral distance (r)

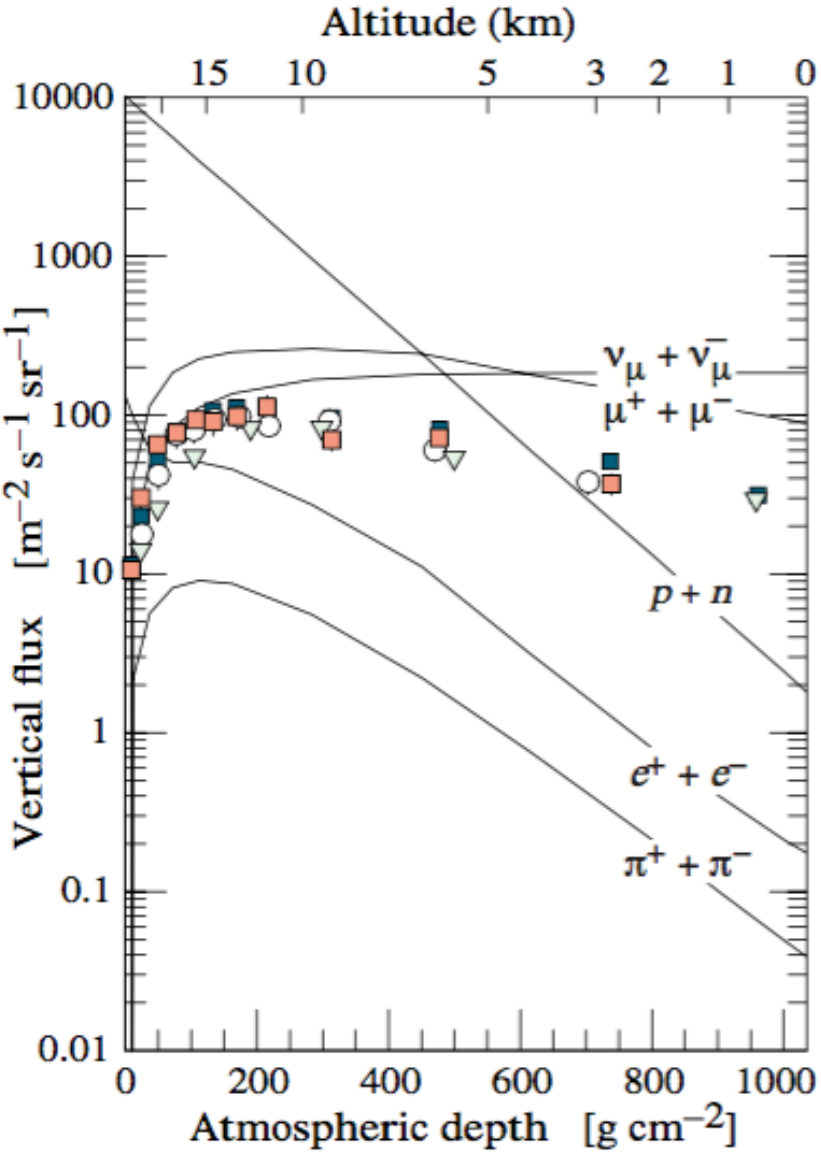

Figure 2.6: Vertical fluxes of cosmic rays in the atmosphere with $E > 1$ GeV [66]. The full and empty points are from measurements of μ^- with $E_\mu > 1$ GeV.

from the cascade centre, according to the Nishimura-Kamata-Greisen (NKG) formula [67]:

$$\rho(r) = C(s)\left(\frac{N_e}{r_M^2}\right)\left(\frac{r}{r_M}\right)^{s-2}\left(\frac{r}{r_M}+1\right)^{s-4.5}, \tag{2.11}$$

where $C(s)$ is a normalisation constant, the parameter s represents the shower age, N_e is the total number of charge particles in the cascade and r_M is *Molière radius* which depends of the atmosphere density and therefore of the altitude where

the cascade is measured:

$$r_{\mathrm{M}} = \frac{E_{\mathrm{s}}}{E_{\mathrm{c}}} X_0 \tag{2.12}$$

Here $E_{\mathrm{s}} = \sqrt{\frac{4\pi}{\alpha}} m_{\mathrm{e}} c^2 = 21.2$ MeV is a constant depending on the particle mass, and X_0 is the atmospheric fraction unit traversed by the particle. At the sea level $r_{\mathrm{M}} \approx 78$ m, and increases with the altitude as the air density decreases. The NKG formula is valid for $0.6 \leq s \leq 1.8$ and $0.01 \leq \frac{r}{r_{\mathrm{M}}} \leq 10$. Finally the lateral extension of the cascade is dominated by the Coulomb scattering of low energy electrons and is also characterised by the *Molière radius*.

It is important to take into account some fluctuations occurring during EAS development, even for particles with the same primary mass and energy. The average relationship between the cascade size N_{e} and its primary energy E_0 depends on the depth in the atmosphere. The equation 2.13 is an estimate of this relationship for primaries with $10^{14} < E < 10^{17}$ eV at 965 m above the sea level (920 g cm^{-2}) [68].

$$E_0 \sim 3.9 \times 10^6 \; GeV \;\; (N_{\mathrm{e}}/10^6)^{0.9} \tag{2.13}$$

The shower maximum (on average) moves down into the atmosphere as E_0 increases. At the maximum shower development there are only 2/3 particles per primary energy unit.

Electrons and positrons are the most abundant particles in the cascade, while the number of muons produced by charged meson decays (Eq. 2.5) is of one order of magnitude less. The lateral development of the EAS gives rise to a large cascade extent at ground level reaching to about several kilometres for the high primary energies.

The number of muons in the EAS, per square meter, as function of the lateral distance from the cascade centre was proposed by Greisen in 1960 [67] (Eq. 2.14):

$$\rho_\mu = C(\frac{1}{r_0})^{1.25} \cdot N_\mu \cdot r^{-0.75} (1 - \frac{1}{r_0})^{-0.25}, \tag{2.14}$$

where r is the lateral distance, r_0 is is the characteristic enlargement distance, N_μ is the total number of muons in the shower and C is a normalisation constant. The dispersion of the *muonic* component is due to both, the transverse momentum of pions and kaons which generate muons and to the Coulomb scattering.

2.4 Cosmic radiation at surface

Muons are the charge particles more abundant at sea level. Most of muons are produced at 15 Km of altitude and they loose about 2 GeV by ionization before reaching the ground. For muon energies lower than 1 GeV the energy spectrum is almost flat, gradually steepening to reflect the primary spectrum in the 10 – 100 GeV range. A further steepening occurs at higher energies, until the critical energies of pions and kaons ($\varepsilon_\pi = 115$ GeV and $\varepsilon_K = 850$ GeV) since almost all mesons decay such that the muon flux has the same power law of parent mesons. At energies above critical values, pions and kaons tend to interact in the atmosphere before they decay. At larger energies ($E_\mu \gg 1$ TeV) the atmospheric muon spectrum can be described by a power law. The integral intensity of vertical muons above 1 GeV/c at sea level is $\approx 70\ m^{-2}s^{-1}sr^{-1}$ [69, 70]. The overall angular distribution of muons at surface level scales with $\cos^2\theta$ ($E_\mu \sim 3$ GeV). At lower energy the angular distribution increasingly steeps, while at higher energy it flattens approaching a $\sec\theta$ distribution for $E_\mu \gg \varepsilon_\pi$ and $\theta < 60^\circ$ [71].

Figure 2.7 shows the muon momentum spectrum at sea level for two θ values, measured by different experiments. At large θ, low energy muons decay before reaching the surface whereas high energy pions decay before they interact, thus the average muon energy increases.

By other hand, the μ^+/μ^- ratio reflects the π^+ excess over π^- as well as the K^+ excess over K^- in the forward fragmentation region of proton initiated interactions. The larger amount of protons over the neutrons in the primary spectrum is also reflected in the μ^+/μ^- ratio.

The *electromagnetic* component of the EAS at ground level consists of electrons, positrons and photons mostly produced in the cascades generated by the decay of charge and neutral mesons. The muon decay is the main source of low energy electrons at sea level. The integral vertical intensity of electrons plus positrons is $\approx$ 30, 6 and 0.2 $\mathrm{m^{-2}s^{-1}sr^{-1}}$ above 10, 100 and 1000 MeV respectively at sea level, but the exact numbers depend sensitively on the altitude, and the angular dependence is complex because of the dependence of the different electron sources with the altitude. The ratio of photons to the sum of electrons and positrons is ≈ 1.3 above 1 GeV and 0.7 below the critical energy ε_0 ($\sim$80 MeV in air) [75].

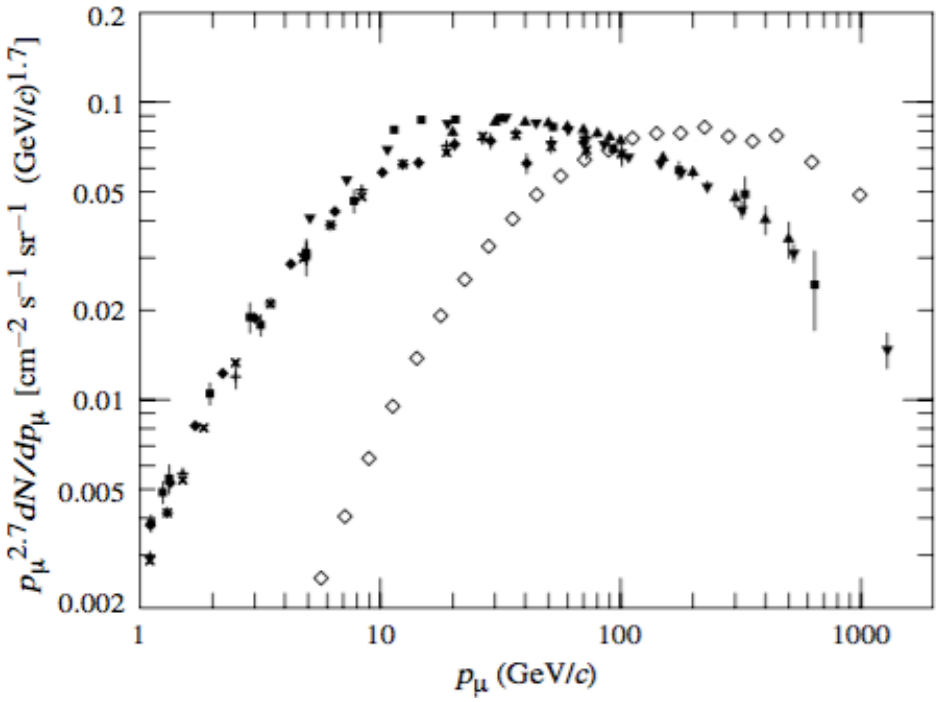

Figure 2.7: Muon momentum spectrum for $\theta = 0°$ (♦ [69], ■ [70], ▼ [72], ▲ [73]) and $\theta = 75°$ ◊ [74].

2.5 Cosmic radiation underground

The terrestrial surface is a high density medium where the *electromagnetic* and *hadronic* components of the EAS are absorbed while only muons and neutrinos penetrate deeply underground. Measurements of muon intensities at different levels under rock allow to establish deep underground flux data. High-energy muon data can be used to investigate the primary spectrum. In particular multi-muon data are useful to explore the primary mass composition. Another objective of muon measurements deep underground has been to establish data for background estimations in heavily shielded underground areas that house neutrino experiments.

Several energy-loss mechanisms characterise the muon propagation through dense matter: ionization and atomic excitation, $e^- e^+$ pair production, bremsstrahlung and photonuclear reactions. The total energy loss of muons can be expressed in terms of the amount of traversed material, as:

$$-\frac{dE_\mu}{dx} = a(E) + b(E)E_\mu, \tag{2.15}$$

where $a(E)$ represents energy loss by ionisation. This term is a slowly varying function of energy and is usually regarded as constant for deep under-

ground applications. The term $b(E)$ is the fraction of energy loss by radiative processes: bremsstrahlung, pair production and photo-nuclear reactions. The quantity $\varepsilon = a/b$ defines a critical value of energy, below which the ionisation loss is more important than the radiative processes. In case of rock $\varepsilon \approx 500$ GeV. Parameters $a(E)$ and $b(E)$ are quite sensitive to the chemical composition of the rock. For this reason it is very important to perform a careful study of the rock for every position of the experimental location.

The detailed knowledge of energy-loss mechanisms is important to compute the *range-energy* relation. The relation between the muon spectrum at surface and the spectra at different underground depths can be determined with the consequent *depth-intensity* definition. The latter is a method to explore the highest energies of the muon spectrum at ground level and to link it with the primary spectrum and composition of cosmic rays.

If we integrate the equation 2.15 by assuming $a(E)$ as a constant, the average range can be obtained,

$$R_\mu(E) = \frac{1}{b} ln \frac{a + bE}{a} \tag{2.16}$$

The average range of muons as a function of energy in standard rock[5] is shown in Table 2.1 together with the energy loss parameters.

E_μ GeV	R ($\times 10^5$ g cm^{-2})	a (MeV g^{-1} cm^2)	Σb_i ($\times 10^{-6}$ g^{-1} cm^2)
10	0.05	2.17	1.90
100	0.41	2.44	3.04
1000	2.45	2.68	3.92
10000	6.09	2.93	4.35

Table 2.1: Average muon range R and energy loss parameters calculated for standard rock [76]. Here $\Sigma b_i = b_{brems} + b_{pair} + b_{nucl}$.

Solving the equation 2.16 for E we get the *range-energy* relation,

$$E = \frac{a}{b}\left(e^{bR_\mu} - 1\right) \tag{2.17}$$

Considering the weakly energy dependence of the term a in the equation 2.17, we obtain the relation between the muon energy at production in

[5] $A = 22$, $Z = 11$, $\rho = 2.65$ g cm^{-3}

the atmosphere ($E_{\mu,0}$) and its mean energy (E_μ) after have traversed a thickness X of the rock (water or ice) as follows,

$$E_\mu = (E_{\mu,0} + \frac{a}{b})e^{-bX} - \frac{a}{b} \tag{2.18}$$

Monte Carlo simulations of the underground muon propagation should account for the stochastic energy-loss processes, which play an important role when the muon range starts to be comparable to the radiation length in the medium. Large fluctuations are produced at large depths (high energies) where the electromagnetic processes (accounted by the term b) are more important than the energy loss by ionization.

There are two depth regimes for equation 2.18. For $bX \ll 1$, $E_{\mu,0} \approx E_\mu(X) + aX$, while for $bX \gg 1$, $E_{\mu,0} \approx (\varepsilon + E_\mu(X))\exp(bX)$. Thus, at shallow depths the differential muon energy spectrum is approximately constant for $E_\mu < aX$ and steepens to reflect the surface muon spectrum for $E_\mu > aX$, whereas for $bX > 1$ the differential spectrum underground is again constant for low muon energies but steepens to reflect the surface spectrum for $E_\mu > \varepsilon \approx 0.5$ TeV. In the deep regime the shape is independent of depth, although the intensity decreases exponentially with depth. In general the muon spectrum at slant depth X is

$$\frac{dN_\mu(X)}{dE_\mu} = \frac{dN_\mu}{dE_{\mu,0}}\frac{dE_{\mu,0}}{dE_\mu} = \frac{dN_\mu}{dE_{\mu,0}}e^{-bX}, \tag{2.19}$$

where $E_{\mu,0}$ is the solution of the equation 2.18 in the approximation of neglecting fluctuations.

2.6 Cosmic radiation measurements

The flux of primary cosmic rays is attenuated with increasing atmospheric depth. Light primary nuclei reach larger atmospheric depths, while heavy primary nuclei are rapidly attenuated because of fragmentation. The interaction mean free path of nuclei in air decreases from 75 g/cm^2 for protons to 14 g/cm^2 for iron nuclei. Thus, the flux of primary nuclei that survive on their way through the atmosphere down to the sea level is vanishing small.

Direct measurements

The high altitude data detected with direct measurements, are the backbone for the determination of primary cosmic ray spectrum and mass composition

over a wide range of energies. Direct measurements may access cosmic ray energies in different intervals up to $\sim 10^{15}$ eV, and are complemented with EAS data at high and ultra-high energies. Detailed simulations and cross-calibrations between different types of detectors are necessary to establish the primary energy spectrum from air shower experiments.

The low energy component of cosmic rays hitting the atmosphere, has been explored in the top atmosphere with instruments on board of satellites, space stations, aircrafts and balloons using a wide variety of techniques and instruments. Excellent data between the geomagnetic cutoff and 10^{15} eV, have been produced by experiments in the upper atmosphere using electronic detectors such as spectrometers, Cherenkov counters, calorimeters, transition detectors, combinations of the more advanced systems, or nuclear emulsions, thus recording and identifying individual primary cosmic rays. One of the advantages of direct measurements is the possibility of identifying the original particle that would generate the EAS detected by ground-based detector. However, to increase the maximum detectable energy it is needed to have detectors big enough, and to perform long measurements, which becomes an important difficulty that this type of experiments have to overcome. The use of nuclear emulsion chambers has been pioneered by experiments like JACEE[6][77] and RUNJOB[7] [78], which have studied the energy spectra of cosmic rays from proton to iron at energies extending to 10^{15} eV. The nuclear emulsion is a passive technique with limited exposure times because of the integrating effects of the background. Several new complex balloon-borne instruments employing superconducting magnets were built like BESS[8], CAPRICE[9], and HEAT[10] [79–81], whereas data from cosmic rays with a large charge range and higher energies have been covered by balloon-borne instruments which have been equipped with efficient spectrometers like ATIC[11] [82] and CREAM [12] [83]. These instruments are characterized by a high energy resolution, especially CREAM with the larger number of pixels in smaller area allowing a very efficient geometry. It reached a record of exposure of 162 days, being 40 days in only one flight. As part of the direct measurements of primary cosmic

[6] **J**apanesse-**A**merican **C**ooperative **E**mulsion **E**xperiment
[7] **RU**ssia-**N**ippon **JO**int **B**alloon collaboration
[8] **B**alloon-**E**experiment with a **S**upercondinting **S**olenoid
[9] **C**osmic **A**nti**P**article **R**ing-**I**maging **C**herenkov **E**xperiment
[10] **H**igh-**E**nergy **A**ntimatter **T**elescope
[11] **A**dvanced **T**hink **I**onization **C**alorimeter
[12] **C**osmic **R**ay **E**nergetic and **M**ass **B**alloon **E**xperiment

rays, in 2006 was launched the satellite based experiment PAMELA[13] [84], which is a permanent magnet spectrometer with a variety of specialised detectors, dedicated to perform precision measurements of cosmic rays, mainly focussed on particle identification and to study the antimatter component of cosmic radiation.

Air shower measurements

With the increasing energy, at values larger than 10^{14} eV, the differential flux of primary cosmic rays rapidly falls to one particle per square meter-steradian per year (see figure 2.1). This leads to use larger collection areas with detectors operating for long periods in order to reach reasonable statistics. Hence the understanding of the primary flux at energies around the knee depends on ground-based air shower observations, and require the detection of different components of the EAS, i.e. hadrons, electromagnetic radiation, Cherenkov light and muon content. At this point, only secondary products from air showers can be measured. These particle showers are spread over large areas deep in the atmosphere, at ground level and even underground.

Air shower experiments that use the atmosphere as a calorimeter generally measure a quantity that is related to total energy per particle. As explained in sections 2.2 and 2.4 electrons and positrons are the most abundant particles in the cascade, while muons are the charge particles more abundant at see level. Many experiments have been dedicated to detect the air shower components in order to investigate the spectrum and composition of primary cosmic rays facing the problem of the low event rate at high energies with large installations. They consist of large detector arrays at ground level with different altitudes with respect to the sea level. Relevant data of the cosmic ray spectrum at energies around the knee have been reported by shower experiments like EAS-TOP, EAS-TOP/MACRO, KASCADE, KASCADE-GRANDE, MSU, TUNKA, SPASE/AMANDA, CASAMIA, TIBET and IceCube experiments, between others [5, 12, 37–46, 85, 86]. Some of the most relevant results about the chemical composition in the energy range around the knee of the primary cosmic ray spectrum have been obtained by the KASCADE experiment in Karlsruhe, which is optimised to measure EAS in the energy range of 10^{14} eV to 10^{17} eV. It consists of a big scintillator array with muon tracking detectors, which was projected to distinguish between muons and electrons, and a huge

[13] **P**ayload for **A**ntimatter **M**atter **E**xploration and **L**ight-nuclei **A**stophysics

iron sampling calorimeter installed at centre of KASCADE detector aimed to measure energy and number of hadrons. Different components of the EAS can be measured by using this multi-detector concept. This complex experimental arrange is spread over an area of 200×200 m^2 located at 110 meters above the sea level. KASCADE-GRANDE is an extension of KASCADE, and consists of a multi-component air shower experiment aimed to measure the all-particle energy spectrum by extending the energy region to 10^{18} eV and with a larger collection area of 700×700 m^2.

Other shower experiments have also explored different kinematic regions of the cosmic ray spectrum and have made useful contributions in researches about the elemental composition. The EAS-TOP experiment, located at 2005 m above the sea level operated in the ninetieth at the Gran Sasso Laboratories producing important results about the flux of various primary cosmic ray elements and the all-particle energy spectrum in the range of 10^{15} eV to 10^{16} eV. Some results come from measurements in coincidence between the surface apparatus EAS-TOP with the underground detector MACRO, which is located under the mountainous overburden of the Gran Sasso in Italy. In the same decade, in Chicago and Michigan began operating the experiment CASA-MIA whose objective was studying gamma rays and cosmic ray interactions above 10^{14} eV. CASA-MIA was based on an array of surface particle detectors (CASA) and another array of underground muon detectors (MIA). Data from CASA-MIA allowed to estimate a position and shape of the knee from the electron and muon size of individual showers, slightly above 10^{15} eV and suggested that the knee is dominated by heavy elements. Similar results were obtained by the shower array TIBET experiment in China.

Experiments which study cosmic rays at higher energies ($E > 10^{16}$ eV) complement the shower arrays that work around the knee energy. Such is the case of KASCADE-GRANDE, HiRes[14], AGASA[15] and the AUGER experiments. HiRes was mainly based on the fluorescence technique with optical telescopes [87], AGASA is a ground-level array of muon detectors covering 100 Km^2, while Auger employs ground array and fluorescence detection methods. Cosmic rays of high and ultra-high energies (up to 10^{18} eV and beyond) have been measured by these experiments, through the measurement of its shower components. They have also confirmed the knee and observed

[14] **H**igh **Res**olution Fly's Eye

[15] **A**keno **G**iant **A**ir **S**hower **A**rray

the GZK cutoff (briefly introduced in section 2.2.4) at the second knee of the spectrum as an indication of the highest energy cosmic rays interacting with the cosmic microwave background [35, 88–91].

Underground measurements

The secondary particles generated during the EAS evolution down to the ground level are absorbed in interactions with the rock, while only muons penetrates deeply underground. Muon intensities have been measured at different underground levels with a varying amount of overburden rock, down to depths of about 10^6 g cm^{-2}, as well as in ice to shallower depths. At underground level the advantage is the possibility of measuring only the muonic component of the EAS. Underground measurements of muons have been carried out under a variety of different conditions, using different detector types, geometries, and different rock compositions. Underwater measurements have the advantage that the overburden is exactly known leaving no ambiguities about density and composition variations along a particle trajectory.

Among the most relevant underground measurements, that have measured muon multiplicity distribution to explore the energy spectrum and composition of cosmic rays, we should mention the MACRO [16] experiment at Laboratory Nazionali del Gran Sasso (LNGS) which is took data from 1989 until 2001 and consisted of large liquid scintillator counters, streamer tubes and plastic track-etch detectors. This is one of the deeper detectors (3.2×10^5 g cm^{-2}), collecting muons with a threshold energy of $\sim$1.4 TeV. In the same institute (LNGS) another underground experiment, the LVD [17], was installed, consisting of 38 modules each containing eight liquid scintillator counters. Both, LVD and MACRO, registered events in coincidence with the surface experiment EAS-TOP which covers an area approximately 10^5 m^2 [92, 93]. EAS-TOP was used to measure the electromagnetic size of the shower N_e, whereas the muon multiplicity was measured with its underground facility. In addition, detector SOUDAN II [94] from Minnesota obtained a muon multiplicity distribution, corresponding to a muon threshold E_{th} = 700 GeV. This is a calorimeter consisting of iron/drift tubes located at a depth of 2.1×10^5 g cm^{-2}. At a shallower depth (8.5×10^4 g cm^{-2}) was installed the BUST[18]

[16] **M**onopole with **A**strophysics and **C**osmic **R**ay **O**bservatory
[17] **L**arge **V**olume **D**etector
[18] **B**aksan **U**nderground **S**cintillation **T**elescope

detector [95], an underground scintillator telescope consisting of an array of four horizontal and for vertical scintillator layers, to detect muons over 220 GeV which has reconstructed the energy spectrum of cosmic rays at about 10^{12} eV [96]. More recently started the experiment EMMA[19], which is 85 m underground and differs from other underground experiments in its ability to measure lateral distribution of muons [97]. Many of these experiments used different Monte Carlo hadronic-interaction models to simulate the shower, and GEANT to propagate muons through the rock. Their results suggested the existence of the knee and were consistent with an mixed chemical composition having an increasing mass trend at energies around the knee. The inaccuracies of the hadronic interaction models and accumulated systematic uncertainties were the main limits.

[19] **E**xperiment with **M**ulti **M**uon **A**ray

3 Cosmic ray physics with accelerator detectors

During the era of LEP [17], the particle accelerator built at CERN in Geneva and used from 1989 until 2000, some experiments started to develop a common cosmic-ray research project called Cosmo-LEP [98], taking advantage of the relative shallow depth location and making use of the performance and good tracking capabilities of these underground detectors. The participating detectors were ALEPH[1], DELPHI[2] and L3 + C. Another accelerator based detector that have performed studies of atmospheric muons is CMS[3] [99], one of the four large experiments at CERN LHC at present.

In the following, the most relevant results related to atmospheric muon measurements in accelerator-based detectors at CERN are presented.

3.1 Cosmo-ALEPH experiment

Cosmo-ALEPH [100] was the first experiment to operate in Cosmo-LEP project. The ALEPH apparatus, located 140 m underground, was capable to detect muons with threshold energy E_{th}= 70 GeV and record multi-muon events with multiplicities up to 150 muons in an area of $\sim$8 m^2. The ALEPH location was the deepest LEP point. It collected 580 000 cosmic ray events during LEP data taking periods during 1997 - 1999, corresponding to 19.6 days effective time [101]. The TPC of ALEPH with 1.8 m outer radius, surrounded by the electromagnetic (ECAL) and hadronic (HCAL) calorimeters (Fig. 3.1) inside a magnet field of 1.5 T, provided good tracking capabilities. Cosmic trigger was given by the the coincidence of energy deposition of muons in opposite HCAL supermodules.

A Monte Carlo strategy using CORSIKA with QGSJET 01 model [102]

[1] **A**pparatus for **LEP** **PH**ysics
[2] **DE**tector with **L**epton **P**hoton and **H**adron **I**dentification
[3] **C**ompact **M**uon **S**olenoid

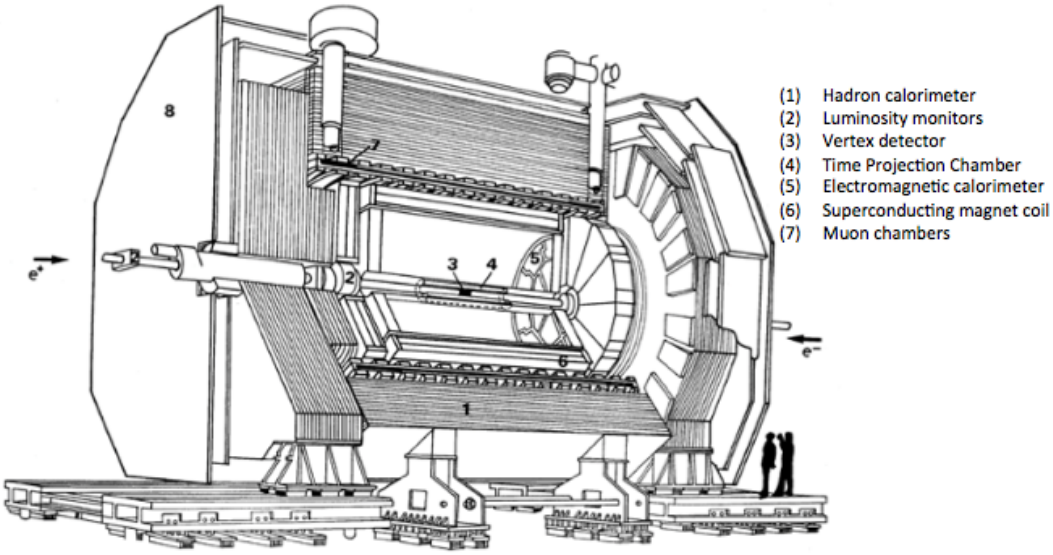

Figure 3.1: Layout of ALEPH detector.

to simulate extensive air showers, and GEANT3 to describe the overburden rock, was adopted to calculate the expected muon multiplicity distribution and to compare it with the measured one (Fig. 3.2).

The data (see Fig. 3.2) are well described from the simulations up to multiplicities around $N_\mu = 40$. In particular multiplicities in the range $5 < N_\mu < 20$, sensitive to the energy spectrum around $10^{15} < \mathrm{E} < 10^{16}$ eV, are due to light elements (proton curve), while the range $20 < N_\mu < 40$, covering an energy region above 10^{16} eV, is dominated by heavier elements (iron curve).

However in the data there are five events with more than 70 muons not expected in simulations. While simulations describe the data over a wide range of multiplicity, they fail to reproduce the highest multiplicities, even under extreme assumptions of a pure iron composition.

The five high muon multiplicity events occur with a frequency which is an order of magnitude above the simulations.

3.2 DELPHI experiment

The DELPHI detector, installed in the CERN LEP tunnel, collected 18.5 days live time of cosmic ray data during 1999 – 2000 [103]. It was located 100 m underground with 84 m of overburden rock, imposing a muon momentum cutoff of 52 GeV/c. A hadron calorimeter was responsible for sampling the

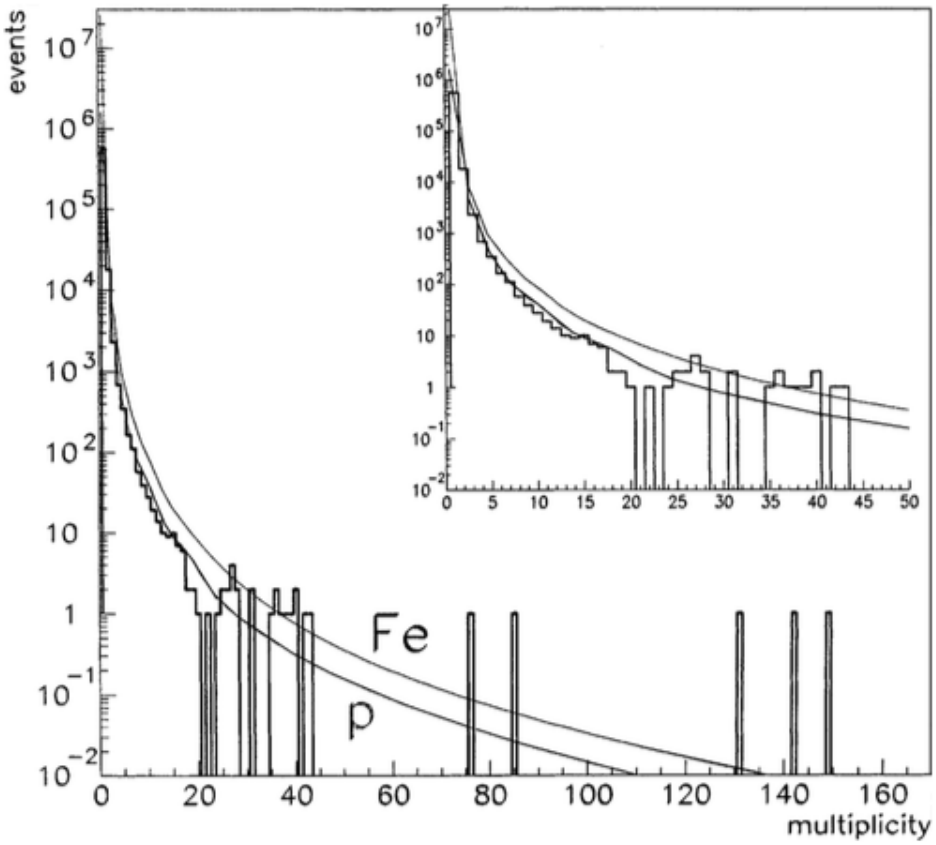

Figure 3.2: Muon multiplicity distribution measured in the ALEPH TPC, compared with the expected multiplicity calculated with CORSIKA [101].

muon energy depositions taking advantage of its fine granularity, although full spatial information on traversing muons was only obtained from the TPC, which had an active area 10 times smaller than the calorimeter. The trigger of cosmic events was entirely given by TOF based on plastic scintillator counters. The layout of DELPHI is shown in figure 3.3, where subdetector systems used for cosmic ray studies are indicated.

The reconstructed muon multiplicity distribution was obtained up to $N_\mu \approx 120$, because events with higher multiplicities produced hits in more that 50% of the tubes of the hadron calorimeter, consequently individual muons could not be counted anymore, and the event is tagged as "saturated". This is shown in the left panel of figure 3.4. To try to reproduce the measured multiplicity distribution, CORSIKA software package with the QGSJET 01 model [102] was used to simulate high energy interactions. The geometric environment including the rock, experimental cavern and access shafts were simulated by GEANT3. Two extreme chemical compositions of primary cosmic rays were

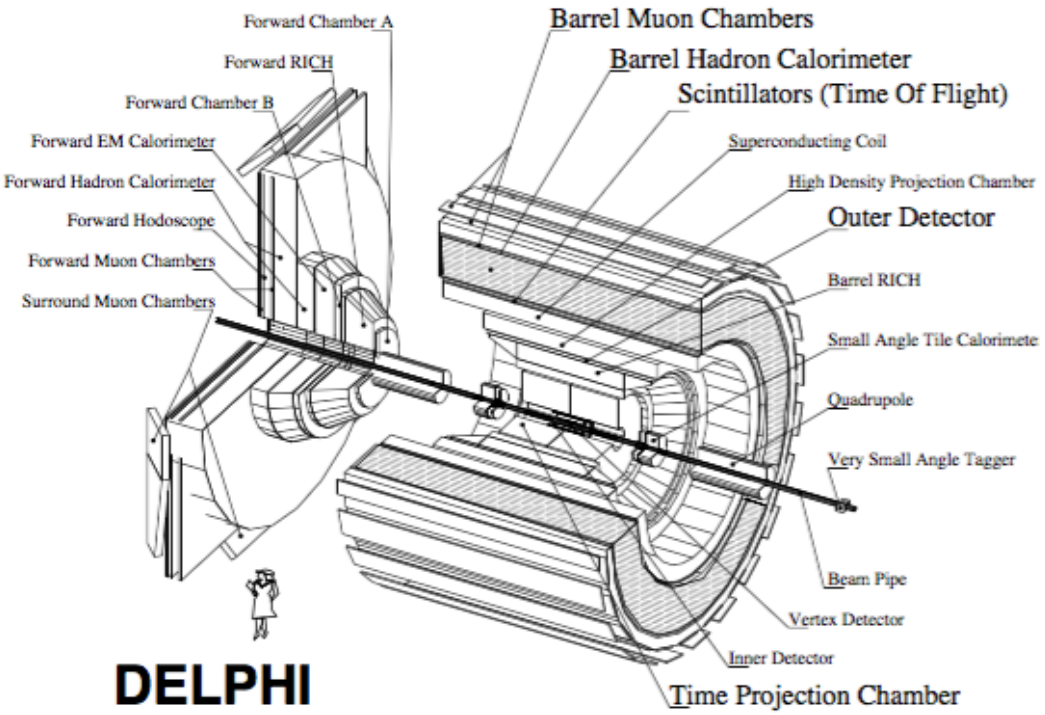

Figure 3.3: Layout of DELPHI detector [103].

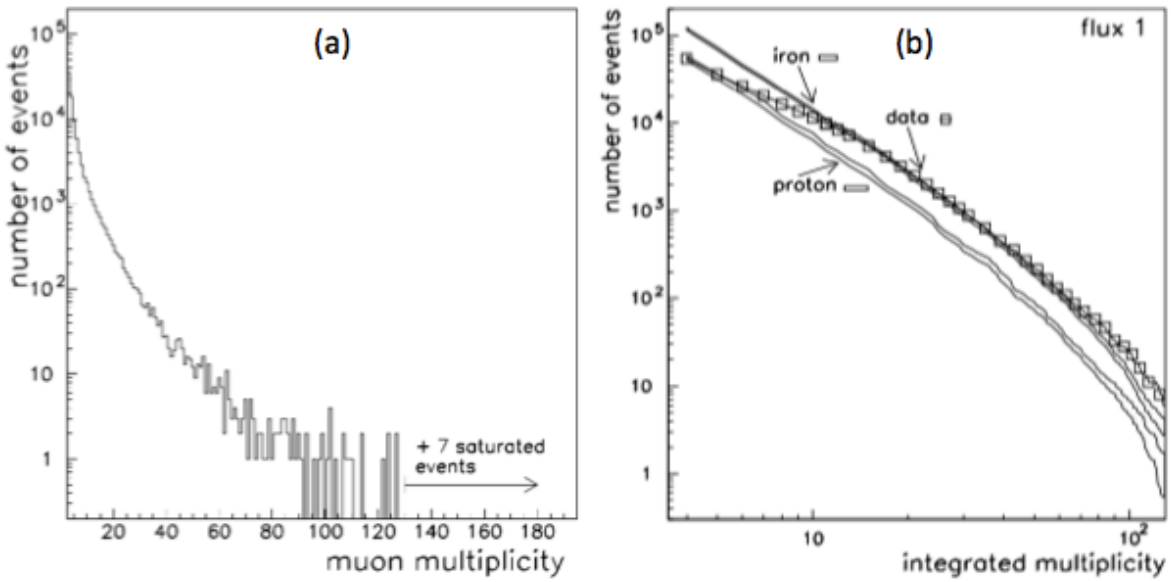

Figure 3.4: (a) Differential muon multiplicity distribution. (b) Comparison of the integrated multiplicity with the Monte Carlo simulations where highest flux and extreme chemical composition of primaries were assumed [103].

assumed: proton and iron. Three variants of energy spectrum were considered by varying the spectral index in such a way that the flux changed while

the shape was kept. The measured integrated[4] multiplicity distribution was compared with Monte Carlo simulations (right panel of figure 3.4).

The high muon multiplicity events, in DELPHI, were defined as those with more than 45 muons. They concluded that the Monte Carlo simulation based on the hadronic interaction model QGSJET failed to describe the abundance of high multiplicity events, despite of using the combination of extreme assumptions of highest measured flux values and pure iron spectrum [103].

3.3 L3 + C experiment

The L3 + Cosmic experiment, so called "L3 + C" was carried out in the predecessor of the LHC, the LEP, exactly in the same location were ALICE is presently installed. Located 52 m underground with 28 m of overburden rock, had an array of about 200 m^2 scintillators on the top of the magnet to provide the cosmic trigger and a reference time signal for cosmic muons. Inside the solenoid magnet, muon spectrometer drift chambers were installed for readout.

A schematic view of the L3 detector is shown at figure 3.5.

In this experiment around 1.2×10^{10} atmospheric muons were collected during 1999 and 2000, allowing to perform muon flux and charge ratio studies. Precise momentum measurement was possible over the large barrel muon spectrometer operating under a magnetic field of 0.5 Tesla, up to a maximum momentum of 1.8 TeV/c.

The measured flux of vertical muons was compared to the flux obtained from direct experiments, even when most of previous experiments measured atmospheric muons with momenta lower than $\sim$ 100 GeV (Fig. 3.6). Systematic uncertainties arised from the rock contribution as reported in [16]. It can be noted that at lower energies there is a slope difference between L3 + C and the rest of the experiments. At energies above 10^2 GeV, it is difficult to compare the results because of the lack of data from the direct measurements. Only data from Kiel [104] cover energies up to 1000 GeV and seem to be consistent with the L3 + C results.

[4] All events with a given (or higher) multiplicity contribute to the corresponding bin.

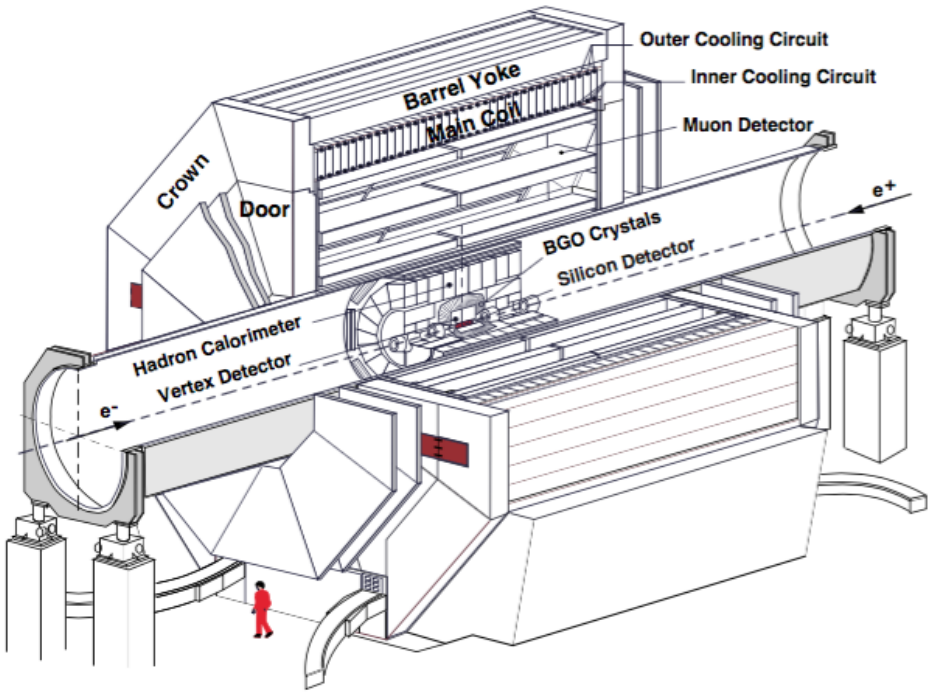

Figure 3.5: Layout of L3 detector.

3.4 CMS experiment

The CMS detector is a large superconducting solenoid, installed in a cavern 89 m underground at 420 m above the sea level with 70 m of overburden rock. It provides a magnetic field of 3.8 – 4 Tesla. A high precision tracking system is guaranteed by the electromagnetic and hadron calorimeters inside the solenoid magnet. The experimental description of CMS can be found in [105] and the detector layout is shown in figure 3.7.

During detector commissioning periods, until 2009, CMS registered atmospheric muons with large statistics to align the tracker and muon systems and to test the whole detector system. Although the CMS was designed to search for signals of new physics in proton–proton and heavy ion collisions, their high quality data from cosmic runs were used to perform studies of physical quantities related to atmospheric muons.

CMS measured the cosmic muon charge ratio, as function of the muon momentum. In figure 3.8 it is shown the charge muon ratio measured by CMS, compared with other measurements done by underground experiments. The fits correspond to the CMS data only, together with the χ-squared fit performed by Schreiner along with MINOS and L3 + C data [106]. The CMS result is

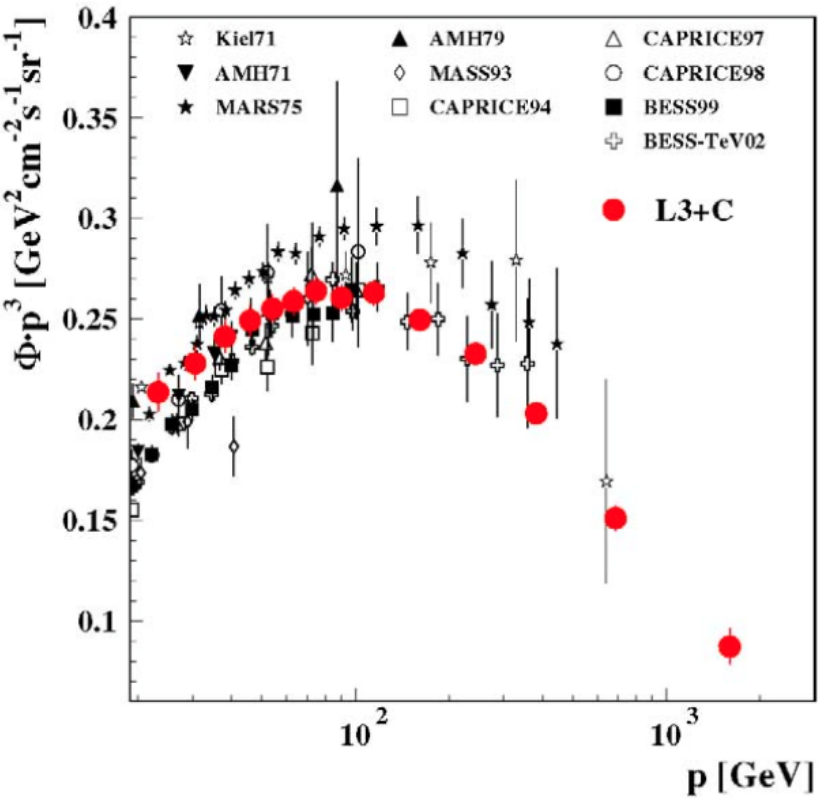

Figure 3.6: Comparison of vertical muon spectrum flux measured by L3 + C to the flux measured with direct measurements. Results are presented with absolute normalisation [16].

in agreements with the previous experimental results, specifically with L3 + C below 400 GeV/c and with UTAH, MINOS and OPERA above 400 GeV/c. This is was the most precise measurement of the charge ratio for momenta lower than 0.5 TeV/c [99].

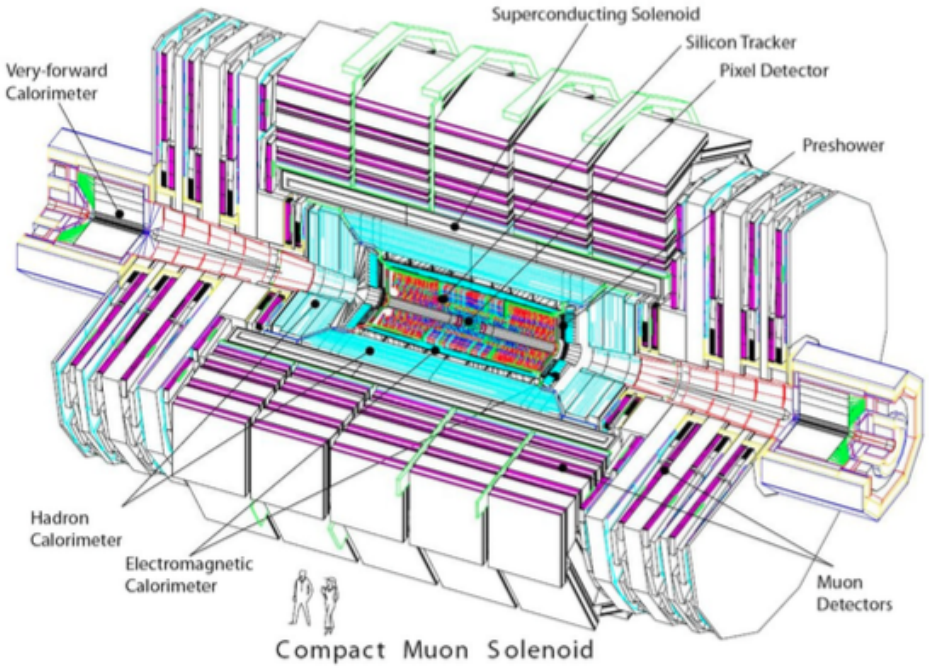

Figure 3.7: Layout of CMS detector.

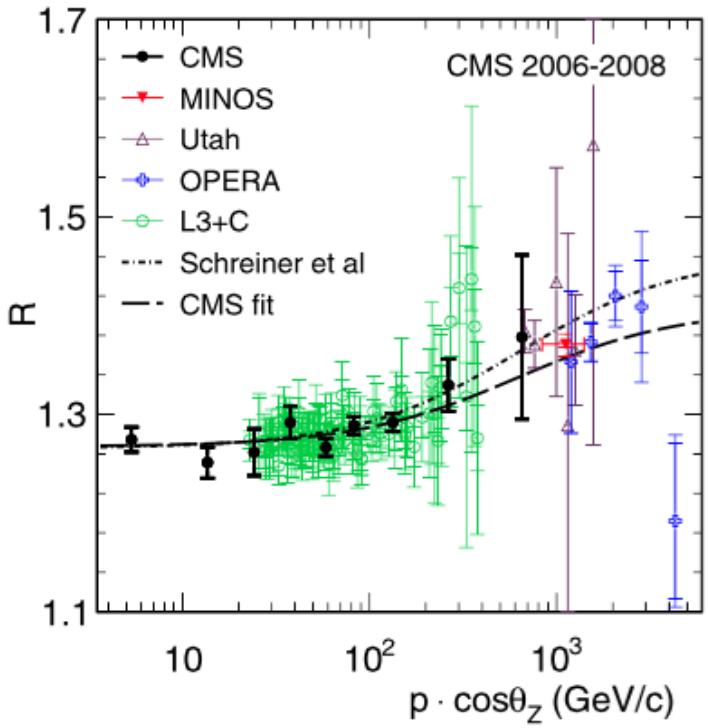

Figure 3.8: Muon charge ratio obtain by CMS as function of the vertical momentum component, compared with measurements from other experiments. [99].

4 The ALICE experiment at CERN

ALICE (A Large Ion Collider Experiment) [1] is one of the four large experiments at the CERN Large Hadron Collider. It was designed to study Quark-Gluon Plasma (QGP) formation in ultra-relativistic heavy-ion collisions at the CERN Large Hadron Collider (LHC). It is focused on the strongly interacting matter at extreme energy densities, predicted by quantum chromodynamics and whose existence is now firmly established experimentally [2]. The physics program is based on the A–A (Pb–Pb) collisions. It also includes proton–proton (pp) and proton–nucleus (p–Pb) collisions in order to vary the energy density and interaction volume to provide the reference data for the heavy-ion programme. ALICE has been optimised to reach high-momentum resolution as well as excellent particle identification over a broad range of momentum from tens of MeV/c to around 100 GeV/c, up to the highest multiplicities predicted by the LHC. ALICE employs essentially all known particle identification techniques: specific ionization energy loss dE/dx, time–of–flight, transition and Čerenkov radiation, electromagnetic calorimetry, muon filters and topological decay reconstruction.

The large size and excellent tracking capability of the ALICE Time Projection Chamber allowed to perform atmospheric muon analysis in order to contribute to cosmic ray physics. With this aim a programme of cosmic ray data taking was carried out, during pauses in collider operations where no beam was circulating. This is intended to be an extension of earlier cosmic-ray studies with high-energy physics detectors, pioneered by ALEPH, DELPHI and L3 (see Chapter 3). Now, in the LHC, experiments can operate under stable conditions for many years.

In this Chapter, a brief overview of the ALICE detector is described, with emphasis in detector subsystems directly involved in the cosmic-ray studies performed in this thesis.

4.1 Brief picture of the ALICE detector system

ALICE is located at Point 2 of the LHC accelerator complex, approximately 450 m above sea level in a cavern 52 m underground with 28 m of overburden rock. The geometry of ALICE is typical of any collider experiment. A complete description of the apparatus is given in [1]. Figure 4.1 shows a schematic view of the ALICE detector. A large solenoidal magnet forms a central barrel that houses several detectors. The magnet is a room-temperature solenoid originally built for the L3 experiment [107] at LEP. The L3 magnet is an octagonal steel yoke which operates with current 30 kA and nominal field strength ≤ 0.5 T. The field homogeneity of the ALICE magnet was improved compared to the original L3 solenoid.

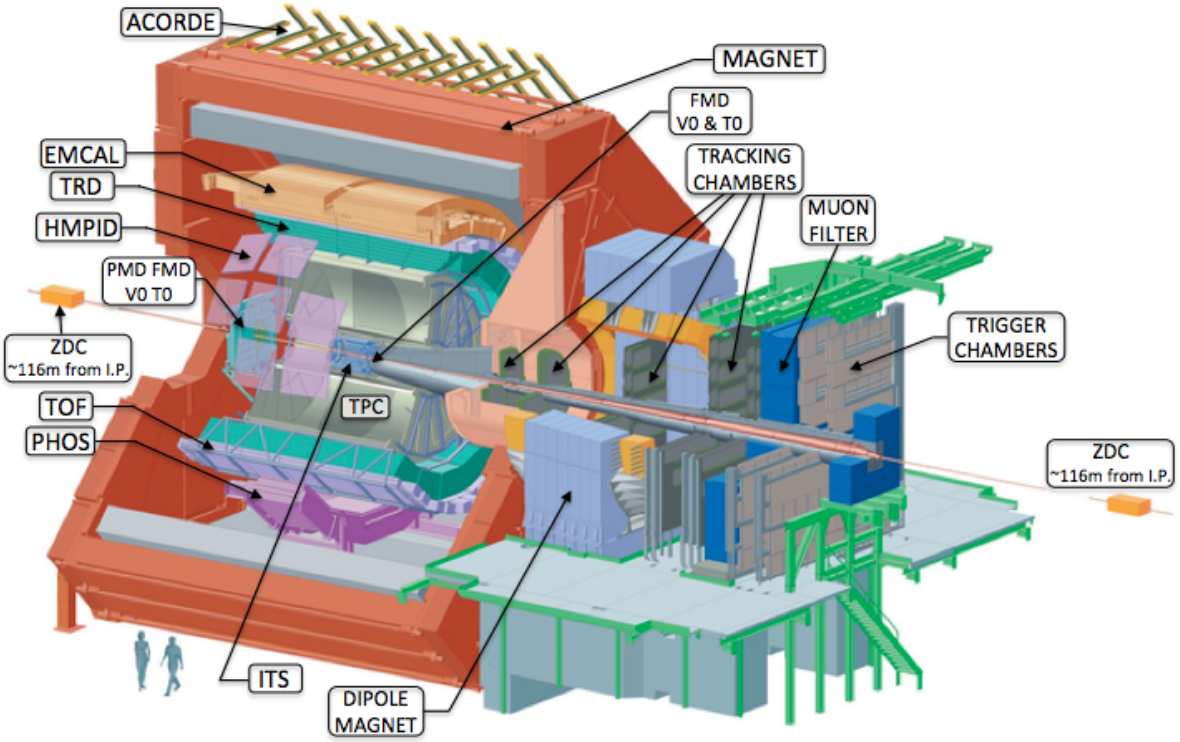

Figure 4.1: Schematic view of ALICE detector

A set of four detectors in the central region of ALICE, cover the mid-rapidity region $-0.9 < \eta < 0.9$ over the full azimuthal angle. The main tasks of these detectors are tracking and particle identification in a very high-multiplicity environment. These are, in order of increasing radii: The Inner Tracking System (ITS) with six layers of high-resolution silicon detectors, the Time-Projection Chamber (TPC) as the main tracking device of the AL-

ICE experiment, the Transition-Radiation Detector (TRD) for tracking in the central region improving p_t resolution at high momentum, and the Time-Of-Flight (TOF) detector for charged-hadron identification. Also in the central region but covering a significantly smaller region of phase space are placed: the Photon Spectrometer (PHOS), the Electromagnetic Calorimeter (EMCal) and the High-Momentum Particle Identification (HMPID) and the ALICE Cosmic Ray Detector (ACORDE).

In the forward regions, the forward scintillator hodoscopes (VZERO) are used for triggering and the Zero Degree Calorimeter (ZDCs) for measuring the interaction remnants of the nuclear collisions. The forward MUON spectrometer, which is optimised for the study of heavy quarkonia via muon decay channel, locates in the C side of the ALICE experiment (on the right hand in Fig. 4.1). An absorber in front before it absorbs the hadronic background. Other detectors in the forward region are the Photon Multiplicity Detector (PMD) aimed to measure the photon multiplicity distribution in the pseudo-rapidity range $2.3 < \eta < 3.7$, the Forward Multiplicity Detector (FMD) to measure the charged-particle multiplicity over a large fraction of phase space ($-3.4 < \eta < -1.7$, $-1.7 < \eta < -5.0$) in full azimuth, the V0 detector used as minimum-bias trigger and the T0 detector to measure the collision time with a precision of 25 ps, in order to serve as a reference time for the TOF detector and to determine the vertex position of about 1.5 cm.

In the following a detailed description is given only of the detectors involved in cosmic ray studies.

4.2 The detectors used to trigger on atmospheric muons

4.2.1 Inner Tracking System (ITS)

The ITS consists of six concentric cylindrical layers of high resolution silicon detectors, the Silicon Pixel Detectors (SPD), the Silicon Drift Detectors (SDD) and the Silicon Strip Detectors (SSD), ranging from a radial position of 3.9 cm to 43 cm from the beam axis (Fig. 4.2) [1]. Two layers of SPD and two layers of SDD, that are high-granularity devices, were chosen as the innermost layers of the ITS. These four layers are surrounded by two layers of double-sided SSD where the requirements in terms of granularity are less strict.

The ITS, providing precise space point measurements, is aimed to localise

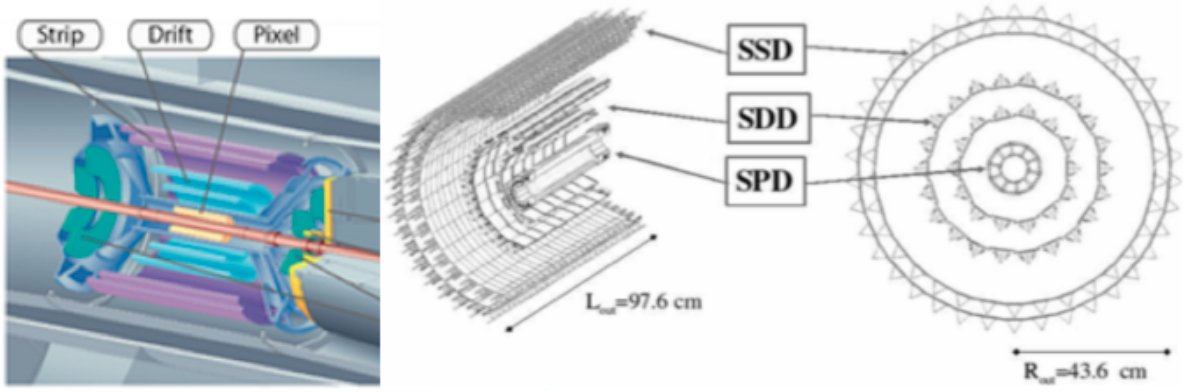

Figure 4.2: Layout of the ITS.

the primary vertex with a resolution better than 100 μm, to track and identify particles with momentum below 200 MeV/c, to improve the momentum and angle resolution for particles reconstructed by the TPC and to reconstruct particles traversing dead regions of the TPC.

The SDD and SSD have analog readout and measure energy loss dE/dx for particle identification at low momenta. In addition, the SPD is included in the minimum-bias trigger logic, which requires at least one charged particle detected by one of the VZERO counters or by the SPD in coincidence with passing bunches.

SPD was incorporated as a dedicated trigger for cosmic rays during 2010 cosmic data taking, requiring a coincidence between signals in the top and bottom halves of the outermost layer (Section 4.4).

4.2.2 Time of Flight detector (TOF)

TOF is mainly aimed to identify particles like protons, kaons and pions by measuring time between the collision and the arrival of particles to the detector. It is a cylindrical array of multi-gap resistive-plate chambers (MRPC) that completely surrounds the outer radius of the TPC. It covers the pseudo–rapidity region ($|\eta| < 0.9$) for particle identification in the intermediate momentum range. The TOF, coupled with the ITS and TPC for track and vertex reconstruction and for dE/dx measurements in the low momentum range (up to about 1 GeV/c) provides event-by-event identification of large samples of pions, kaons and protons.

TOF has a modular structure composed by 18 sectors in ϕ and 5 segments in z direction (beam axis). There is a supermodule framework for each of

the 18 sectors, containing five modules in a row. A schematic layout of one supermodule inside ALICE space-frame is shown in Fig. 4.3. Each module of TOF consists of MRPC strips (15 in the central, 19 in the intermediate and in the external modules) closed inside a box that defines and seals the gas volume and supports the external front-end electronics and services.

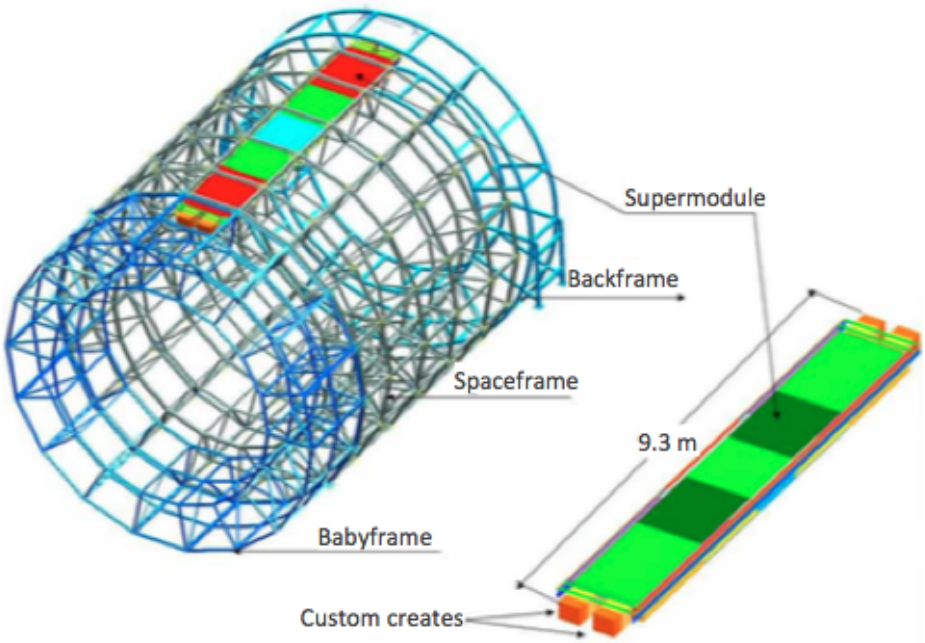

Figure 4.3: Schematic drawing of one TOF supermodule, consisting of 5 modules, in the ALICE space-frame [3].

The MRPC are stacks of very thin structures (250 μm) featuring a high and uniform electric field. A gas mixture of $C_2H_2F_4$(90%)/i–C_4H_{10}(5%)/SF_6(5%) guaranties that any traversing particle immediately triggers an avalanche achieving a good time resolution of about 40 ps. The whole device is inscribed in a cylindrical shell with an internal radius of 370 cm and an external one of 399 cm. The thickness corresponds to 30% of a radiation length.

Uncertainties like the exact time of the interaction affect the time of flight measurements for single particles in such a way that the resolution becomes around 100 ps.

TOF provides a pre-trigger signal to the TRD and a L0[1] trigger for ultra-peripheral collisions. It has also been incorporated as the main trigger into the cosmic-ray physics program. The configuration of the trigger system for cosmic rays in ALICE, is discussed in Section 4.4.

[1] Triggers in ALICE are divided in three levels (L0, L1, L2). More details in Section 4.4.

4.2.3 The ALICE Cosmic Ray Detector (ACORDE)

The detector ACORDE provides the trigger setup configuration to detect cosmic muons, as well as a spatial position when atmospheric muons hit the ALICE magnet. It consists of an array of 60 scintillator modules located on the three top octants of the ALICE magnet, covering 10% of its surface area and has an azimuthal coverage of $-60^\circ < \phi < 60^\circ$ (Fig. 4.4).

Figure 4.4: Photograph of the ACORDE scintillator module array.

ACORDE has been a very important piece of ALICE providing L0 trigger signals when atmospheric muons impinge upon the ALICE detector. These fast signals have been used for commissioning, calibration and alignment procedures of some of the ALICE central detectors.

A single ACORDE module consists of two plastic scintillator padless, each with active area of 188 x 20 cm^2 and 10 mm thickness, plus two Photomultiplier tubes (PMT) placed at the end of each scintillator. They are installed on top of each other with the readout in coincidence.

Details of ACORDE as cosmic trigger are explained in Section 4.4.

4.3 The detector used to track cosmic muons

4.3.1 Time Projection Chamber (TPC)

The ALICE TPC is the largest detector of its type ever built. It is the main tracking detector of the central barrel and is optimised to provide, together

with the other central barrel detectors, charged-particle momentum measurements with good-track separation, particle identification and vertex definition. The phase space covered by the TPC in pseudo-rapidity is $|\eta| < 0.9$ for tracks with full radial track length (matches in ITS, TRD and the TOF detectors) while the acceptance up to $|\eta| < 1.5$ is accessible for reduced track length. The full azimuth is covered. Particles with a p_t from about 100 MeV/c up to 100 GeV/c can be measured with good momentum resolution.

The TPC has an inner radius of about 85 cm, an outer radius of 280 cm and a total length of 500 cm along the LHC beam direction. The active volume of the detector comprises a cylindrical gas volume (90 m^3) filled with $Ne/CO_2/N_2$ (85.7/9.5/4.8)% gas mixture. This volume is divided into two halves by a high voltage central membrane (Fig. 4.5).

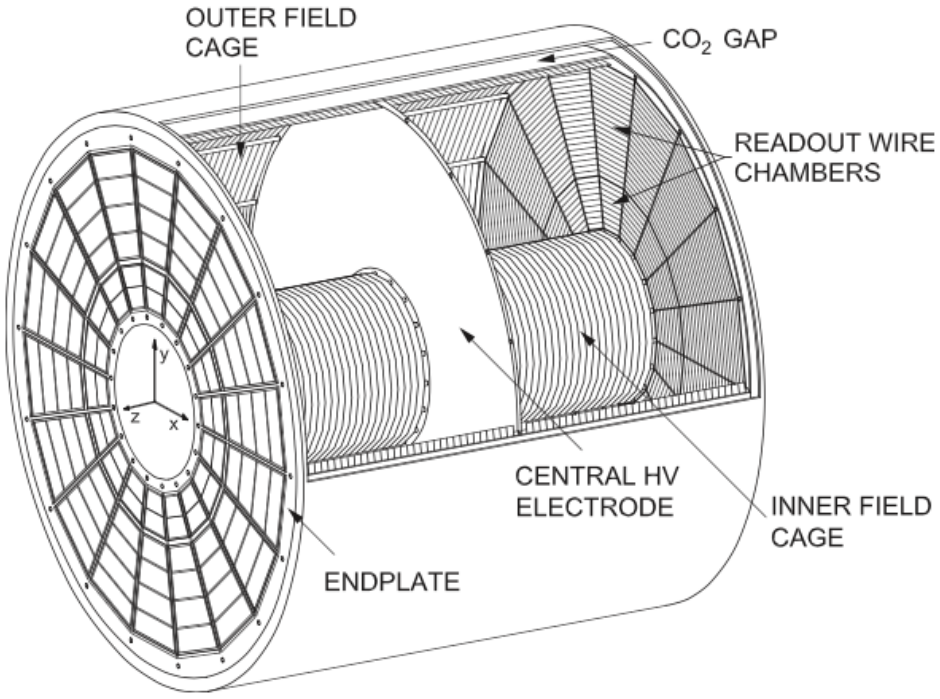

Figure 4.5: 3D view of the TPC field cage [3].

At each end of the cylindrical volume there are multi-wire proportional chambers with pad readout, mounted into 18 trapezoidal sectors at each end plates.

A maximum of 159 clusters can be measured for a typical track, allowing up to 20 000 tracks in one event to be reconstructed and identified. The readout comprises about 557 568 channels because of the high granularity. The position resolution for the inner/outer radii is 1100/800 μm in the transverse

plane and 1250/1100 μs along the beam axis. The charge collected at the end plate is proportional to the energy loss of particles in the gas mixture. The TPC is the slowest detector in ALICE, being its drift time equal to 94 μs. This is important to be taken into account for the trigger, because once an event is accepted, no other event is measured with the TPC within the next 94 μs.

The use of TPC to reconstruct the trajectories of cosmic muons traversing the active volume of the detector is explained in Section 5.1.

4.4 Trigger system for cosmic rays in ALICE

The trigger system

Three detector subsystems were used to provide dedicated triggers to study the muonic component of extensive air showers from cosmic rays: TOF [108], ACORDE [109] and SPD [110]. They were used, in combination with the ALICE TPC to collect single atmospheric muons and muon bundles in order to study high-energy cosmic rays in the region of the knee (3×10^{15} eV) of the cosmic ray spectrum.

The trigger architecture of ALICE consists of two main steps: the low-level trigger is a hardware trigger called Central Trigger Processor (CTP) and the High-Level Trigger (HLT) is implemented as a pure software trigger [111]. The CTP is related with the readout, and combines inputs from different detector subsystems. The HLT receives a copy of the data read out from each subdetector and processes it. The CTP combines the trigger signals of the various subdetectors to decide if an event is accepted, in which case its information is written to disk to be processed by the HLT.

In ALICE there are 3 trigger levels (L0, L1, L2) and for each of them 2 sublevels are present: sub-level *b* meaning before vetoes and sub-level *a* meaning after vetoes. The three trigger levels reduce the event rate depending on the input signals. The first level L0 is delivered after 1.2 μs, the second level L1 after 6.5 μs, and the final trigger signal L2 is delivered after 100 μs, upon completion of the drift time in the TPC. Only after a L2 trigger the event is finally stored. In particular L0*b* gives the number of times a given trigger is fired, while L2*a* gives the number of times the same trigger passes the CTP decision as well as the detector dead time and any other vetoes. These trigger scalers and in particular the ratio L2*a*/L0*b* gives the estimate of the live time

of the detectors for the specific trigger used.

The ALICE "cosmic" trigger detectors provide fast L0 signals to the CTP, when atmospheric muons hit the ALICE detector. Consequently the CTP processes and synchronises the information from trigger detectors and sends the correct sequences of trigger signals to all detectors to perform the readout of relevant events. Besides of providing multi-coincidence trigger signals, cosmic trigger detectors store kinematic information from atmospheric muons. This system was configured to select atmospheric muons with zenithal angles between 0° and 60°, and azimuthal angles from 0° to 360°.

TOF as the main trigger

The ALICE TOF detector is a fast-response device, well suited for triggering purposes. It requires a signal in a pad corresponding to a cluster of readout channels covering an area of 500 cm^2 in the upper part of the detector and another signal in a pad in the opposite lower part forming a back-to-back coincidence (OB0) with respect to the central axis of the detector. With a back-to-back coincidence the trigger rate is higher than 10 Hz. The configuration of the pads involved in the trigger can be changed via software. In some periods of data taking, this flexibility has been exploited to require a signal in an upper pad and in the opposing pad plus the two adjacent pads forming a back-to-back$\pm$1 coincidence (OB1), which gives rise to a better trigger rate allowing to register higher muon multiplicities. The OB3 configuration consists of a back-to-back$\pm$3 coincidence and allows to reach a rate of $\sim$70-80 Hz. Two of the three trigger configurations implemented in our data sample (OB0 and OB3) are illustrated in the first panel (a) of figure 4.6.

ACORDE

ACORDE have been traditionally used as "cosmic" trigger for alignment and calibration purposes of the ALICE central detectors, thus becoming a very important trigger detector for cosmic-ray studies. The trigger ACORDE was formed by the coincidence of signals in two different modules (a two-fold coincidence), although the trigger can also be configured to select events when a single module fires or when more than two modules fire (a n-fold coincidence). The rate of a single hit is about 100 Hz while the obtained rate for

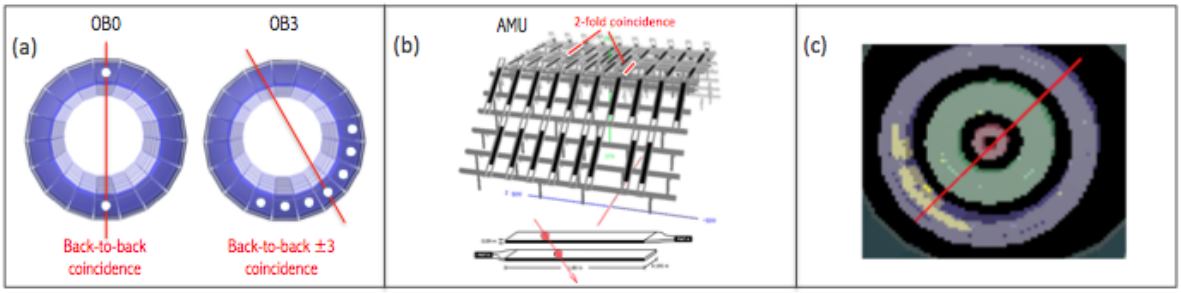

Figure 4.6: Examples of cosmic trigger configurations. (a) Two trigger configurations from signal coincidences using TOF trigger (OB0 and OB3); (b) scheme of a module of ACORDE formed by two scintillators fired by a single atmospheric muon (bottom), and the representation of the 2-fold coincidence (AMU) with two modules fired (top); (c) schematic representation of a SPD trigger (SCO).

two-fold coincidence (AMU)[2] configuration is about 1 Hz. Two configurations of ACORDE trigger are illustrated in the panel (b) of Fig. 4.6.

A compromise should be established when selecting trigger configurations, because higher trigger rate usually means lower purity[3].

SPD

The SPD was incorporated into the trigger system by requiring a coincidence between signals in the top and bottom halves of the outermost layer. This trigger class is denominated SCO[4] trigger and is represented in the panel (c) of Fig. 4.6. This trigger has few contributions to the statistics of atmospheric muons because of its small size, however was not neglected since gave rise to some multi-muon events with a very good purity.

Trigger efficiency

Cosmic ray data were acquired with a combination (logical OR) of at least two out of the three trigger conditions (ACORDE, SPD and TOF) depending on the run period.

The trigger efficiency was carefully determined with real data and simulations. Characteristics like the cylindrical geometry and large area of the TOF detector, surrounding the TPC, make this detector ideal for triggering the atmospheric muons traversing ALICE. The efficiency of the TOF trigger as a

[2] ACORDE MUlti-coincidence
[3] The purity indicates how many tracks are reconstructed in the TPC from the total number of L0 triggers.
[4] SPD COsmic

function of the muon multiplicity is shown in Fig. 4.7. The efficiency is very small at low multiplicities due to the back-to-back coincidence requirement of the TOF (OB0) trigger. This pad configuration contributed to cut many single muon events, such as those close to the vertical direction, specially when do not traverse the central area of the TPC by the central vertical axis.

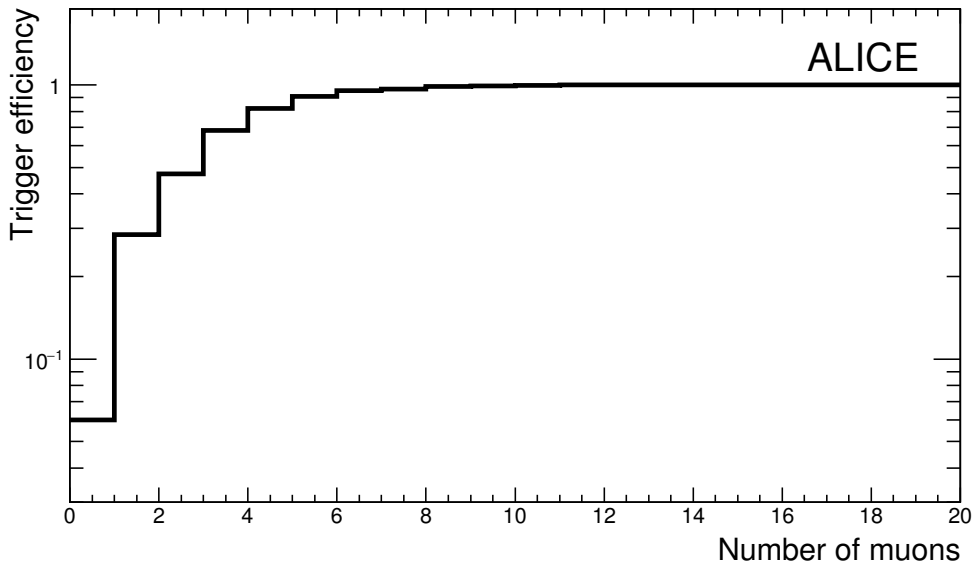

Figure 4.7: Trigger efficiency of TOF trigger.

The efficiency of the ACORDE trigger has a similar, increasing trend with the muon multiplicity. The multiplicities at which the two triggers reach full (100%) efficiency are $N_\mu > 10$ (TOF) and $N_\mu > 15$ (ACORDE).

Given the much smaller area of the SPD in comparison with the TPC, the efficiency of the SPD trigger is significantly lower than both ACORDE and TOF, although the purity was high. It makes only a minor contribution to the muon multiplicity distribution in the low-to-intermediate range of muon multiplicities.

Given the nature and topology of high multiplicity events, all trigger conditions contributed to them with close to 100% efficiency.

4.5 The ALICE location and its environment

ALICE has a global and a local coordinate system. The global coordinate system is a right-handed orthogonal system with the origin at the beam interaction

point. The reconstruction softwares in ALICE use the local coordinate system of the central tracking detectors. Both systems can be transformed one into other by a simple rotation around the z axis.

In this work, with the purpose of studying cosmic rays, the global coordinate system of ALICE was adopted, in such a way that the z axis is aligned with the LHC beam pipe (see figure 4.8) but the azimuthal and polar angles were transformed in order to describe the arrival direction of atmospheric muons. The cosmic–ray coordinate system can be defined as follows:

- **origin of the system** $x = y = z = 0$ at the nominal interaction point;
- **the** x**–axis** perpendicular to the local beam direction, aligned with the horizontal mid-plane of the ALICE TPC, pointing towards the centre of the LHC;
- **the** y**–axis** perpendicular to the plane xz, pointing upwards;
- **the** z**–axis** parallel to the LHC beam pipe. Positive z axis points towards side A (see Fig. 4.8);
- **the azimuthal angle** ϕ is measured at plane xz and increases clockwise from x ($\phi = 0$) up to 360°.
- **the zenithal angle** θ is measured with respect to the vertical y–axis and increases from $\theta = 0$ to $\theta = \pi/2$

The ALICE environment

A detailed description of the ALICE experimental cavern plus the overburden rock, is used to reproduce the ALICE environment in our Monte Carlo simulations. Atmospheric muons arriving at the ALICE location experience meaningful physical effects due to the traversed material between the surface and the apparatus.

The ALICE detector is located 52 m underground, at Point 2 of the LHC accelerator tunnel, in the commune of Saint Genis Pouilly, France. The surface altitude is 450 m above sea level. The location of the ALICE apparatus has 28 m of overburden consisting of subalpine molasse rock. Only muons with an energy E_{th}, at the surface, larger than 16 GeV reach the detectors. The composition of the rock is known from previous geological surveys carried

out for civil engineering purposes at L3–LEP experiment [112]. The molasse density is 2.40 g/cm^3 and the elemental composition can be seen in Table 4.1

Element	H	C	O	Na	Mg	Al	Si	K	Ca	Fe
Percentage (%)	0.8	4.3	48.5	0.7	4.2	3.7	21.5	2.3	10.0	4.4

Table 4.1: Composition of the overburden rock (molasse) above ALICE.

The detector was placed in a large experimental cavern equipped with access shafts, as shown in Fig. 4.8. A large assembly hall was built over the PX24 shaft which gives access to the underground cavern.

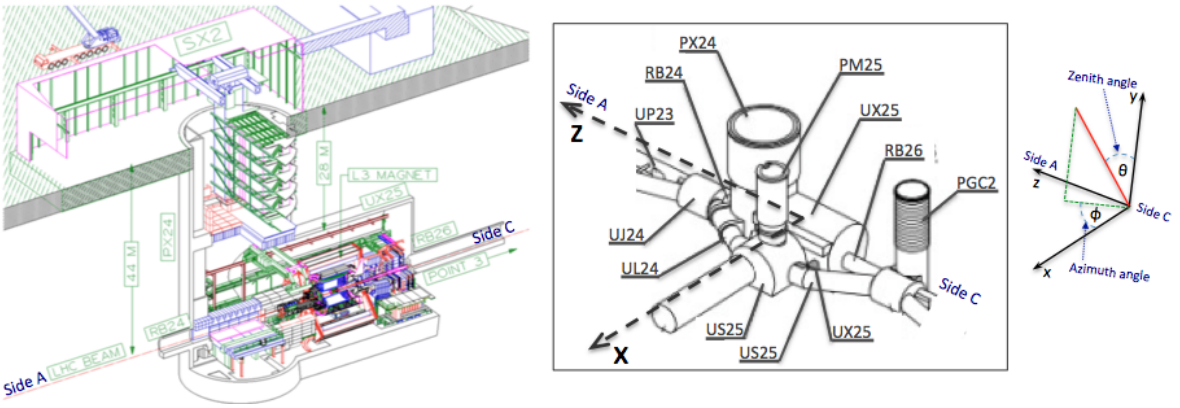

Figure 4.8: Scheme of the ALICE cavern. A sketch of the main shafts is shown on the right, together with the adopted coordinate system.

The most relevant shafts are:

- PX24: The main access shaft, with diameter of 23 m, provides a 15×15 m^2 opening for the installation of magnets and detector units. In addition, accommodates the counting rooms of the ALICE experiments. The LHC beam line passes directly through the shaft bottom. This shaft is located at $\phi = 90°$.
- PM25: This shaft, with 8.4 m diameter, allows accessing to the machine bypass area and, via two access tunnels on each side of the ALICE detector, gives a second access to the main experimental cavern. Its azimuthal location is $\phi = 0°, 360°$.
- PGC2: The PGC2 shaft, with 12 m diameter, is located downstream of the ALICE detector where the machine bypass tunnel and the beam tunnel coincide. It is located at $\phi = 270°$.

5 Event reconstruction

5.1 Atmospheric muon reconstruction

The ALICE TPC was used to reconstruct the trajectory of cosmic muons passing through the active volume of the detector with full spatial information. Some of the most relevant characteristics are summarised in 4.3.1. For the purpose of this thesis we exploited what we consider the main advantages of this detector: the excellent tracking capabilities.

The TPC, main tracking detector in the central barrel, provides the charge particle track reconstruction with a very good two-track separation. It was designed to detect particles stemming from the LHC beam collisions. However, there are differences between particles emerging from LHC beam collisions and atmospheric muons traversing the TPC. A particle created in a collision passes very close to the centre of ALICE, and generates a track either in the upper half of the TPC or in the lower half. In contrast, an atmospheric muon vertically crosses the TPC, usually far from the central axis, and its track often traverses the whole length of the TPC.

5.1.1 Tracking algorithm

The TPC tracking algorithm [113], in the ALICE experiment, was designed to reconstruct tracks coming from the primary interaction vertex during the LHC beam collisions. It follows the Kalman filter procedure [114] that allows to find and fit tracks by working inwards from the outer radius of the detector, where, during collider operations, the track density is lower. According to the Kalman filter, the propagation of track parameters like position, direction, curvature and its associate covariance matrix to the next pad row, is recursively done. The reconstructed tracks are conformed by specific clusters[1]. If a cluster

[1] Particles interacting with the detector leave a signal in several adjacent space points or in several time bins of the detector. These signals are combined to form a cluster.

is found to fit the track, it is added to that track candidate, with the subsequent updating of its parameters and covariance matrix. The track parameters and the corresponding covariance matrices can be treated as "seeds". The seed candidates are built first with two TPC clusters and the vertex point, then with three clusters and without requiring that the seeds point to the primary vertex. This is recursively repeated according to the reduced χ^2. The resulting tracks only have information from the TPC and are saved in the reconstruction output. This is complemented with the information from other detectors when the tracks are covered by their respective acceptance range producing the so-called global-tracks. The reconstruction software produces analysis objects in the format called Event-Summary Data (ESD), containing high-level information related to the event vertex position, parameters of reconstructed charged particles with their PID information, secondary vertex candidates and integrated signals of certain subdetectors.

In case of atmospheric muons, there is no primary vertex since the muon tracks can be originated anywhere in the active volume of the TPC. Thus, this analysis used the same tracking algorithm but removing any vertex constraint such that muons are not forced to cross the nominal collision point in order to be reconstructed.

As the track search is performed from the larger TPC radius to the inner one, cosmic ray muons are typically reconstructed as two separate tracks in the upper and lower halves of the TPC. We refer to these tracks as *up* and *down* tracks. This is shown in figure 5.1 where two event cases are represented: a single-muon and a multi-muon event. Hereinafter another algorithm is used to match every *up* track with its corresponding *down* track, so as to obtain the entire muon track.

5.1.2 Matching algorithm and track selection

A complete analysis of the muon events reconstructed by the tracking TPC algorithm, entails a second stage aimed to reconstruct the full trajectory of the muons by matching each *up* track with its corresponding *down* track, in such a way that double counting can be eliminated. In order to make an unambiguous matching of tracks, the algorithm was first implemented analysing single muon events with two tracks in the real data. After this first stage, the algorithm was improved step by step using muon bundles and comparing the results with the event display of the events. Then to optimise the cut values

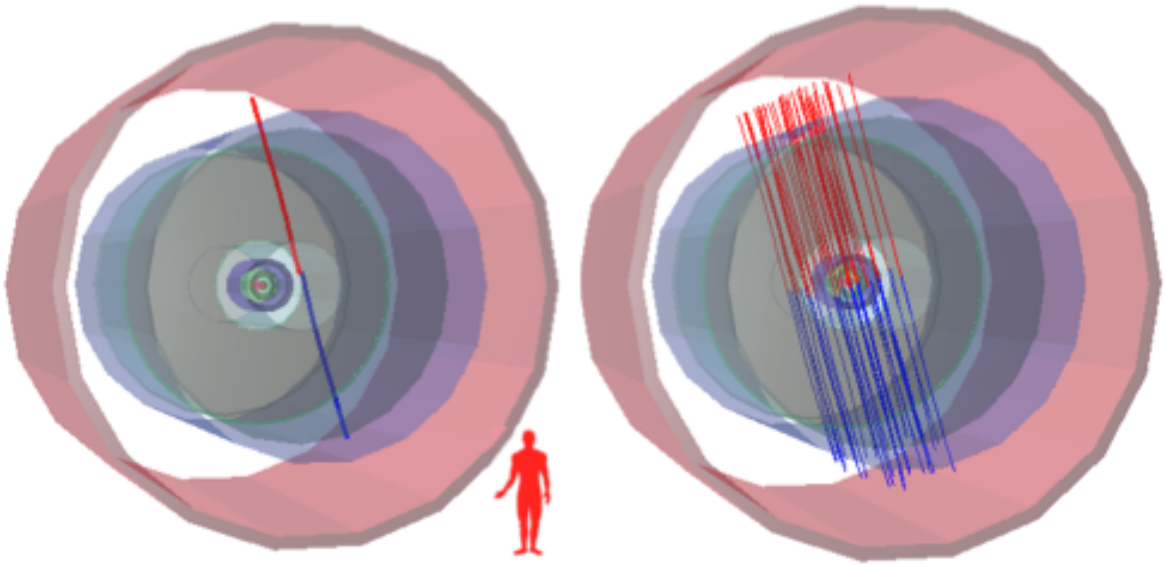

Figure 5.1: Two cases of muon events. Muons are usually reconstructed as two TPC tracks, one in the upper half of the detector (*up* track) in red, and the other in the lower half (*down* track) in blue.

and work with high multiplicity events the matching algorithm was analysed using simulated events up to multiplicities of hundred of muons.

Because of the amount of pad rows in the TPC readout chambers, the tracking algorithm makes possible to reconstruct single tracks (*up* or *down*), with up to 159 clusters within the TPC volume. In our procedure, each track was required to have 50 space points (clusters) at the minimum, thus maximizing the detector acceptance and avoiding the loss of short muon tracks.

In events where the magnetic field was *on*, a momentum cut, $p > 0.5$ GeV/c, was imposed on the tracks to eliminate all possible electromagnetic background.

The parallelism between the selected tracks is a very important requirement for the reconstruction process of multi-muon events, since the atmospheric muons coming from the same EAS arrive almost parallel at ground level. With this aim, a double loop is performed in order to check the scalar product of the direction between every pair of tracks $\left(\vec{t_1},\vec{t_2}\right)$. The parallelism condition is fulfilled when $\vec{t_1}\cdot\vec{t_2} = \cos(\Delta\phi) > 0.990$. The first loop is performed for every analysed track $\vec{t_a}$ to define all the parallel tracks and in particular the track with the largest number of associated parallel tracks called reference track $\vec{t_r}$. With the second loop, all the tracks fulfilling the parallelism condition with regard to the reference track ($\vec{t_a}\cdot\vec{t_r} = \cos(\Delta\phi) > 0.990$) are finally selected as

muon-track candidates.

The parallelism requirement introduces an additional momentum cut to the bending of muon tracks in the magnetic field. The momentum cut is a function of the azimuth angle of the muon track and varies between 1 and 2 GeV/c. After all of these cuts on the reconstructed tracks we can start the algorithm to match the tracks.

The maximum distance allowed between every pair of analysed tracks (*up* and *down*) to be matched, in the horizontal mid plane of the TPC, was systematically studied and it was finally chosen as $d_{xz}^{max} = 3$ cm. This value is large enough to maximise the matching efficiency in high multiplicity events, while keeping the background to a minimum.

A muon reconstructed with two TPC tracks (*up* and *down*) is called a "matched muon". In addition to the matched muons we also have found "single-track muons", which are those TPC tracks fulfilling all the criteria to be a muon track: number of clusters, momentum and parallelism, but does not have a corresponding track within $d_{xz} < 3$ cm in the opposite side of the TPC. These single-muon tracks are also accepted as muon candidates. Most single-track muons are found to cross the TPC near its ends where part of the muon trajectory falls outside the detector.

The relevant cut values of the matching algorithm are summarised in table 5.1.

Cut Parameter	Value
# TPC clusters	> 50
p	> 0.5 GeV/c
$\cos(\Delta\phi)$	> 0.990
d_{xz}	< 3 cm

Table 5.1: Values of the cuts of the main variables defining an atmospheric muon in the matching algorithm.

During the refinement of the reconstruction algorithm and during the data taking we analysed single-muon events ($N_\mu = 1$) and multi-muon events as the ones shown in figure 5.1. Besides these two cases, a small percentage of "interaction" events was identified. The "interaction" events are those where cosmic muons have interacted with the iron yoke of the magnet producing a shower of particles that pass through the TPC. These events are not typical

atmospheric muon bundles. Actually they are undesirable events that could fulfil all the reconstruction and matching criteria, by introducing a fake counting of supposedly atmospheric muons. An example of this kind of fake muon event is shown in figure 5.2, together with a typical multi-muon event just for comparison.

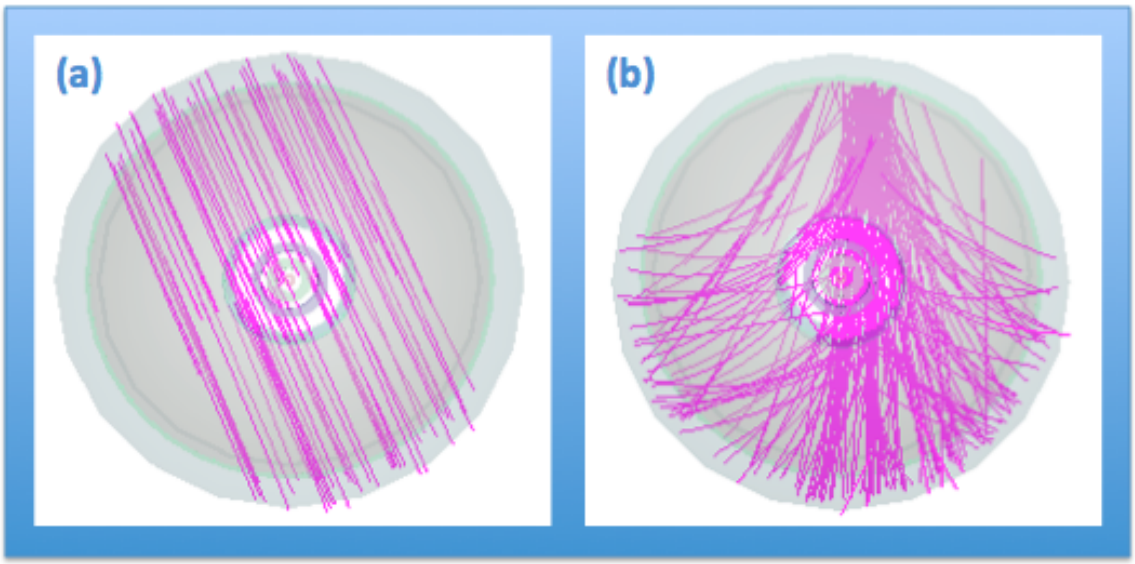

Figure 5.2: Examples of muon events reconstructed by the reconstruction algorithm: (a) standard atmospheric muon event; (b) typical "interaction" event.

Some parameters in the matching algorithm help to differentiate "interaction" events from the standard atmospheric muon events. Usually "interaction" events are characterised by an average distance between tracks, which is much smaller than the distance in the standard atmospheric muon events. Additionally, the ratio between the number of tracks and reconstructed muons (matched and single track muons) is larger in "interaction" events. The condition $N_{\text{tracks}}/N_{\text{muons}} > 2.2$ in the matching algorithm, correlated with a parameter evaluating the average distance between the tracks, allows to discriminate many of these undesirable events. Nevertheless, the events with high multiplicity ($N_{\mu} > 50$) have been checked with ALICE event visualisation interface (event display) to be sure they are produced in an EAS.

The event reconstruction analysis needs also to overcome the difficulties created by inaccuracies associated with the most inclined showers. The tracking algorithm has not been optimised for quasi horizontal tracks, thence the zenith angle of all accepted events was restricted to the range $0^{\circ} < \theta < 50^{\circ}$.

5.2 Performance of tracking and matching algorithms

In order to quantify the performance of the reconstruction algorithm as a whole, we created a Monte Carlo generator where cosmic muons were generated parallel to each other like in a typical EAS. Atmospheric muons were sampled in a surface located at a certain altitude (y level), conveniently chosen as $y = 435$ cm (over TOF) with respect to the mid-plane of the TPC. The central point of the TPC mid-plane represents the origin of coordinates. Such muons were triggered downwards to cross the TPC. In a very flexible way, some user-defined variables can be set: number of muons per event, spatial limits (x and z coordinates) of the sampling area, muon direction (θ, ϕ) range and finally the momentum range. The momentum should be high enough to allow muons to traverse the TPC. This generation was interfaced with AliRoot, producing a *kinematic tree* containing the full Monte Carlo information about the generated particles, e.g. type, momentum and charge. From that point on, the generated muons can reach the TPC and are then propagated with the subsequent detector simulation.

The reconstruction of the simulated events can be done using the same algorithms applied to real events.

With this straightforward procedure, Monte Carlo simulated events were used to study the multiplicity dependence of the reconstruction efficiency. We generated 1000 events for each of the 20 discrete values of the muon multiplicity, varying between 1 and 300, which were then reconstructed.

The histograms of the relative difference between the number of generated muons and its associated reconstructed multiplicity,

$$\left(N_{\text{gen}} - N_{\text{rec}} \right) / N_{\text{gen}}, \tag{5.1}$$

were obtained for the 20 discrete values of generated muons. Selected plots corresponding to $N_\mu = 50$, 70 and 100 muons per event, are shown as example in figure 5.3.

The mean values (MEAN) and root-mean-square (RMS) of the distributions given by the Eq. 5.1 are shown in figure 5.4 as function of the number of generated muons.

The root-mean-square represents the resolution on the number of reconstructed muons and is typically less than 4%, while for the highest multiplicities it is around 2%. This is important in order to choose the optimum bin

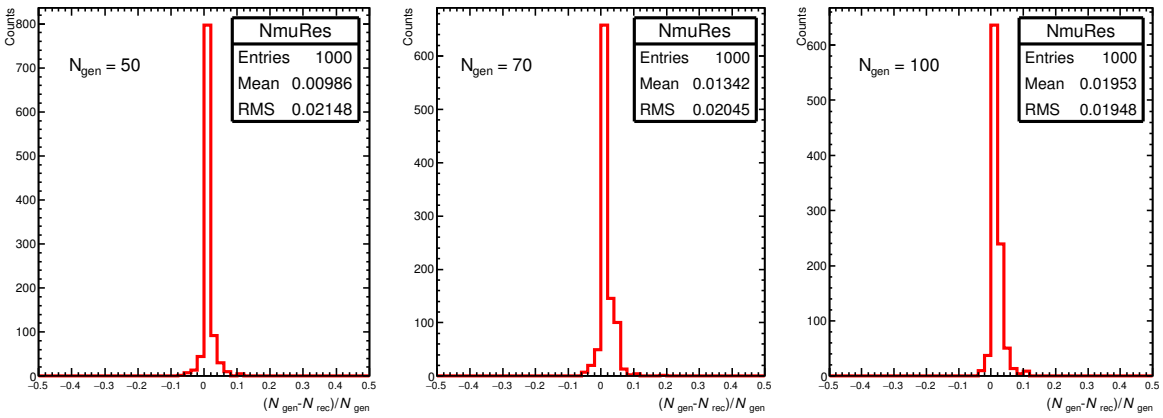

Figure 5.3: Relative difference between the number of generated and reconstructed muons.

width value in the muon multiplicity distribution and avoid migration of entries from bin to bin.

The mean value is an indication of the bias in the reconstructed number of muons, being less than 1% up to $N_\mu \sim 50$ and increasing to 5% at high muon multiplicities ($N_\mu = 300$).

The same generator was used to determine the momentum resolution as a function of the momentum of generated muons, which was evaluated simulating single muon events. In the TPC a momentum value is assigned to each track, however for matched track muons both, *up* and *down* tracks, are important. A new algorithm that uses the covariant matrix of both tracks to fit the trajectory of the entire track length, allows to determine the momentum of atmospheric muons. The covariant momentum was found to give a more accurate momentum estimation of the particle, with respect to either the average momentum value of the two tracks or other estimations based on the error weight of each tracks.

The relative difference between the generated and reconstructed momenta,

$$\left(p_{\text{gen}} - p_{\text{rec}} \right) / p_{\text{gen}}, \tag{5.2}$$

as a function of the generated one, is illustrated in figure 5.5 for p_{gen} = 10, 50 and 100 GeV/c.

The resolution of the covariant momentum was obtained with the root-mean-square of distributions given by equation 5.2 for 20 discrete values of p_{gen}, varying between 1 and 200 GeV/c. As can be seen in figure 5.6 the resolution is lower than 6% for momenta below 120 GeV/c increasing to more

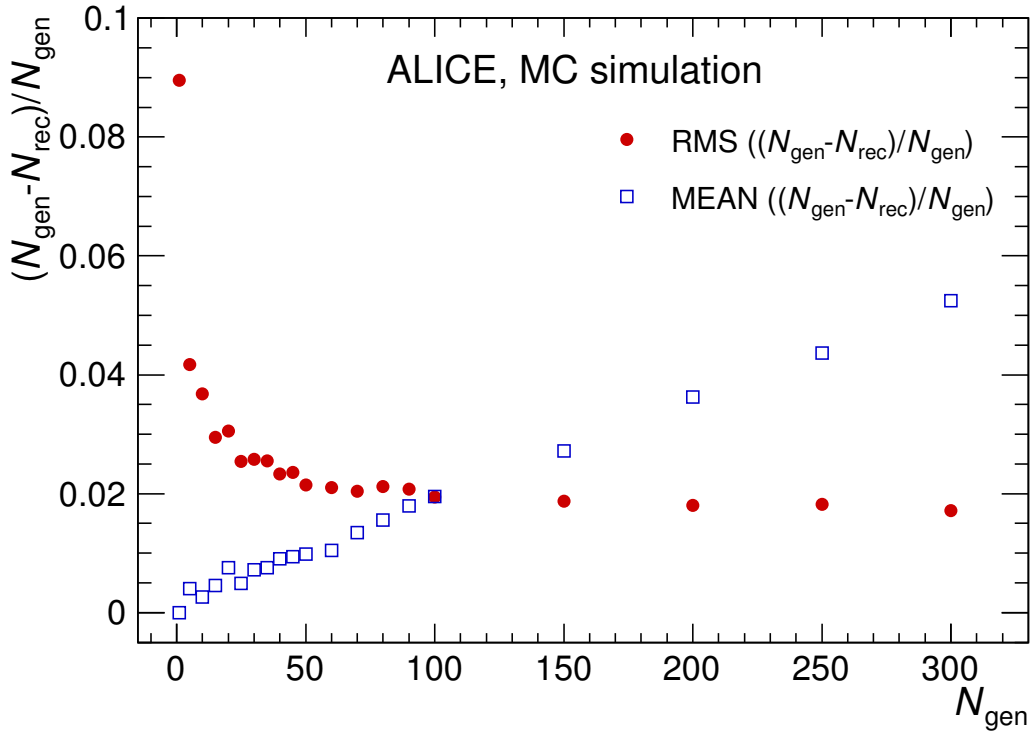

Figure 5.4: Root-mean-square and mean values of the relative difference between the number of generated and reconstructed muons for events simulated with different muon multiplicities.

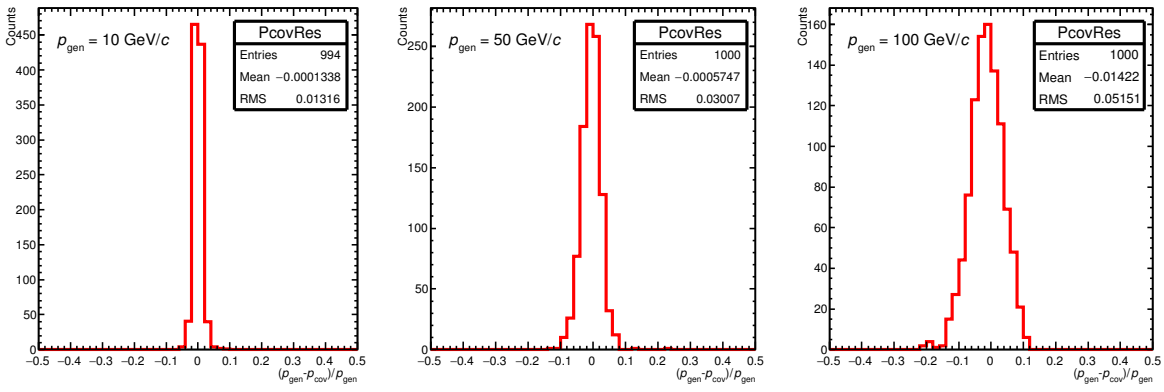

Figure 5.5: Relative difference between the generated and reconstructed momenta of muons for different generated momenta.

than 10% for momenta above 200 GeV/c.

In order to evaluate the similarity between data and Monte Carlo simulation, we determined the ratio of the number of muons reconstructed as single

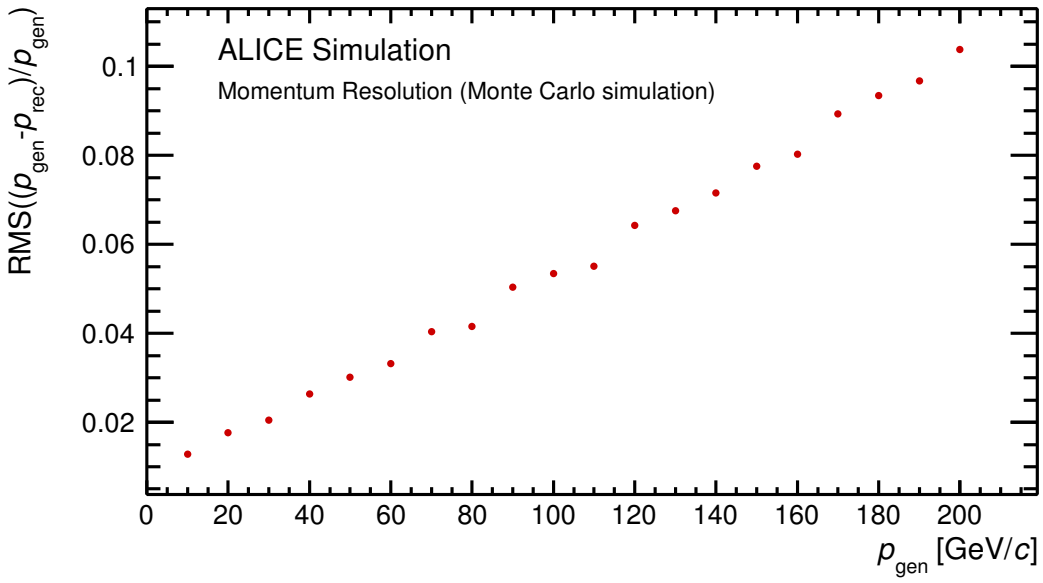

Figure 5.6: Resolution of momentum reconstruction as function of momentum of generated muons by Monte Carlo simulations.

tracks (either *up* or *down* tracks) to the total number of reconstructed muons (both, single and matched tracks) for different multiplicities in the intermediate range $5 \leq N_\mu \leq 18$. The ratio obtained from data was compared with the ratios obtained using a full Monte Carlo simulation where primary cosmic rays with two different compositions, pure proton and pure iron, were generated with CORSIKA (see chapter 6).

This ratio is shown in figure 5.7 as function of the muon multiplicity in the mentioned range. Over the range of muon multiplicities shown, the ratio varies between 0.2 and 0.4 with good agreement between data and simulations. There were not significant difference between the simulated proton and iron samples.

The effects of the environment of ALICE, in particular the rock composition introduced in section 4.5, and the geometry of the cavern with the main shafts (see figure 5.8), was studied comparing data with Monte Carlo events.

A comparison of the attenuation of the number of muons $\left(\frac{dN}{dX}\right)$ as function of the traversed grammage X, from data and MC results, would be a suitable way to estimate the effect of the underground environment upon our results, but the statistics of multi-muon events is poor in our data sample to give a valuable plot (the data sample is further described in section 7.1). Since the

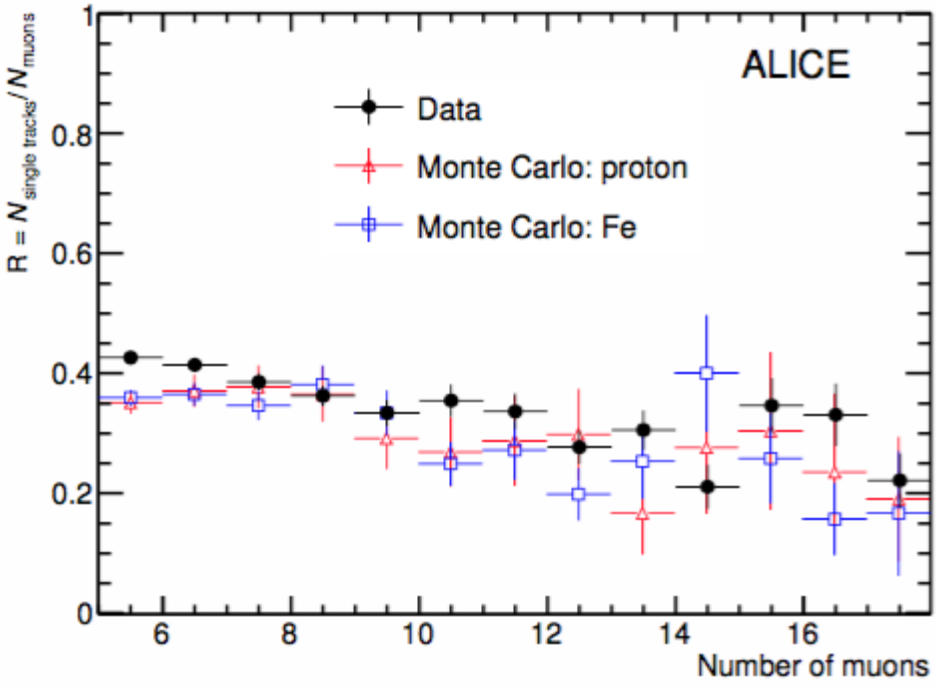

Figure 5.7: The ratio of muons reconstructed as single tracks to the total number of reconstructed muons (both single and matched tracks) in the data and simulations with proton and iron primaries.

integrated density of the mass overburden should depend on the azimuth and zenith angle of the muons traversing it, the influence of modelling the overburden rock and the various access shafts was evaluated by comparing the distributions of the arrival muon directions (zenith *vs* azimuth) with simulations (Fig. 5.9). The whole data sample was used for this study, given that most of the events are single-muon events.

We find a larger rate of atmospheric muons in the directions of the access cavities located in the ALICE cavern, since muons arriving from shaft directions loose less energy in their passage from the surface to the ALICE level with respect to the muons crossing the whole rock. In figure 5.9 we can clearly see the location of the biggest shaft PX24 at $\phi = 90^\circ$ and the location of the shaft PM25 at $\phi = 0^\circ$ and 360°, while the more distant shaft PGC2 at $\phi = 270^\circ$ is less visible.

The lacking of some details related to the underground environment description might give rise, to some extent, to any possible discrepancy between data and simulations. To check the description of the environment simulated with MC, the differences between simulation and data of the zenith *vs* azimuth distribution, are shown in figure 5.10. Scattered points from both, data and simulation, were normalised to the total amount of entries. This plot shows

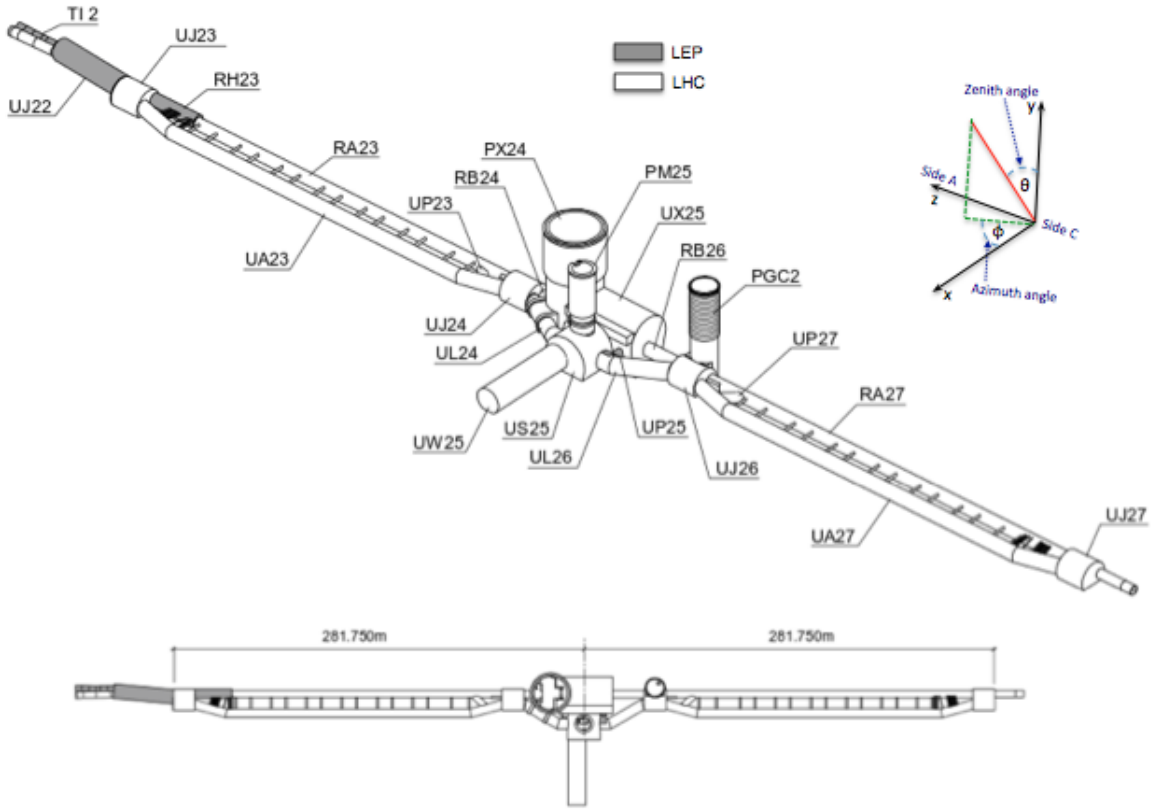

Figure 5.8: Structure of the ALICE cavern with the access shafts to the experimental installation. The coordinate system is also shown.

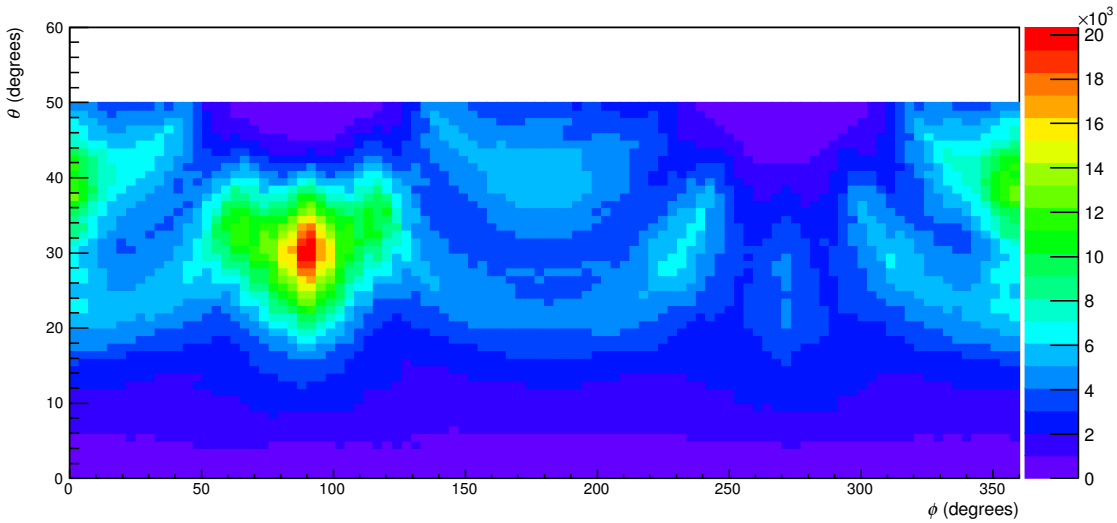

Figure 5.9: Zenith *vs* azimuth distribution of atmospheric muons in the horizontal mid plane of the ALICE TPC, obtained with the data sample taken in 2010-2013.

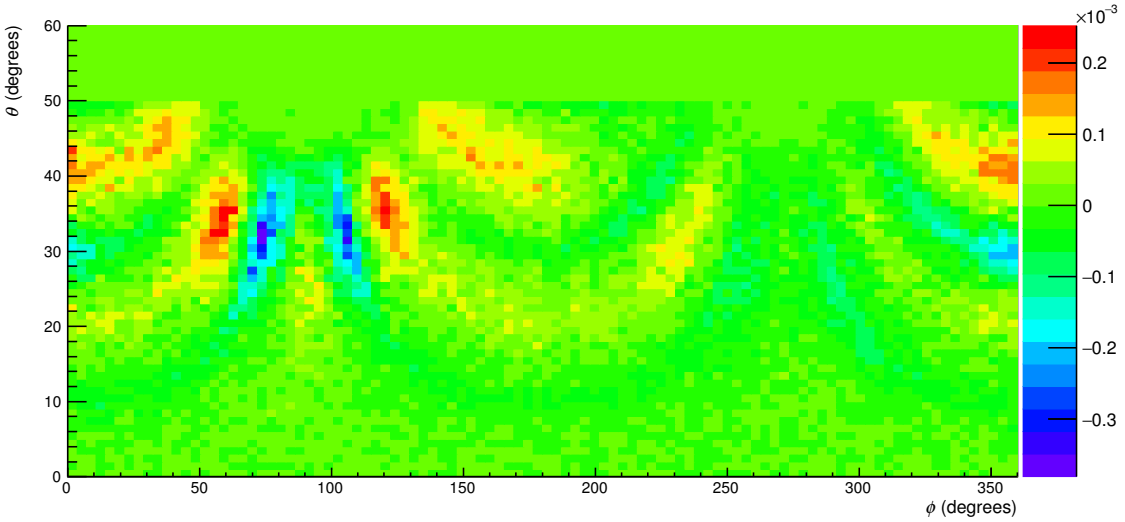

Figure 5.10: Difference between data and MC simulations in the zenith *vs* azimuth distribution of atmospheric muons in the horizontal mid plane of the ALICE TPC.

the position of those zones where some remnant discrepancies arise. This was also checked by plotting the zenith and azimuth projections of the distributions obtained from data and MC. The comparison of the zenith and azimuth projections is shown in figure 5.11.

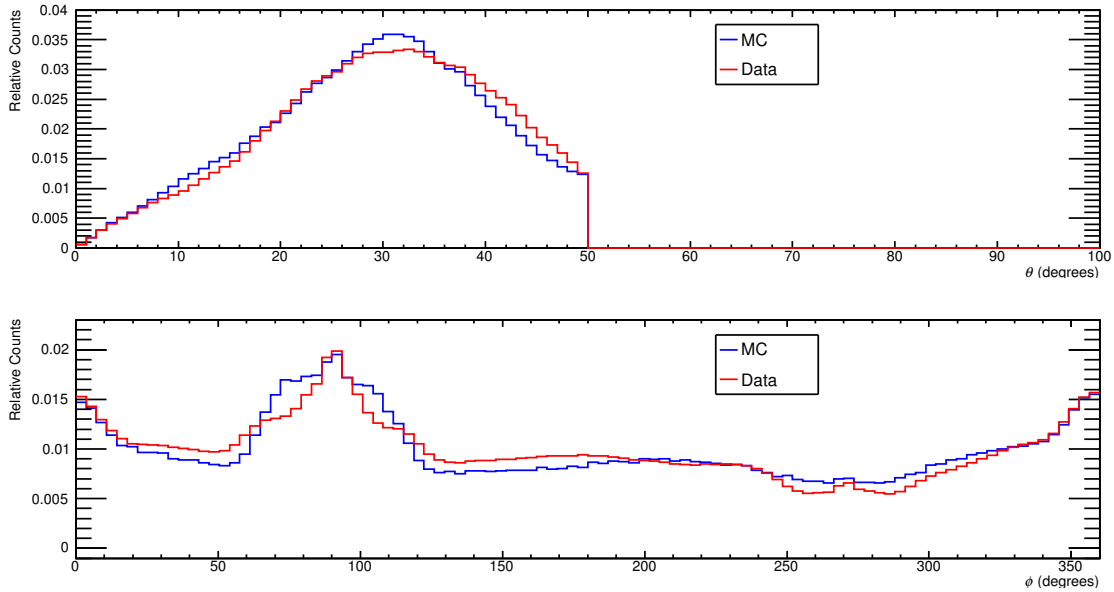

Figure 5.11: Comparison between data and MC simulations of the zenith and azimuth distributions of atmospheric muons in ALICE.

One of the main differences between data and simulations, is found at az-

imuth angles around $\phi = 90^\circ$ where the biggest shaft (PX24) is located. The plot corresponding to the simulated azimuth angular distribution (blue colour) shows a wider shape around $\phi = 90^\circ$ indicating that the shaft PX24 was modelled with dimensions slightly bigger than the real ones. On the other hand, at zenith angles $\theta > 40^\circ$ representing very inclined atmospheric muons, the simulations slightly underestimate the muon contribution.

In general we can say that the description of the rock and the shafts of ALICE with MC simulation satisfactorily describes the angular distributions of the data, suggesting a good modelling of the environment of the experiment.

6 Simulation strategy

6.1 Event generator and hadronic models

In order to explain the muon component detected by ALICE, a proper set of modern Monte Carlo tools is necessary to achieve a suitable EAS simulation. The simulation has to start with the first interaction of the primary cosmic ray with a nucleus of the upper atmosphere and subsequently describe all the EAS development up to the ground level.

The Monte Carlo software CORSIKA[1] [115], originally developed to perform simulations for the KASCADE experiment [116], was adopted in this thesis as event generator of primary cosmic rays. The CORSIKA code incorporates different hadronic interaction models to simulate interactions and decays of nuclei, hadrons, muons, electrons and photons in the atmosphere up to energies of about 10^{20} eV. In this work, two of the more recent CORSIKA versions where used: 6.990 [117] and 7.350 [118]. The main differences reside in the implemented hadronic interaction models with their specific theoretical formalisms and cross-sections data used to describe hadron-air and nucleus-air interactions in EAS.

The main hadronic interaction models included in CORSIKA are DPMJET[2] [119] used to describe interactions involving nuclei through the two-component Dual Parton Model, –EPOS[3] [120] which introduces improvements concerning hard interactions as well as nuclear and high density effect, –NEXUS[4] [121] which extrapolates up to higher energies features of VENUS and QGSJET in a parton model approach for initial stages of nuclear collisions in hadron-hadron interactions, –QGSJET[5] [18, 19] which treats the

[1] **CO**smic **R**ay **SI**mulation for **KA**scade.

[2] **D**ual **P**carton **M**odel with **JET**s.

[3] **E**nergy conserving quantum mechanical multi-scattering approach, based on **P**artons **O**ff-shell remnants and **S**plitting parton ladders.

[4] **NEX**t generation of **U**nified **S**cattering approach

[5] **Q**uark **G**luon **S**tring model with **JET**s

hadronization process in the quark gluon string model and describes high energy hadronic interactions using quasi-eikonal Pomeron[6] parameterization for the elastic hadron-nucleon scattering amplitude, –SIBYLL [122] which is based on the QCD mini-jet model to simulate hadronic interactions at extreme high energies, and –VENUS[7] [123] for ultra-relativistic heavy ion collisions.

All high-energy interaction models mentioned above were developed on a semihard Pome- ron approach, with the exception of SIBYLL which works on a mini-jet scheme. Both approaches are identical in what concerns high p_T hadron production. However, the semihard Pomeron treatment provides an additional contribution, from the low virtuality domain ($|q^2| \simeq p_T^2 < Q_0^2$), to secondary particle production and significantly enhances the predicted inelasticity of hadronic interactions. Actually, in shower simulations is very important the treatment of the transition region between central and peripheral collisions, in particular when the average parton densities grow with the decreasing impact parameter but keeping impact parameters large enough such that no density saturation is reached. In this scenario both, soft and semihard processes, are important to the same extent and give a notable contribution to the interaction characteristics relevant for EAS physics.

In the latest versions of CORSIKA (7.3xx) there are two models including the early LHC data, for the first time, to constraint model parameters: EPOS LHC (v3400) and QGSJET II-04 [19].

In this work we have settle on QGSJET [18, 19] as the model for simulating the generation and development of the EAS. In order to test different versions of the model, we have chosen QGSJET II-03 [18] implemented in CORSIKA version 6.990, and QGSJET II-04 [19] implemented in CORSIKA version 7.350. Both models have, per se, a much more advanced description of the underlying physics with respect to the original QGSJET(01). All versions of QGSJET are developed as Monte Carlo performances of the Quark Gluon String [124] model, which was being generalized to treat nucleus-nucleus collisions and to describe the fragmentation of the nuclear spectator. All of this was done in the framework of the Reggeon Field Theory applying the semihard Pomeron approach (see [125] and references therein). The phenomenological treatment of semihard processes in QGSJET gives rise to hadron jets

[6] Pomeron is a Regge trajectory, a family of particles (composite objects) characterized by vacuum quantum numbers, that could lead to logarithmically rising cross sections of hadronic collisions at high energies.

[7] **V**ery **E**nergetic **N**uclear **S**cattering

of relatively high p_T.

The main difference between QGSJET 01 and QGSJET II lies on the treatment in QGSJET II of the Pomeron-Pomeron interaction (the so-called enhanced diagrams) at any order. A proper focus to non-linear interaction effects, just like parton shadowing and saturation at high parton densities and small impact parameters, as well as screening effects in a high parton density environment produced by Pomeron-Pomeron interactions at high virtuality ($|q^2| > Q_0^2$), have been also developed in the recent models.

In the latest model versions, one notices that QGSJET II-03, implemented in CORSIKA 6.990, underestimates the strange particle production. This aspect was improved in QGSJET II-04 by readjusting some parameters of the hadronization process. In addition, in the latest version QGSJET II-04 stands out the inclusion of loop diagrams, providing smaller screening corrections for hadron-nucleus and nucleus-nucleus collisions. Both improvements resulted in an increase of the muon content in air showers over a wide energy range ($10^{15} < E < 10^{19}$ eV). Another distinctive feature of QGSJET II-04 is the treatment of the remnant of the projectile in hadronic interactions, which is known to significantly influence the muon production in air showers. The break-up of the hadronic remnant results in baryons as well as in charge and neutral mesons in the very forward region of the hadronic interaction. Enhanced baryon break-up lessens the muon production in air showers, while enhanced break-up of mesons increases the amount of muons because the energy fraction going to neutral pions (main component giving rise to the electromagnetic channel, see equation 2.9) produced by meson remnants is reduced. On the other hand, it is important to mention that multi-step hadronic cascade processes contribute to increase the abundance of pion induced collisions, and forward neutral hadron production in pion interactions (e.g. $\pi^+ + p$) has a dominant contribution to the production of ρ^0 mesons by exchanging charge pions (Fig. 6.1). Neutral ρ mesons, subsequently decay with 100% branching ratio into two charged pions ($\pi^+\pi^-$) which in turn may decay by leading to an enhanced multiplicity of high-energy muons in EAS (in the higher atmosphere where air density is low, the pion decay dominates over the pion interactions).

6.2 Monte Carlo simulation

The simulation plan followed in this work is represented in figure 6.2.

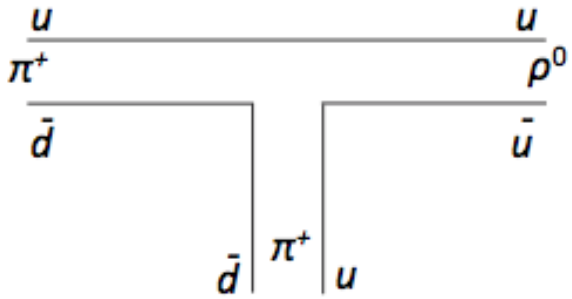

Figure 6.1: Diagram of production of leading ρ^0 meson in pion collisions. This is the case where pion exchange dominates forward hadron production.

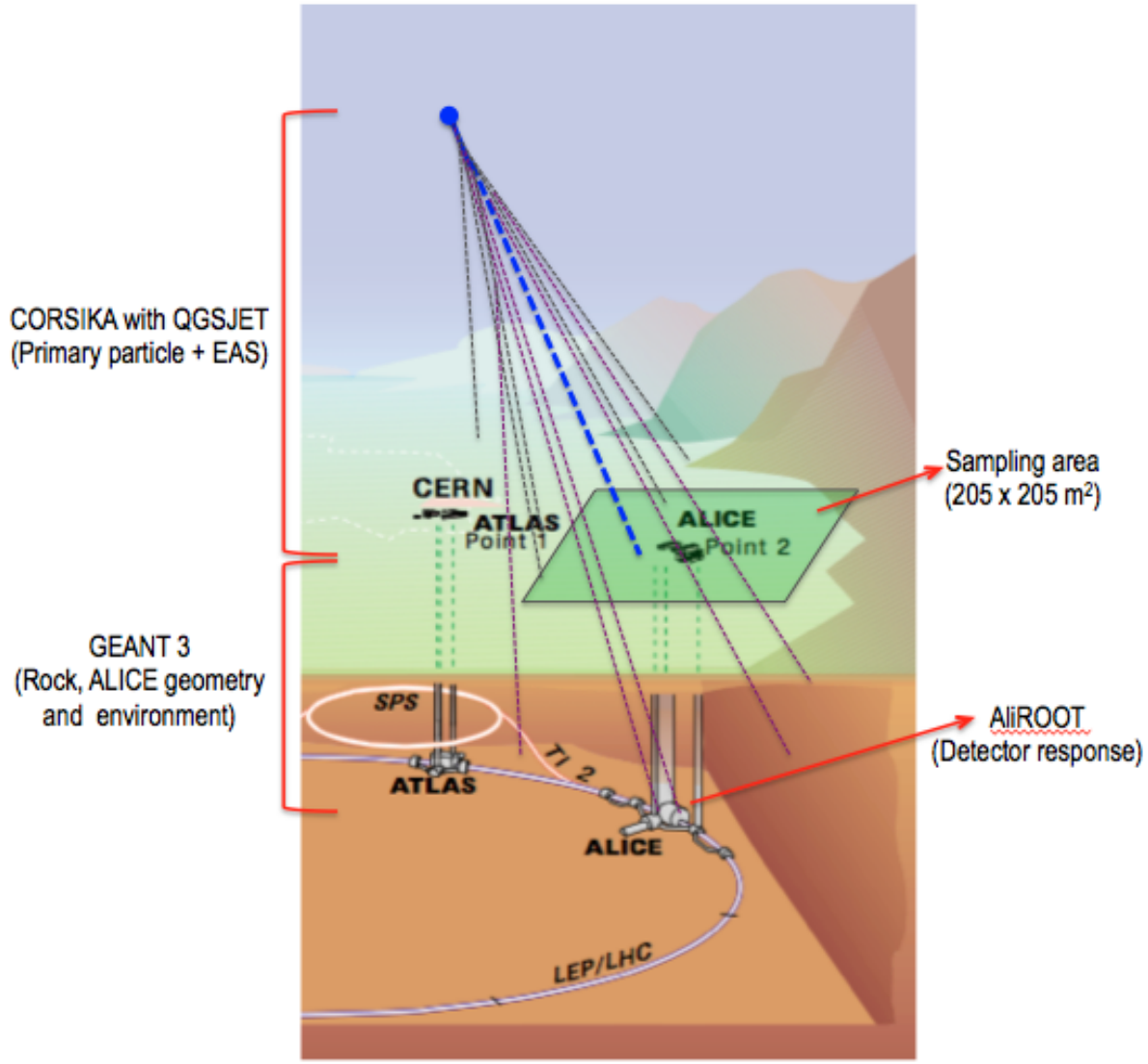

Figure 6.2: Schematic view of the Monte Carlo simulation.

The main steps of the simulation scheme consist of defining the primary particle giving rise to the EAS, performing the shower development through the atmosphere until the observation level, following the propagation of the muons through the rock and the environment around ALICE, as well as simulating the ALICE detector. All muons crossing the TPC active area are treated by a detector response simulation that produces pseudo-raw data which are then processed with the same reconstruction code that is applied to the real data, including the TPC tracking algorithm and the track matching algorithm (Section 5.1) developed for this study.

The sampling area, that is the area at surface level in which the core of the shower (centre of the shower) is randomly scattered, has to be optimised. Actually, a too large area gives a fraction of simulated showers in which no muon crosses the TPC of ALICE to the detriment of the simulation efficiency. On the contrary, a too small sampling area can lose events in which some muons would fall inside the TPC, artificially decreasing the number of events, especially at low multiplicities. For this reason, the core of the shower was randomly scattered at ground level over an area covering 205×205 m^2 centered upon the nominal LCH beam crossing point corresponding to the ALICE experiment (see figure 6.2). The optimisation of the size of this sampling area was obtained with preliminary simulations. It was found that, when the core was located outside this area, only a very small number of events gave rise to muons crossing the TPC and these events were only of low multiplicity ($N_\mu < 4$). This sampling area contributes to minimize the number of generated events without creating any bias on the final results.

Two main methods were used to perform the simulations: simplified Monte Carlo (Section 6.2.2) and full Monte Carlo (Section 6.2.3).

In order to generate a shower it is important to define some initialization parameters. This is summarised in section 6.2.1.

6.2.1 CORSIKA initializations

Some of the most important parameters initialized in every CORSIKA run to simulate the showers are:

- primary particle identification;
- energy range of primary particles;

- slope of differential primary energy spectrum;
- range of zenith angle;
- range of azimuth angle;
- the observation level;
- Earth's magnetic field at the experiment location;

In our simulations we have chosen pure proton and pure iron as primary cosmic particles in order to have the lower and higher limits of mass compositions.

Primaries in a wide energy range were generated, starting from 10^{12} eV up to 10^{18} eV. Simulations were run for small energy intervals within the whole range in order to make more efficient the computing time, and in turn to cover the energy range of primary cosmic rays giving rise to muons that can be detected in ALICE.

The zenith angle range was limited to $0^\circ \leq \theta \leq 50^\circ$ while the azimuth angle range was taken in the whole interval $0^\circ \leq \phi \leq 360^\circ$.

For all generated showers the starting altitude in the atmosphere was set to 0 g/cm^2 mass overburden.

The ground surface was selected as the observation level of the generated showers, which is 479 m above the sea level for the CERN Point 2 surface location.

The first interaction point of hadronic primaries was defined with a random behaviour according to the appropriate mean free path.

We assumed the default atmospheric model adopted by CORSIKA, which is the U.S. standard atmosphere parameterized according to J. Linsley. The parameters of this model can be found in [117]. The atmosphere density dependence with the altitude was modelled by dividing the atmosphere in 5 layers (i.e. 0 - 4, 4 - 10, 10 - 40, 40 - 100 and $>$ 100 Km). The following expressions reflect the dependence of the atmosphere density (T) with the altitude (h), with parameters a_i, b_i and c_i.

$$T(h) = a_i + b_i \cdot e^{-h/c_i} \qquad i = 1,...,4. \tag{6.1}$$

$$T(h) = a_i - b_i \cdot -h/c_i \qquad i = 5. \tag{6.2}$$

In the lower four layers the density decreases exponentially with the altitude (Eq. 6.1), while the fifth layer is characterized by a linear decreasing of density

with the altitude (Eq. 6.2) until it finally vanishes. Based on the U.S. standard atmosphere, the parameter $a_5 = 0$ in Eq. 6.2.

The Earth's magnetic field was defined in correspondence to the geographical location of the CERN. In this case magnetic field horizontal component was set to $B_x = 22.1$ μTesla whereas vertical component was set to $B_z = 41.6$ μTesla. In CORSIKA, the component $B_y = 0$, by definition[8].

The number of simulated showers is a decisive parameter during the simulation process since it allows to fix the time in a direct equivalence to the experimental effective time. This allows an accurate comparison between measurements and simulations without any normalisation. The number of events for a given energy interval depends on the flux, the solid angle, the area where the shower central axis is sampled and the *measurement* time, as follows,

$$N_{ev}(E_1, E_2) = \Phi \times \Omega \times A \times T \tag{6.3}$$

In Eq. 6.3, the primary particle flux is given by Φ (m^2 s sr TeV)$^{-1}$, while Ω (sr) is the solid angle, A (m^2) is the sampling area and T (s) is the measurement time. The total (all-particle) flux Φ of primary particles was calculated according to the *poly-gonato* model [47] which is explained in section 2.2. Its value was estimated to be $\Phi(1\text{TeV}) = 0.225 \pm 0.005$ (m^2 s sr TeV)$^{-1}$. Thus, the energy dependence of the flux can be expressed as,

$$\Phi(E_1, E_2) = 0.225 \int_{E_1}^{E_2} \left[\frac{E(TeV)}{1(TeV)}\right]^{-\gamma} dE \tag{6.4}$$

The exponent γ is the spectral index, defining the slope of the differential primary energy spectrum. This value was set to $\gamma = 2.7$ for energies below the knee ($E_k = 3 \times 10^{15}$ eV) and $\gamma_k = 3.0$ for energies above the knee.

The QGSJET model was chosen to describe the high-energy hadronic interactions, as well as the cross sections derived from it. The differences in rapidity distribution between π^0 and $\pi^{\pm}$ were taken into account according to the LHC data. A realistic nuclear fragmentation depending on the transverse momenta was defined. The NKG formula [67] was enabled in order to calculate the electromagnetic subcascades analytically. The radius of the lateral NKG distribution was defined between 100 cm and 200 m, while the NKG longitudinal development is sampled in vertical steps of 20 g/cm^2. The values of low cutoff kinetic energies were chosen as $E_h = 1$ GeV, $E_{\pi^0} = 3$ MeV, $E_\mu =$

[8] The reference system of CORSIKA is different from the ALICE coordinate system.

1 GeV, E_γ = 3 MeV, E_{e^-} = 3 MeV, for hadrons (not including π^0), π^0, muons, photons and electrons respectively. The calculation of the muon multiple scattering angles followed the *Molière* theory for large steps and were treated as single Coulomb scattering events for small steps (see explanation in 2.3).

6.2.2 Simplified Monte Carlo procedure

Our simulations, mainly aimed to the study of the muon multiplicity distribution in ALICE, started with a simplified Monte Carlo procedure. This is a fast and flexible method of estimating important parameters and observables involved in the analysis before using a full simulation.

With the simplified Monte Carlo the muon transport through the rock above the ALICE hall is not explicitly modelled. Instead, to make the simulation faster, the trajectory of the muons arriving at the surface level were extrapolated as straight lines to the depth of ALICE. An energy cut value of $E_\mu = 16\ \mathrm{GeV}/\cos(\theta)$, where θ is the zenith angle of the muon, is imposed thus reflecting the effect of the rock. All muons passing this cut and crossing an area of 17 m^2, corresponding to the horizontal cross-sectional area of the TPC, with the centre located underground in correspondence with the centre of the TPC, are considered detected.

6.2.3 Full Monte Carlo procedure

The full simulation takes into account all possible interactions in matter surrounding the experiment. In each event, all muons crossing the ground level are extrapolated to the horizontal mid-plane of the ALICE apparatus and flagged if they hit an enlarged area of 36 m^2 centred upon the TPC with no restriction on the energy of the muons. Then, the position and momentum of all flagged muons, at ground level, are recorded and used as input to the AliRoot code [1]. This is the ALICE framework where the ALICE experimental hall and the environment above and around the apparatus as well as all the detectors are accurately described. Flagged muons are propagated through this environment with GEANT3 [126]. Details about the simulated environment surrounding ALICE were explained in Section 4.5.

7 Analysis of data and Monte Carlo simulations

7.1 Data sample

The periods of pauses in collider operations, when no beam circulates in the LHC, constitute the proper time to perform alignment and calibration tasks of the different detectors using cosmic rays. Specifically in the period 2010-2013, apart from the mentioned tasks, ALICE undertook a program of cosmic ray data taking with the objective of exploiting the detector potentialities in a an important area as astroparticle physics and then to contribute to cosmic ray physics.

About 22.6 million events with at least one reconstructed muon (single-track or matched) in the TPC were collected in ALICE in 30.8 days of effective total time. The trigger system to detect atmospheric muons was comprised by TOF, ACORDE and SPD, as explained in section 4.4. The effective time of cosmic data taking is summarised in Table 7.1, where the amount of days with magnetic field *on* and *off* in the central barrel is specified as well.

Year	Effective time (days)	Magnetic field *on* (days)	Magnetic field *off* (days)
2010	4.45	3.34	1.11
2011	13.71	12.94	0.77
2012	10.02	7.85	2.17
2013	2.63	2.60	0.03
TOTAL	30.81	26.73	4.08

Table 7.1: Effective time of data taking with *standard* cosmic triggers in the period 2010 to 2013. The time of runs with magnetic field *on* and *off* is separately shown.

In cosmic runs with magnetic field *on*, the field strength was always the maximum reachable in ALICE, corresponding to B = $\pm$0.5 Tesla.

The effective time was calculated run by run defining:

$$\text{Effective time} = \text{Time of data taking} \times \text{Detector live time} \times \text{Reconstruction efficiency} \tag{7.1}$$

where,

$$\text{Detector live time} = \frac{L2a}{L0b} \tag{7.2}$$

The time of data taking was the total time of a run from its start until its stop. The detector live time was evaluated from the ratio L2*a*/L0*b*, where L0*b* gives the number of times a given detector is fired while L2*a* gives the number of times the same trigger passes the CTP decision, the detector dead time and other vetoes, as explained in section 4.4.

The reconstruction efficiency, given by a number between 0 and 1, keeps into account those events recorded but not reconstructed by the ALICE offline framework.

The valid runs were required to satisfy, in every period of cosmic data taking, the following selection criteria:

- run duration larger than 10 minutes;
- runs marked as "good run" by the Data Acquisition (DAQ) system and suited for physics analysis;
- data acquired with a combination (logical OR) of at least two out of the three trigger conditions (ACORDE, SPD and TOF) depending on the run period;
- TPC as readout detector;

The analysis of this thesis was centered on the multi-muon events, which we defined as those events with more than four reconstructed muons in the TPC ($N_\mu > 4$). Finally, a sample of 7487 multi-muon events, was collected out of a total of 22.6 million events which were detected in 30.8 days (in terms of effective time).

7.2 Analysis of data and simulations

7.2.1 Experimental muon multiplicity distribution

The algorithms and track selection criteria described in section 5.1, used to identify and reconstruct the trajectories of atmospheric muons arriving at the ALICE experiment, made possible to study a vast sample of data collected between 2010 and 2013. The muon multiplicity distribution (MMD), based on the whole data sample (22.6 million events) and corrected for the trigger efficiency (explained in section 4.4), is shown in figure 7.1. To avoid reconstruction inaccuracies associated with the most inclined showers, the zenith angle of all events was restricted to the range $0° < \theta < 50°$.

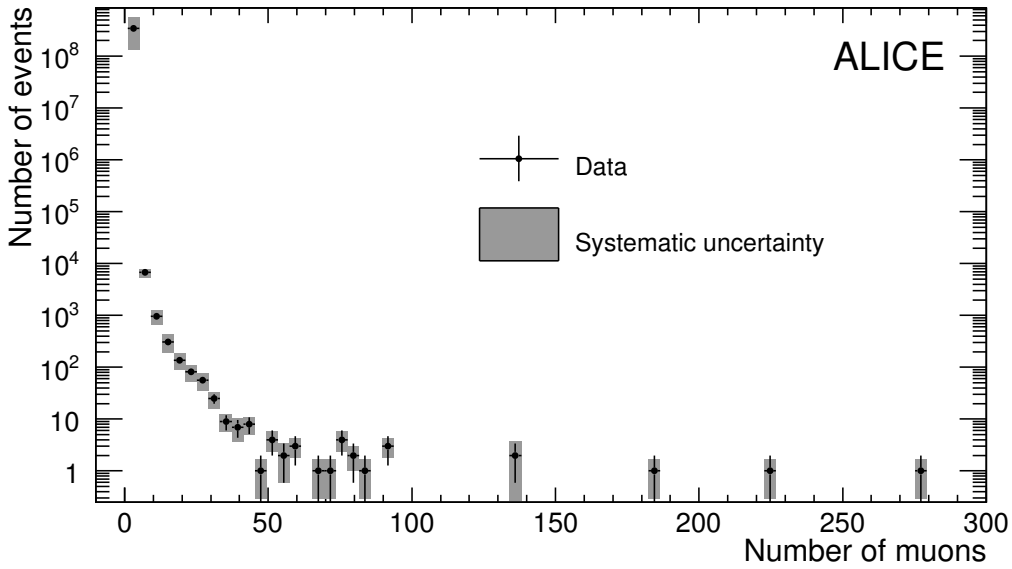

Figure 7.1: Muon multiplicity distribution of the whole sample of data (2010-2013) corresponding to 30.8 days of data taking.

According to the resolution on the number of reconstructed muons explained in section 5.2 (see figure 5.4) the bin width for this whole distribution was chosen equal to 4. With a qualitative analysis we note that the MMD shows a smooth trend up to a multiplicity of around 70, while it is noteworthy to pay attention to the existence of 5 events with more than 100 reconstructed muons. Similar distributions were found by ALEPH [101] and DELPHI [103], as described in section 3. Values of systematic and statistic uncertainties, are

separately plotted in the distribution for each multiplicity bin (Fig. 7.1). Details about the uncertainty estimations are further described in next sections.

The events with multiplicity higher than $N_\mu = 50$ were examined closely with the event-display interface to exclude the possibility of "interaction" events.

In the following section we give a detailed description of the main characteristics of the 5 high muon multiplicity (HMM) events, defined as events in which $N_\mu > 100$.

7.2.2 High muon multiplicity events

For illustration, the event-display picture of the 5 HMM events is shown in figure 7.2. The high degree of parallelism of this kind of events can be clearly seen in these figures. Three of them were detected in runs with magnetic field *on* and two runs with magnetic field *off*.

In the following we illustrate the main characteristics of each of the five HMM events.

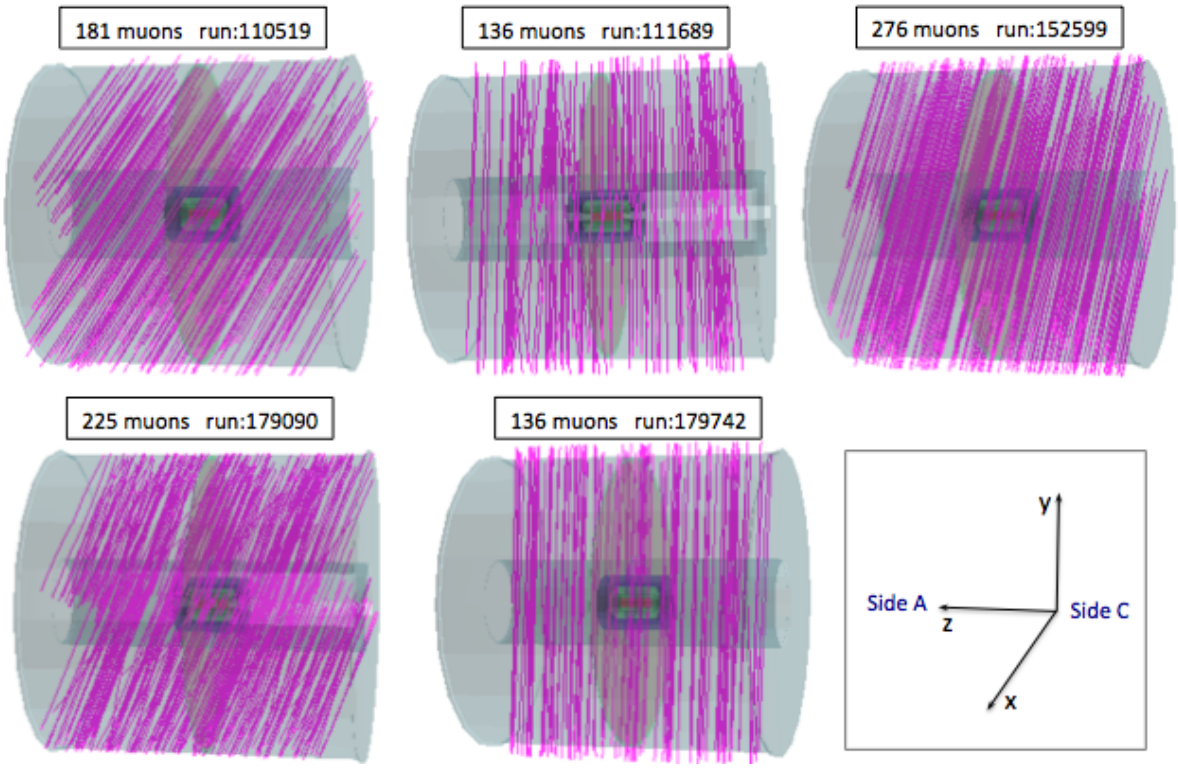

Figure 7.2: Visualisation of the 5 HMM events collected in ALICE, corresponding to a rate of 1.9×10^{-6} Hz.

Event 1 ($N_\mu = 181$)

The first HMM event was recorded by ALICE in February of 2010, corresponding to a multiplicity of 181 muons.

- Date: 2010-02-20
- Run: 110519
- Period: LHC10a
- Event: 6353
- Chunk: 10000110519022.20
- Magnetic field: - 0.5 T
- Trigger: SPD

The zenithal and azimuthal angular distributions of the muons of this event are shown in the first and second pads of the figure 7.3. This is the event with the most inclined shower, with a mean value of the zenithal angle equal to 40.5°. The mean value of the azimuthal angle is 212.4°. The spatial distribution of matched and single-track muons at the TPC mid plane is shown in the third pad of the same figure. The points corresponding to matched-track muons are represented with blue full circles, while those representing the single tracks are shown in red triangles. The majority of single-track muons are reconstructed near the ends of the TPC where muons may enter and leave the active volume without producing a track either the upper or lower halves of the detector.

Event 2 ($N_\mu = 136$)

The second HMM event corresponds to a multiplicity of 136 muons.

- Date: 2010-03-01
- Run: 111689
- Period: LHC10a
- Event: 9328

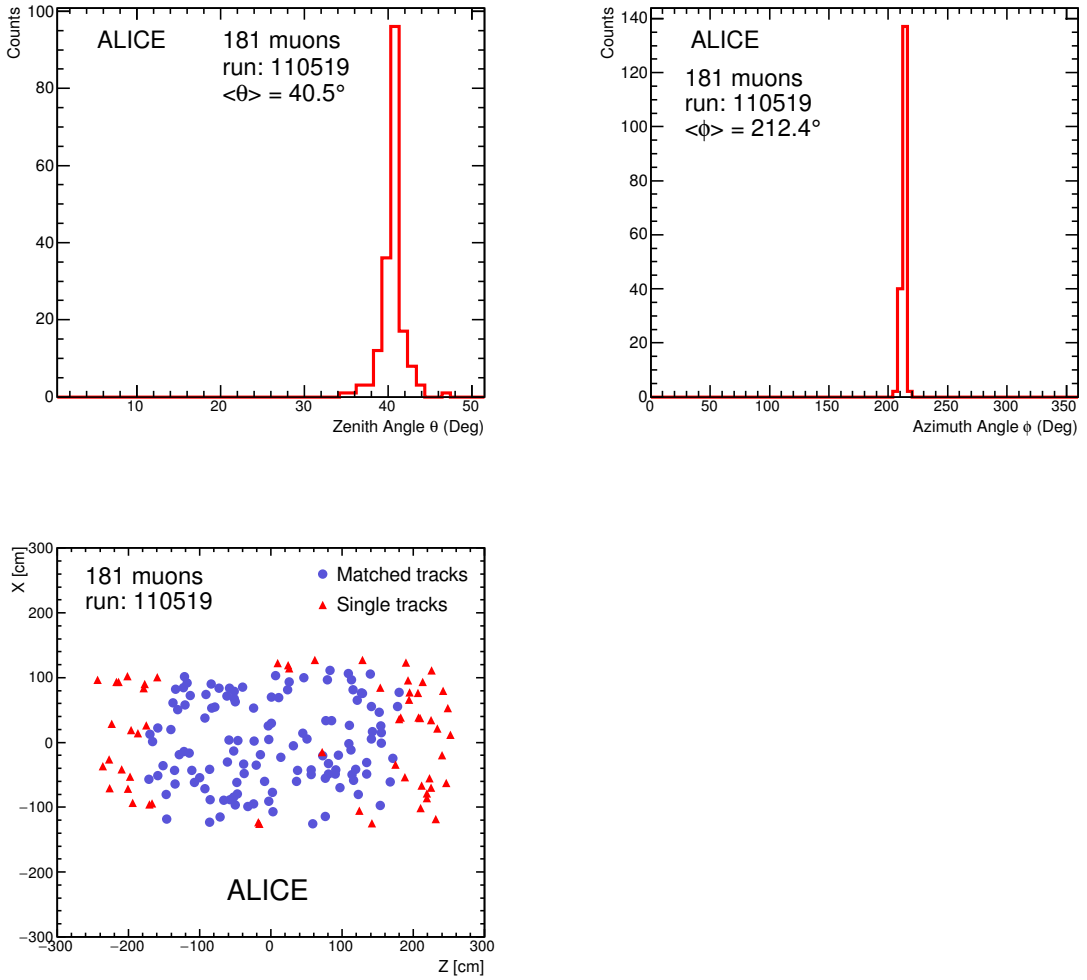

Figure 7.3: Event with 181 muons recorded in 2010 by ALICE. (1) Zenithal distribution, (2) azimuthal distribution and (3) spatial (XZ) distribution.

- Chunk: 10000111689030.10
- Magnetic field: 0
- Trigger: TOF

This event was recorded in a run without magnetic field. The mean zenithal and azimuthal angles equal to 16.7° and 170.6° respectively, are derived from the distributions shown in figure 7.4. The spatial distribution denotes that most of muons are matched-track muons.

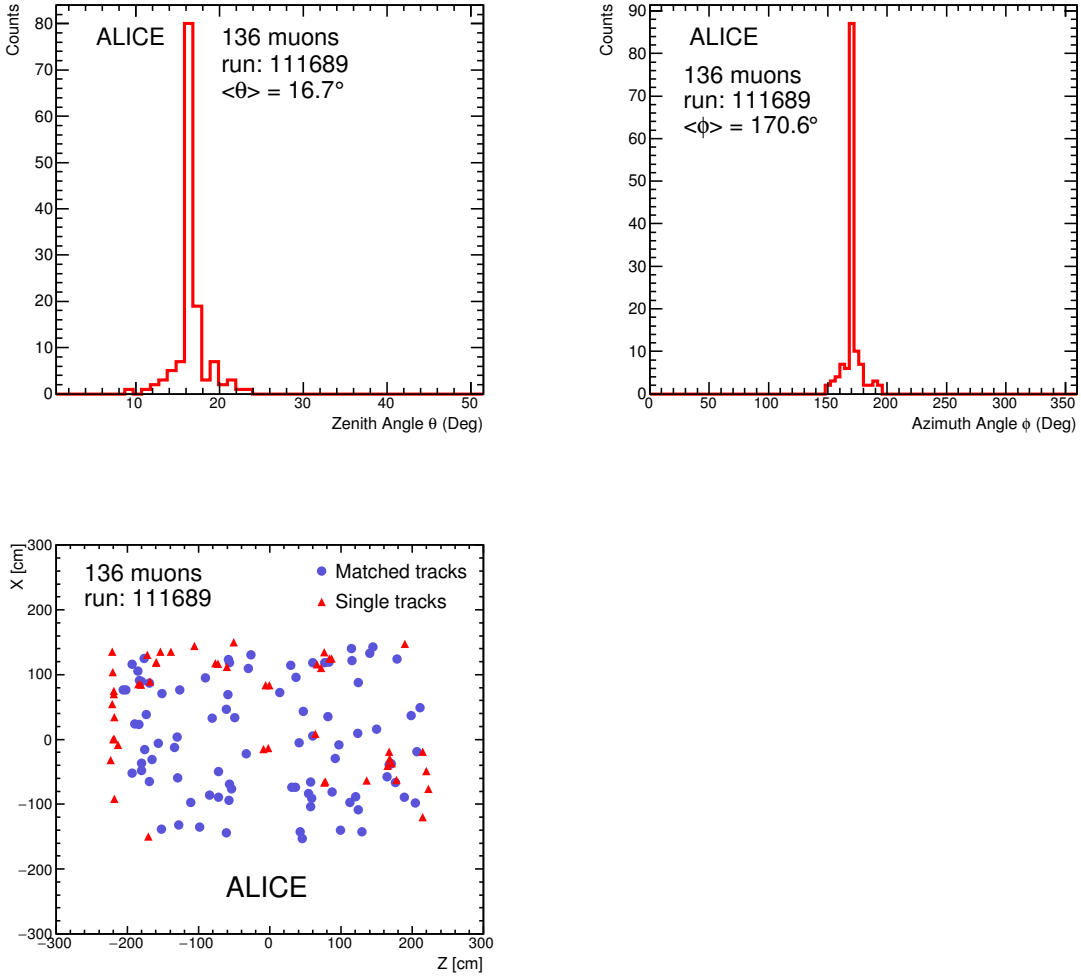

Figure 7.4: Event with 136 muons recorded in 2010 by ALICE. (1) Zenithal distribution, (2) azimuthal distribution and (3) spatial (XZ) distribution.

Event 3 ($N_\mu = 276$)

The third HMM event corresponds to a multiplicity of 276 muons.

- Date: 2011-05-26
- Run: 152599
- Period: LHC11c
- Event: 372
- Chunk: 11000152599020.12

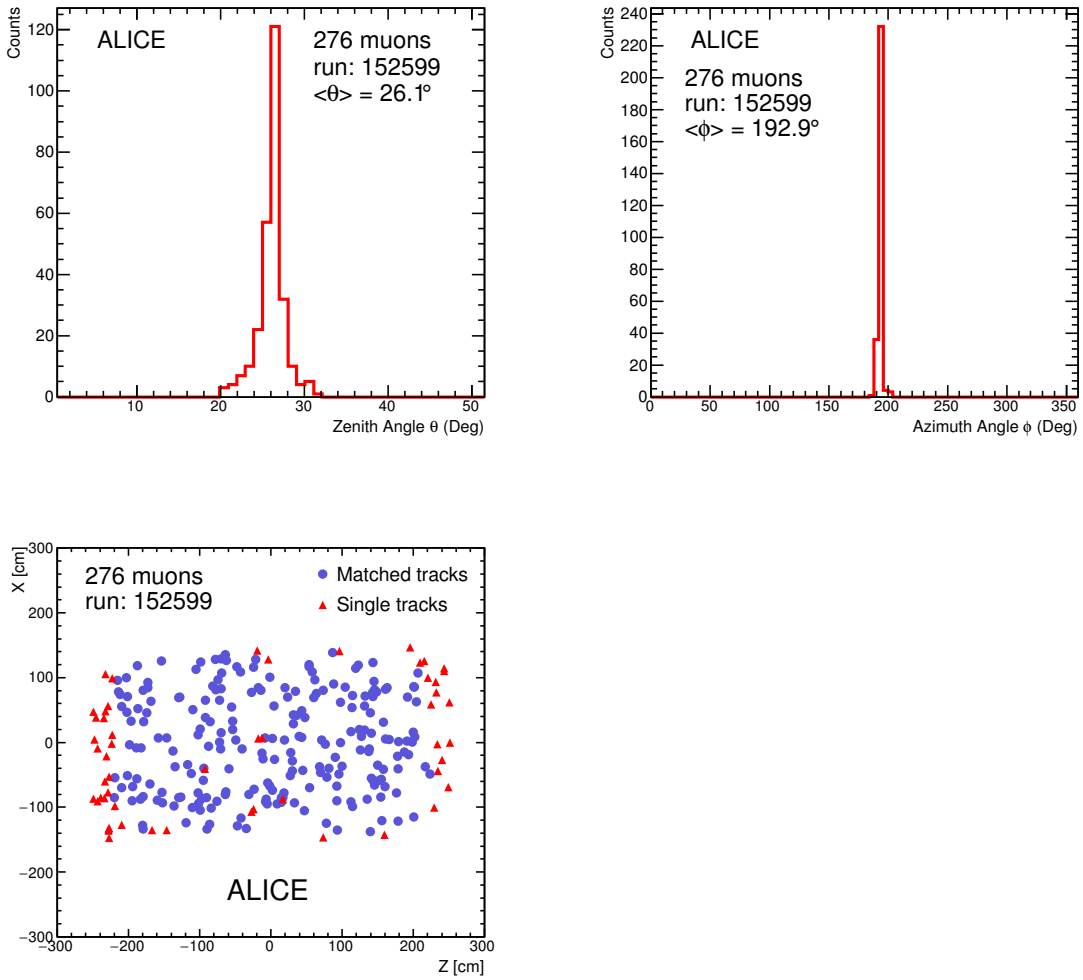

Figure 7.5: Event with 276 muons recorded in 2011 by ALICE. (1) Zenithal distribution, (2) azimuthal distribution and (3) spatial (XZ) distribution.

- Magnetic field: - 0.5 T
- Trigger: ACORDE

This is the highest multiplicity event, among the 5 HMM events detected in ALICE, with mean zenithal and azimuthal angles equal to 26.1° and 192.9°, respectively. The angular and spatial distributions are shown in figure 7.5. The distribution of single-track muons which were concentrated at the extreme values of the z axis, is well defined in this event taken with magnetic field and triggered by the detector ACORDE in 2-fold coincidence configuration.

Event 4 ($N_\mu = 225$)

The forth HMM event corresponds to a multiplicity of 225 muons.

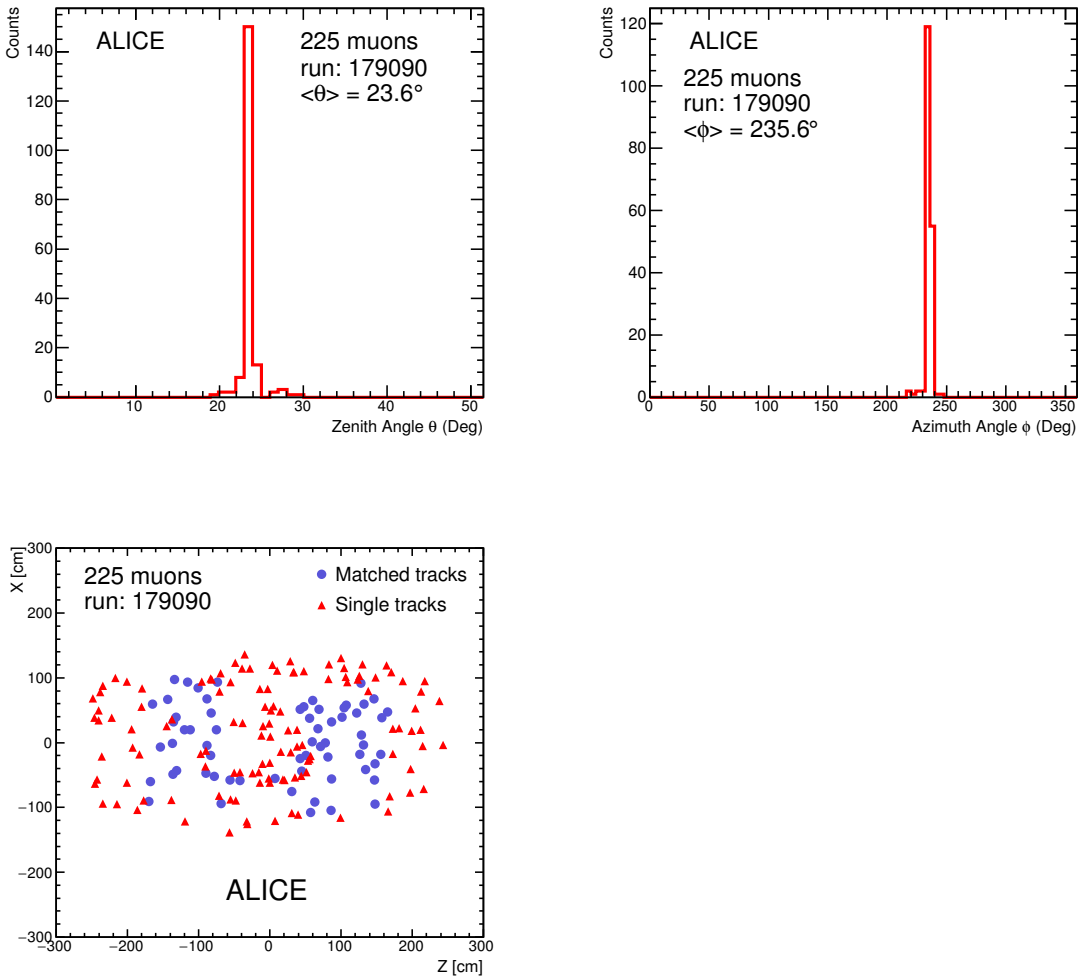

Figure 7.6: Event with 225 muons recorded in 2012 by ALICE. (1) Zenithal distribution, (2) azimuthal distribution and (3) spatial (XZ) distribution.

- Date: 2012-04-27
- Run: 179090
- Period: LHC12b
- Event: 2056
- Chunk: 12000179090061.17

- Magnetic field: 0
- Trigger: TOF

The zenith and azimuth angular distributions of this events are shown figures 7.6, showing mean zenithal and azimuthal angles equal to 23.6° and 235.6°, respectively.

An anomalous behaviour of this event was noticed during the offline analyses. This event was collected during a run with magnetic field *off*. The anomalous behaviour is reflected in the third pad of figure 7.6 in which red triangles (single-track muons) are accumulated in the central region of the spatial distribution of the muons (-70 cm $< z <$ 70 cm). Since the topology of this event, characterized by quite parallel muon tracks, is typical of the muonic component of EAS, it was necessary to investigate the cause of this anomaly. It was found that it is is due to an incorrect TPC drift velocity calibration, that was manifested as a Δz gap between the two drift volumes (A and C sides) from the TPC central HV electrode (CE). The central HV electrode is a plane perpendicular to the z-axis. The initial number of reconstructed atmospheric muons of this HMM event was $N_\mu = 288$ because the mismatching leaded to consider the tracks of every particle passing through the CE as two independent tracks separated by $d_{xz} > 3$ cm. Specifically for this event, the reconstruction algorithm was applied in such a way that different tolerance values of d_{xz} were tested in order to achieve the matching of the atmospheric muons that traversed the TPC in the region $z < [-70, 70]$ cm. Finally, this miscalibrated effect was corrected with an increased track mean distance d_{xz} = 12 cm, which allowed to match the central "single" tracks with minimal effect upon the already matched tracks in the region $|z| > 70$ cm. Thus, the final multiplicity value of this event became 225 muons.

Event 5 ($N_\mu = 136$)

The fifth HMM event corresponds to a multiplicity of 136 muons.

- Date: 2012-05-04
- Run: 179742
- Period: LCH12c
- Event: 67

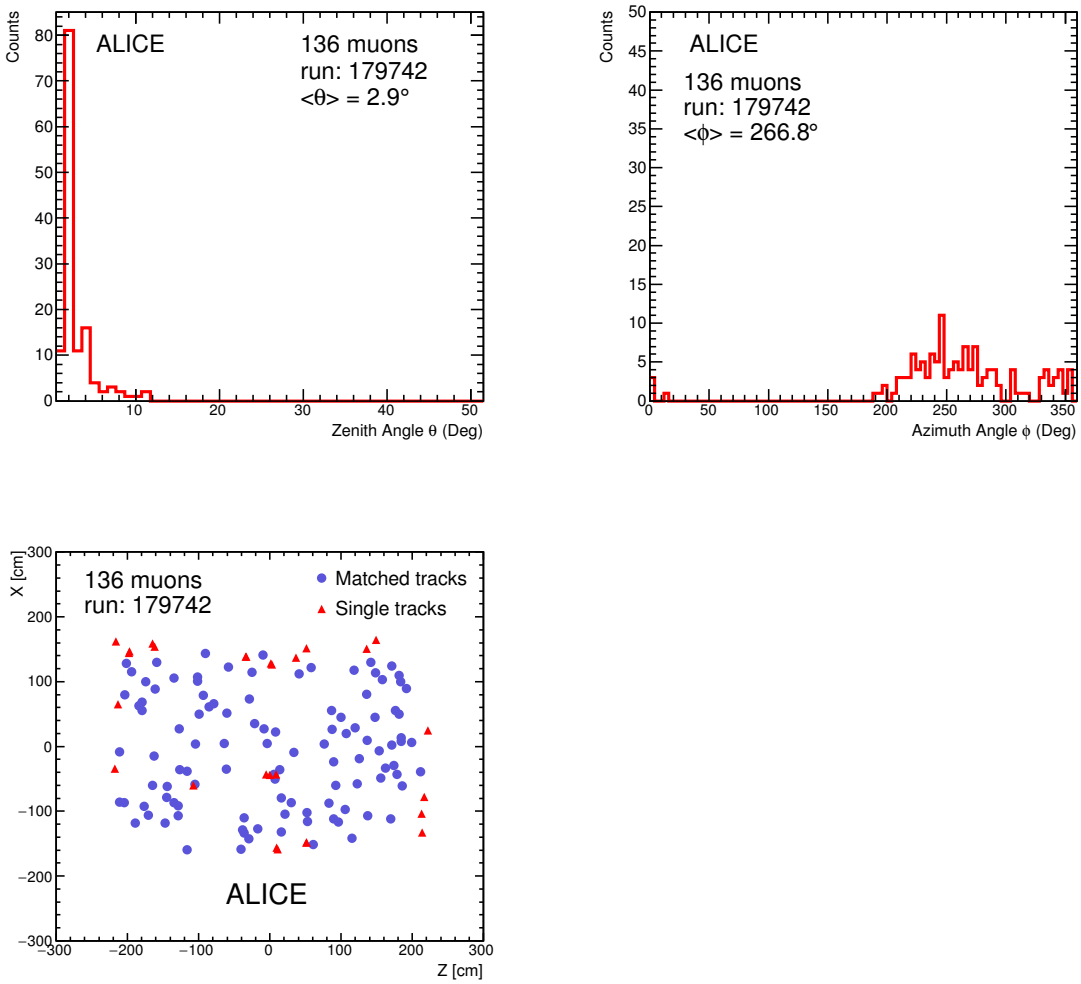

Figure 7.7: Event with 136 muons recorded in 2012 by ALICE. (1) Zenithal distribution, (2) azimuthal distribution and (3) spatial (XZ) distribution.

- Chunk: 120000179742036.12
- Magnetic field: 0.5 T
- Trigger: TOF

This is the most vertical event, characterised by a very small zenithal angle, whose mean value is equal to 2.9°. The spread distribution of the azimuthal angle, shown in figure 7.7 can be explained by the notable verticality of this event. The spatial distribution is also shown in this figure, showing that the single-track muons are mainly distributed at the edges of the TPC mid plane.

The number of muons for each of the 5 HMM events is shown in table 7.2 along with the corresponding run number, trigger and magnetic field, while the mean values of the zenith and azimuth angular distributions are in the next two columns. The areal density is shown in the last column, assuming that the horizontal cross-sectional area of the TPC is 17 m^2, given $z(\mathrm{m})=[-2.5, 2.5]$ and $x(\mathrm{m})=[-1.7, 1.7]$ and keeping into account the direction of the shower.

Number of muons	Run	Trigger	B (T)	$<\theta>$ (degrees)	$<\phi>$ (degrees)	Areal density (m^{-2})
181	110519	SPD	-0.5	40.5	212.4	14.0
136	111689	TOF	0	16.7	170.9	8.4
276	152599	ACORDE	-0.5	26.1	192.9	18.1
225	179090	TOF	0	23.6	235.6	14.4
136	179742	TOF	0.5	2.9	266.8	8.0

Table 7.2: The main characteristics of the 5 HMM events found in 30.8 days of data taking in the ALICE detector.

The highest multiplicity event reconstructed in the TPC was found to contain 276 muons, which corresponds to a muon areal density of 18.1 m^{-2}. The 5 HMM events occurred with a frequency of 1.9×10^{-6} Hz.

Study of the TPC fiducial area

Most of muons are inside a fiducial area A = 17 m^2, given by the limits -1.7 m $< x <$ 1.7 m and -2.5 m $< z <$ 2.5 m in the middle plane of the TPC. This is shown in figure 7.8 in which the spatial xz distribution of the muons in the TPC mid plane is given. In addition, we must take into account that the areal density has an implied associated uncertainty related to the TPC effective area. In order to report an accurate value of the event density with its uncertainty, a TPC fiducial area value was estimated with its error.

Considering that the maximum accepted distance between every pair of tracks (*up* and *down*) in the horizontal mid plane of the TPC is 3 cm, we might estimate the uncertainty of the axis coordinates (x,z) as 6 cm. Given this conservative error value, the estimated fiducial area of the TPC due to its horizontal cylindrical geometry results 17 ± 0.5 m^2. In turn, the error on the number of reconstructed muons, counting both matched and single-track muons, was estimated as being around 5% for $N_\mu > 100$. By knowing the uncertainties

on the estimated fiducial area of the TPC horizontal mid-plane and the error on the number of reconstructed muons, we have HMM events with a muon areal density $\rho_\mu > 5.9 \pm 0.4$ m^{-2}. The relative statistical uncertainty of the 5 observed HMM events is $\sqrt{5}/5 = 45\%$, giving a rate $(1.9 \pm 0.9) \times 10^{-6}$ Hz at the underground location of ALICE.

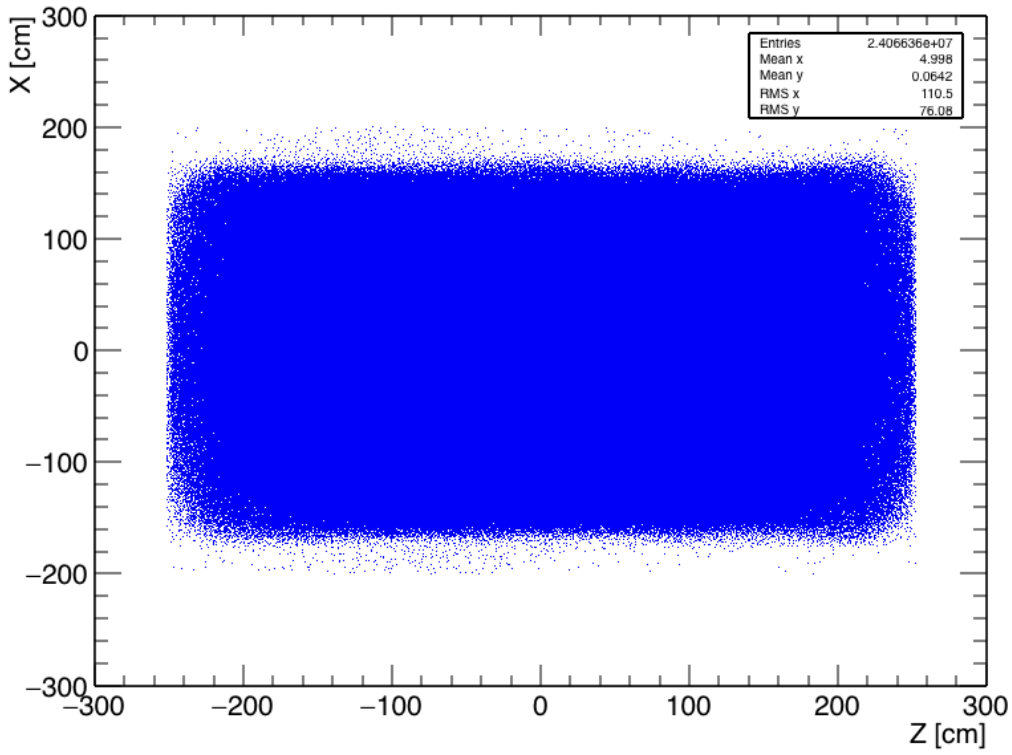

Figure 7.8: Spatial distribution of reconstructed matched and single-track muons in the TPC mid-plane. A representative sample of data was reconstructed, representing a few million of muons.

7.2.3 Simulated muon multiplicity distribution and comparison with data

The following analysis was addressed to interpret the complete measured distribution, and in particular to understand the origin of the HMM events. The comparison between measured and simulated data represents the basis to estimate the composition of the primary cosmic rays giving rise to muons in a wide range of multiplicity, and to understand whether the HMM events can be

described with standard hadronic models or whether they have to be explained with different production mechanisms.

Low-intermediate multiplicity

As a first step we tried to reproduce with MC simulation the MMD in the low-intermediate multiplicity region.

At this purpose we followed the Monte Carlo simulation strategy previously described in broad terms in chapter 6, to obtain the expected distribution. For this first step was used CORSIKA 6.990 with QGSJET II-03 model as hadronic interaction model, and a pure proton and pure iron (^{56}Fe) samples. The proton sample provides a lower limit on the number of events for a given multiplicity, while the iron sample provides an upper limit.

The main interest of this research was the multi-muon events ($N_\mu > 4$). Nevertheless, it is important to assure the understanding of the complete sample of recorded data, including the low multiplicities. For this purpose, the simplified Monte Carlo procedure (see description in section 6.2.2) was followed in order to generate primary cosmic rays with the two mentioned compositions, with energies $E > 10^{12}$ eV.

This preliminary assessment with the simplified Monte Carlo simulation produced the following results:

- The single muon events are mostly produced by primary energies in the range $10^{12} < E < 10^{13}$ eV.
- Primary cosmic rays of either composition, pure proton or pure iron, in the energy range $10^{12} < E < 10^{14}$ eV produce events with a multiplicity range from $1 \leq N_\mu \leq 4$.

After these preliminary results, since our purpose is to study multi-muon events, it was decided to simulate only events with primary energies $E > 10^{14}$ eV, following both, simplified and full Monte Carlo procedures described in the sections 6.2.2 and 6.2.3. All the events studied with the simplified MC method, were subsequently considered for a complete analysis using the full simulation which takes into account all possible interactions in the matter surrounding ALICE and the response of each detector.

Samples of proton and iron primary cosmic rays, were generated in the range of energy $10^{14} < E < 10^{18}$ eV. In this range the composition of primary

particles is a mixture of many species of nuclei in a ratio not well-known and which varies with energy. Therefore, the analysis with a pure proton sample represents the light composition and a pure iron sample represents a composition dominated by heavy nuclei. The zenith angle of generated showers was restricted to $0^\circ < \theta < 50^\circ$. The typical power law energy spectrum, $E^{-\gamma}$, was simulated with the spectral index $\gamma = 2.7 \pm 0.03$ for energies below the knee ($E_k = 3 \times 10^{15}$ eV) and $\gamma_k = 3.0 \pm 0.03$ for energies above the knee. The total (all-particle) flux Φ of primary particles was calculated according to the *polygonato* model [47] as explained in section 6.2.1. The primary particles were generated with the appropriate flux in the following energy intervals:

$10^{14} < E < 10^{15}$ eV, $10^{15} < E < 3 \times 10^{15}$ eV, $3 \times 10^{15} < E < 10^{16}$ eV,
$10^{16} < E < 3 \times 10^{16}$ eV, $3 \times 10^{16} < E < 10^{17}$ eV, $10^{17} < E < 3 \times 10^{17}$ eV,
$3 \times 10^{17} < E < 10^{18}$ eV.

The simulation in separate energy intervals is very convenient to populate every energy bin with the proper number of events. This procedure saves computing time by preventing a usually large and unnecessary amount of events in the first range of energy while populates the larger energy bins accordingly. The generated events were used four times (oversample = 4) only in the first energy interval while in the other intervals the events were used only once.

For the purpose of a straightforward comparison of the MMD data with the Monte Carlo expectation, the events were simulated corresponding to a time equivalent to 30.8 days. Thus, there is not need to apply arbitrary normalisation factors. In figure 7.9 the MMD simulated with both, proton and iron primaries, was compared with the MMD obtained with the data. For easy of comparison, the values of the simulated distributions were fitted with power-law functions to obtain the trend of the multiplicity for proton and iron sample.

From this figure we find that at lower multiplicities, $N_\mu < 20$, corresponding to lower primary energies, the data approach the proton curve, which represents a light ion composition of the primary cosmic ray flux, while at higher multiplicity ($20 < N_\mu < 30$) data lie closer to the iron curve, representing a heavier composition. This trend suggests that the average mass of the primaries become heavier with the increasing energy, a result consistent with several previous experiments [5, 40, 93]. At higher multiplicity ($N_\mu > 30$), the low statistics (less than 10 events per point) does not allow any conclusion on

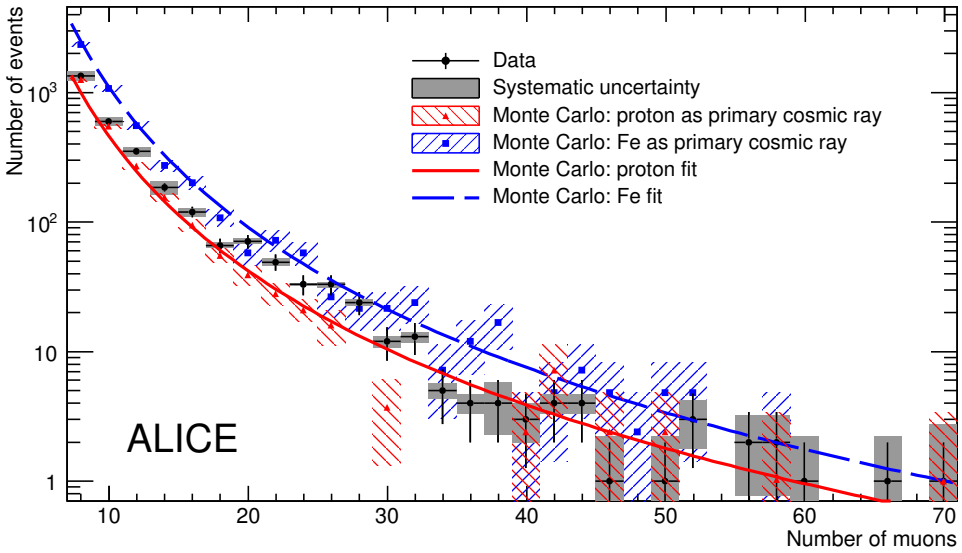

Figure 7.9: Muon multiplicity distribution of the data compared with the values and fit obtained from CORSIKA simulations with proton and iron primary cosmic rays for 30.8 days of effective time.

the trend of the composition, although the experimental points, considering their errors, are inside the region limited by proton and iron curves.

The errors in figure 7.9 are shown separately (statistical and systematic) for data, while for Monte Carlo the statistical and systematic uncertainties are summed in quadrature.

Systematic errors in the data

Values for the systematic uncertainty in the number of events as a function of multiplicity have been estimated by varying the parameters of the track reconstruction and matching algorithms. This was studied for the MMD and for the rate of HMM events.

The main source of systematic uncertainties comes from the value of the distance d_{xz} between every pair of tracks (*up* and *down*), which was found to have a strong influence upon the final number of single and matched track muons. Its optimal value was selected to be large enough to maximise the matching efficiency in HMM events while keeping the background to a minimum, but this adds a non negligible uncertainty which increases towards higher multiplicities. The selection of the minimum number of space points

of each track, such that the detector acceptance could be maximised by counting the short tracks of valid atmospheric muons, introduces another systematic error to the MMD.

A specific run was taken to study how the MMD changes for different values of d_{xz} and values of the minimum number of TPC clusters for each track. In figures 7.10 and 7.11 is shown the MMD of this event, using $d_{xz} = 2,3,5$ cm and a number of clusters equal to 30 and 60.

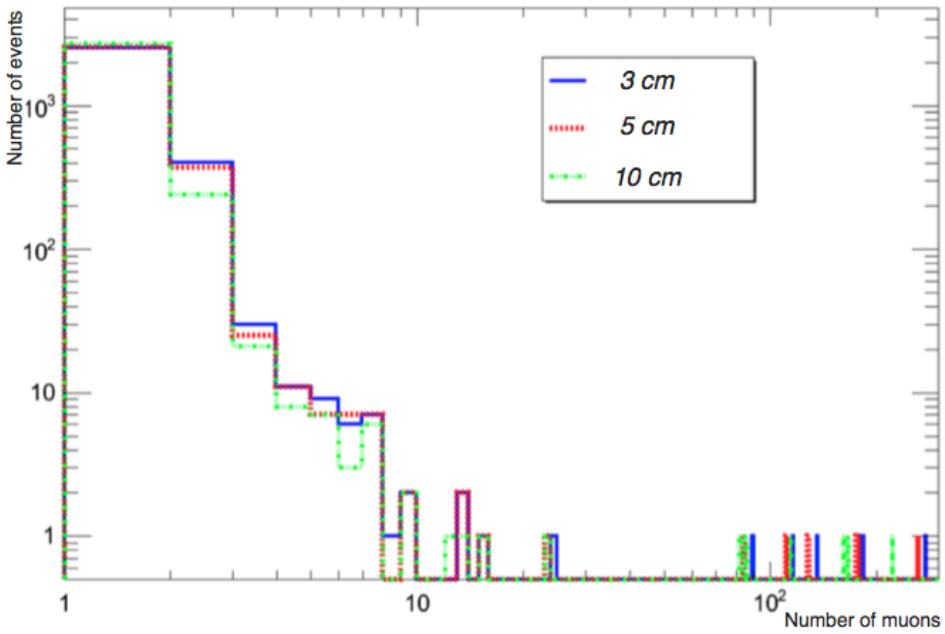

Figure 7.10: MMD of the run containing the event with 276 muons, using different values of d_{xz}.

With the two contributions, the systematic uncertainty of the MMD was estimated, as shown in figure 7.9.

Systematic errors in the simulations

The systematic errors of the MC simulation predictions are mostly given by the uncertainty carried by the estimation of the primary cosmic flux, the value used for the spectral index before and after the knee, the overburden rock description and the determination of data taking live time.

The total (all-particle) flux, $\Phi(1\text{TeV}) = 0.225 \pm 0.005$ $(\text{m}^2\ \text{s}\ \text{sr}\ \text{TeV})^{-1}$, used for normalisation, was estimated to have an error about 2.2% owing to the errors of individual elements [47]. This contributes to an estimated error of around 2% in our muon multiplicity distribution.

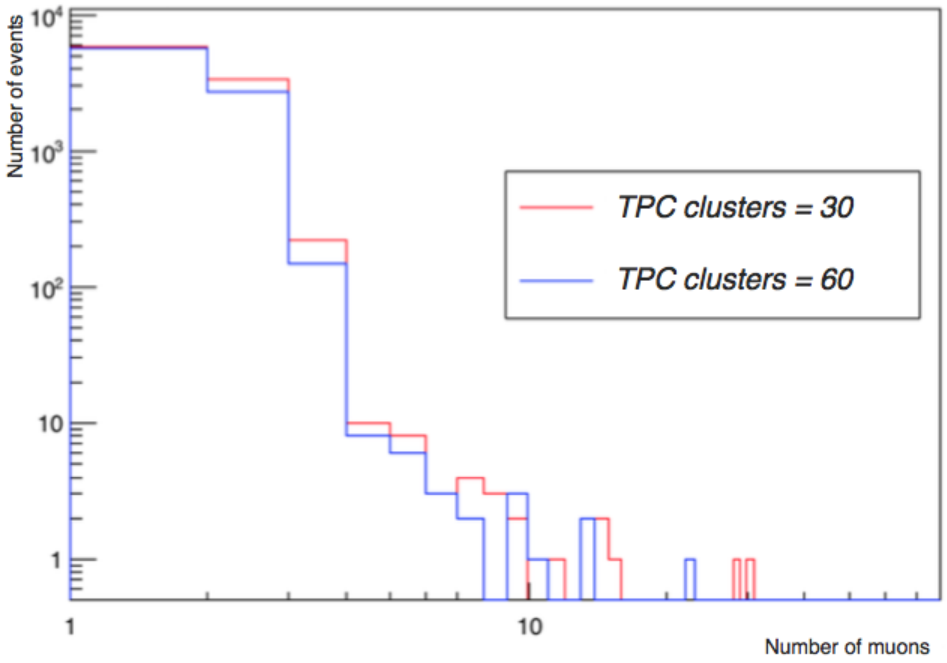

Figure 7.11: MMD of the run containing the event with 276 muons, using different values of the number of TPC clusters.

Since our normalisation at 1 TeV was extrapolated up to 10^{18} eV, we evaluated the uncertainties on the power law indexes used to simulate the cosmic spectrum. The uncertainty of the spectral index was estimated as $\sim 1\%$. The uncertainty in the spectral index below the knee ($\gamma = 2.7 \pm 0.03$) gives rise to an error of about 15% in the muon multiplicity distribution, while the error of spectral index above the knee ($\gamma = 3.0 \pm 0.03$) has a contribution of 2.5% to the systematic error of the MMD.

The passage of muons through the overburden rock results in energy loss and change of directions by multiple scattering. This implies that the muon flux, mainly at lower energies gets lessened when arriving at ALICE detector. Specifically the error of the rock description is reflected in the error on the threshold energy of the muons reaching the detector. This results in a systematic uncertainty of approximately 4% in the MMD.

The uncertainty on the live time of 30.8 days of data taking was evaluated as 2%, due to the error in the dead time estimation of the trigger detectors. This represents less than 2% of the uncertainty of the MMD.

The contribution on the systematic errors due to different values of the cuts in the matching algorithm, has been evaluated in the simulations with the same procedure used for the data and described in section 7.2.3.

7.2.4 Simulated high muon multiplicity events and comparison with data

The success of the whole procedure, based on the good qualitative trend of low and intermediate multiplicities (Fig. 7.9), leads to reinforce the idea of using the same simulation scenario to explain the HMM events, in particular the rate of them.

The 5 HMM events collected at the depth of ALICE, very well visible in the muon multiplicity distribution of figure 7.1 correspond to a rate of 1.9×10^{-6} Hz. The target of this thesis is to compare the rate of HMM events obtained in the simulations with the value found through the measurements, and then get some information on them like the energy and the primary elements producing these events.

The influence of the underground environment (e.g. rock above the experiment, access shafts) upon the detected high muon multiplicity events was checked by superimposing the location of the HMM events on the θ *vs* ϕ distribution of the arrival directions of muons previously shown in figure 5.9. This superposition is shown in figure 7.12. In turn the influence of the discrepancies between data and simulations, with regard to the modelling of the overall underground environment, upon the 5 HMM events, is shown in figure 7.13.

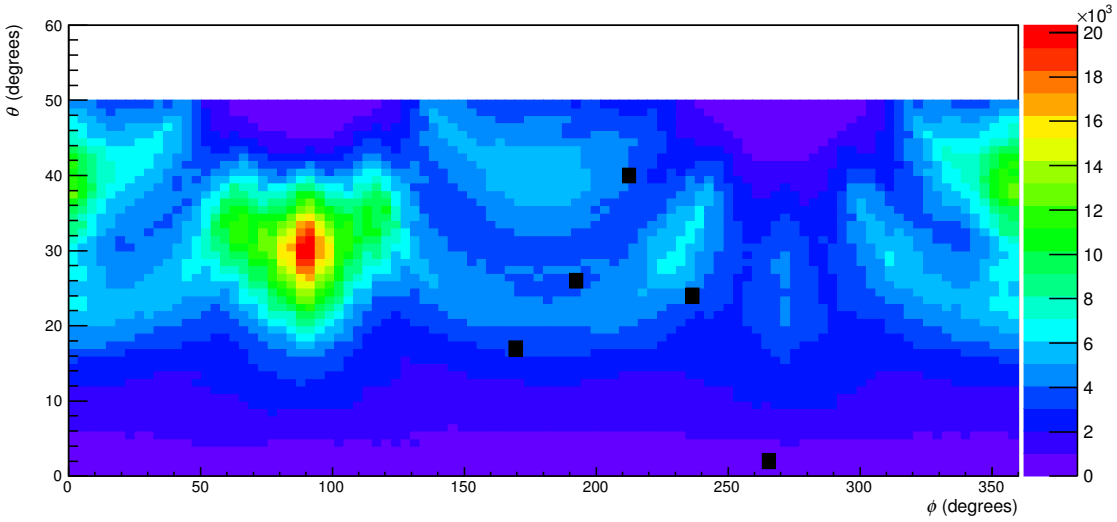

Figure 7.12: Zenith *vs* azimuth distribution of atmospheric muons in the horizontal mid plane of the ALICE TPC, obtained with the whole data sample. The five HMM events are imposed as black boxes.

From figures 7.12 and 7.13 it is clear that the directions of the 5 HMM

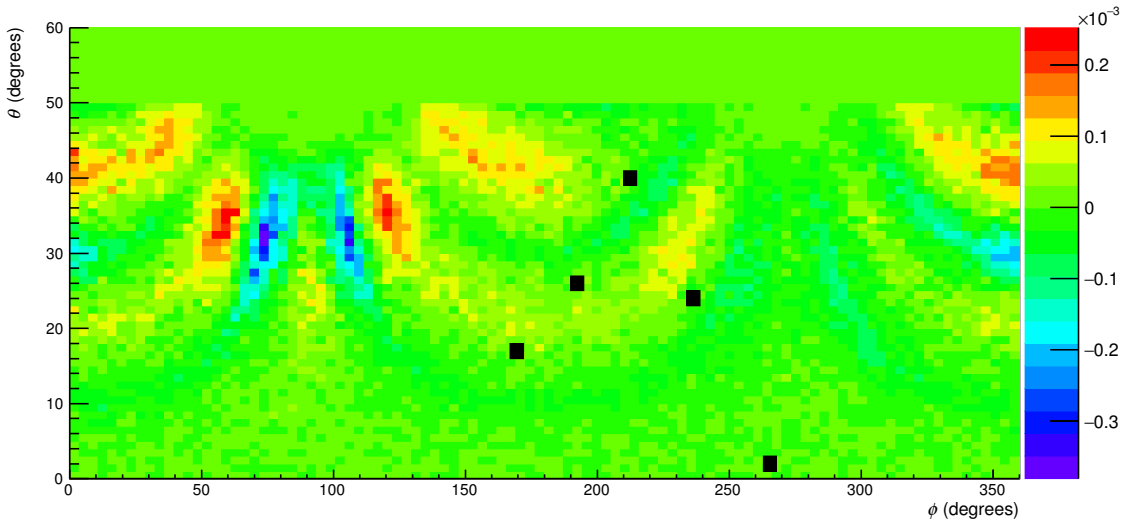

Figure 7.13: Difference between data and MC simulations in the zenith *vs* azimuth distribution of atmospheric muons in the horizontal mid plane of the ALICE TPC. The five HMM events are imposed as black boxes.

events do not coincide with the zones affected by the shafts and they are not affected by the MC modelling of the underground environment.

Simulation of HMM events

Given that the statistical uncertainty of the number of HMM events in the data is dominant, it becomes essential to simulate an increased time equivalent in the simulations in order to reduce the fluctuation of these "rare" events. Therefore we have simulated 365 days equivalent of data taking live time. The simulation was performed with both procedures: simplified and full Monte Carlo. Two versions of CORSIKA were used: CORSIKA 6.990 with QGSJET II-03 model and CORSIKA 7.350 with QGSJET II-04 model.

The simplified Monte Carlo demonstrated that only primary cosmic rays with energies $E > 10^{16}$ eV, contribute to events with $N_\mu > 100$. Thus, primaries in the energy interval $10^{16} < E < 10^{18}$ eV were generated and processed with the full simulation. As in the study of the MMD, pure proton and pure iron samples were simulated.

With simplified and full MC simulations, the number of HMM events expected in one year equivalent of data taking live time, were obtained and shown in table 7.3. The results correspond to the two mentioned versions of QGSJET as hadronic model for light and heavy compositions of primary

cosmic rays.

Model	Simple MC		Full MC	
	proton	iron	proton	iron
CORSIKA 6.990 (QGSJET II-03)	40	61	27	51
CORSIKA 7.350 (QGSJET II-04)	41	72	30	52

Table 7.3: Number of HMM events with the simplified and full MC simulations, for a period equivalent to 365 days of data taking. Events generated with two model versions: CORSIKA 6.990 (QGSJET II-03)and CORSIKA 7.350 (QGSJET II-04).

With the results shown in table 7.3 we can make some preliminary considerations. The EAS produced by high energy cosmic rays composed by iron contribute to more HMM events than the shower generated by primaries composed by proton, as expected. This occurs with both versions of QGSJET (II-03 and II-04). In addition, we note that the more recent version QGSJET II-04 gives rise to a slightly higher rate of HMM events than the previous model version. Moreover, the effect of the underground environment and the detector response is reflected in a suppression of the number of events with full MC simulations compared to the simplified MC procedure.

To reduce further the fluctuations in the rate of HMM events and have a better estimate of the statistical errors we performed four additional simulations, each of 365 days of live time with the same procedure used for the previous simulations. Due to the small number of HMM events we used the same generated samples produced for the first simulation but changing randomly the core of each shower over the usual surface area (205×205 m^2). Given that the acceptance of the TPC is about 3000 times smaller than this area, all the five samples are statistically independent. We proceeded reusing the same simulated sample corresponding to 365 days in four additional simulations, and then obtaining the mean value of the five simulations as well as its standard deviation.

A summary of the results obtained for all the five simulations is presented in table 7.4 for CORSIKA 6.990 with QGSJET II-03 and table 7.5 for CORSIKA 7.350 with QGSJET II-04. The first line represents the results from sample previously shown in table 7.3.

Comparison of the results demonstrates that the detailed modelling of the underground environment has about a 30% effect on the number of HMM events.

	Simple MC		Full MC	
Run	proton	iron	proton	iron
1	40	61	27	51
2	40	64	24	42
3	31	43	25	31
4	26	52	20	34
5	33	64	22	53

Table 7.4: Number of HMM events for each run obtained with both MC procedures, simplified and full simulation. Each run is equivalent to 365 days of data taking. The events have been generated using CORSIKA 6990 with QGSJET II-03.

	Simple MC		Full MC	
Run	proton	iron	proton	iron
1	41	72	30	52
2	42	88	32	71
3	48	78	29	62
4	46	84	35	61
5	36	83	31	58

Table 7.5: Number of HMM events for each run obtained with both MC procedures, simplified and full simulation. Each run is equivalent to 365 days of data taking. The events have been generated using CORSIKA 7350 with QGSJET II-04.

The average value of the number of HMM events expected in 365 days of data taking was obtained from the five independent simulations shown in tables 7.4 and 7.5.

The statistical uncertainty was determined from the standard deviation of the 5 mean values. The result given in table 7.6, is the mean value of the number of HMM events expected in one year of simulated events with its statistical error obtained with the full simulation.

There are two major contributions to the systematic uncertainty on the number of HMM events:

(a) The first comes from the muon reconstruction algorithm as explained in section 7.2.3. To estimate its contribution, we took the first simulated sample (first row in tables 7.4 and 7.5), corresponding to 365 days of data taking,

for each element (p, ^{56}Fe) and each CORSIKA version, and redetermined the number of HMM events using different tunes of the track selection criteria and matching algorithm.
(b) The second contribution stems from the uncertainties in the parameters used in the simulations, as discussed in 7.2.3. This contribution represents approximately 20% and, in summary, it takes into account the uncertainties from calculating the following parameters:

- flux of cosmic rays at 1 TeV
- the slopes the energy spectrum below and above the knee
- energy threshold of muons to reach the detector (description of the rock above the experiment)
- detector live time

The systematic uncertainty was estimated by the sum in quadrature of single contributions (Table 7.7).

Consequently, the total uncertainty was calculated as the sum in quadrature of the statistical error and the systematic one, as follows,

$$Uncertainty = \sqrt{\sigma^2_{stat} + \sigma^2_{sys}}, \tag{7.3}$$

where

$$\sigma^2_{sys} = \sigma^2_{sys\_rec} + \sigma^2_{sys\_sim} \tag{7.4}$$

The terms σ_{sys_rec} and σ_{sys_sim} are the contributions to the systematic uncertainty, due to the reconstruction algorithm and the simulation parameters respectively.

In table 7.7 the statistical and systematic contributions are separately shown, together with the total uncertainty calculated with the equation 7.3.

In the large sample used in simulations (365 days), the contribution of systematic uncertainties to the rate of HMM events is dominant over the statistical uncertainty.

As for the data, with 5 observed HMM events, the statistical uncertainty ($\sqrt{5}/5$) prevails and represents $\sim$45%, whilst the systematic uncertainty is 20%. The systematic error was determined with different tunes of the reconstruction algorithm as with the MC simulations, but using the observed

	CORSIKA 6.990 QGSJET II-03		CORSIKA 7.350 QGSJET II-03	
	proton	iron	proton	iron
$\langle N \rangle$	23.6	42.2	31.4	60.8
σ	1.3 (5.5%)	5.0 (12%)	1.1 (3.7%)	3.5 (5.7%)

Table 7.6: Mean value and statistical uncertainty of the number of HMM events, expected in 365 days live time, using full MC simulation.

HMM events. The sum in quadrature of the statistical and systematic uncertainties in the determination of the observed HMM events is $\sqrt{\sigma_{stat}^2 + \sigma_{sys}^2} = \sqrt{(45)^2 + (20)^2} = 49\%$.

	CORSIKA 6.990 QGSJET II-03		CORSIKA 7.350 QGSJET II-03	
	proton	iron	proton	iron
$\sigma_{stat}(\%)$	5.5	12	3.7	5.7
$\sigma_{sys}(\%)$	24	22	22	27
Uncertainty(%)	25	25	22	28

Table 7.7: Statistical and systematic uncertainties in the calculation of the number of HMM events, expected in 365 days live time, using full MC simulation. The final uncertainty was calculated from the sum in quadrature by the equation 7.3.

8 Discussion of results and Summary

The results of the comparison of the rate of observed HMM events with the expected rate obtained with full Monte Carlo simulations, are shown in table 8.1. The systematic uncertainties have been added in quadrature to the statistical uncertainty in this final comparison of the observed rate of HMM events with that obtained from the Monte Carlo simulations.

The simulation of the HMM event rate from primary cosmic rays composed by iron, using CORSIKA 7.350 and QGSJET II-04, reproduced better the HMM event rate observed during the cosmic data taking in ALICE. According to this result, 1 HMM event every 6.0 days is expected from a pure iron composition, compared with a frequency of 1 event every 6.2 days measured with data. The frequency of the same element, simulated with CORSIKA 6.990 and QGSJET II-03, is lower but still consistent with the observed rate. The simulation of pure proton composition with energy $E > 10^{16}$ eV, using both models (QGSJET II-03 and QGSJET II-04), produce HMM events in a rate which is almost the half of the rate from data.

Therefore the observed rate of HMM events in ALICE appear to favor a heavy component of the primary particles, however, given the large uncertainties in the measured rate, we can not come to a firm conclusion about the chemical elements producing these events.

HMM events	CORSIKA 6.990 QGSJET II-03		CORSIKA 7.350 QGSJET II-04		Data
	proton	iron	proton	iron	
Period [days per event]	15.5	8.6	11.6	6.0	6.2
Rate [$\times 10^{-6}$ Hz]	0.8	1.3	1.0	1.9	1.9
Uncertainty (%) (syst + stat)	25	25	22	28	49

Table 8.1: Comparison of the HMM event rate observed in ALICE with the expected value from detailed MC simulation.

Although, at these energies, the primary cosmic rays are unlikely composed

by the light elements, and our simulation favors a heavy composition to explain the rate of the data, the large uncertainties in the data do not allow to exclude a possible contribution on HMM events due to elements lighter that ^{56}Fe.

The different rates of HMM events, depending on the selected QGSJET model, reveal that the expected rate is sensitive to the hadronic production mechanisms in air shower development. The latest version of QGSJET differs from earlier versions in its treatment of forward neutral meson production, resulting in a higher muon yield and has been retuned taking into account early LHC results on hadron production in 7 TeV proton–proton collisions, as explained in detail in section 6.1.

Finally, using all the HMM events simulated with CORSIKA 7350 and QGSJET II-04, generated by pure iron and corresponding to 5 years of data, we have investigated the distribution of the core location at surface level of these events. The distribution of the distance between the core of each simulated EAS, producing HMM events, and the centre of ALICE is shown in figure 8.1.

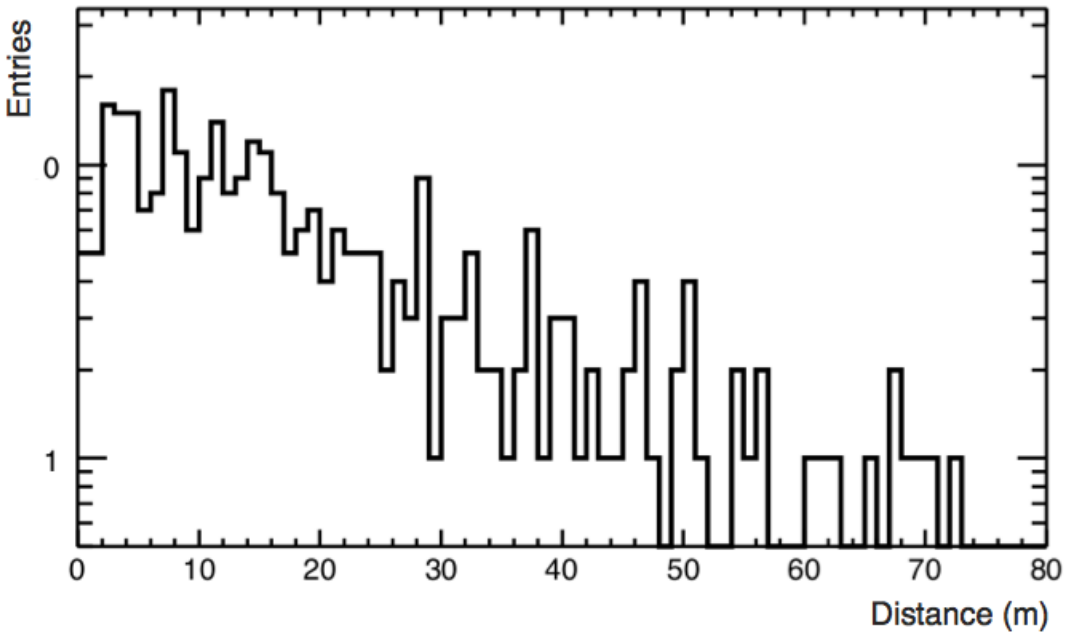

Figure 8.1: The distance between the core of the EAS producing HMM events and the centre of ALICE, for a period equivalent to five years of data taking with iron as primary cosmic rays.

The mean value and the RMS of the same distribution at four different energy ranges, is shown in Table 8.2. The average distance of the shower core

from the centre of ALICE, for all the events, is 19 m and the RMS value is 16 m. Primaries with an energy $E > 3 \times 10^{17}$ eV, corresponding to the highest energy interval studied in this analysis, produce larger showers that may give rise to HMM events also when the shower core falls farther from the center of ALICE. In this case, the mean of the shower core distribution from ALICE is 37.3 m whereas the RMS value is 17.6 m.

Primary Energy (eV)	Mean (m)	RMS (m)
$10^{16} < E < 3 \cdot 10^{16}$	3	1.9
$3 \cdot 10^{16} < E < 10^{17}$	9.2	4.8
$10^{17} < E < 3 \cdot 10^{17}$	21.3	11.2
$3 \cdot 10^{17} < E < 10^{18}$	37.3	17.6
$10^{16} < E < 10^{18}$	19.2	16

Table 8.2: Distance between simulated EAS cores and the centre of the ALICE experiment

Another illustrative representation of the spatial core distribution is shown in figure 8.2, where the colour of each point indicates the energy associated with the primary cosmic ray. In this way one may have a visual representation of the correlation between the distance of the core from the centre of ALICE and the energy of the associated primary cosmic ray. We note that the cores fall within an area of approximately 140×140 m^2 centred upon ALICE, which is located at the origin in figure 8.2. We note also that the lower energies have a core located closer to ALICE, as we can understand considering that primary of lower energy can produce an HMM events only if the core is located close to ALICE.

Summary

The feasibility of the ALICE detector to collect the muonic component of EAS produced by primary cosmic rays with energies $E_\mu > 10^{14}$ eV, was demonstrated by registering millions of events covering 30.8 days of effective time in the period 2010-2013.

The muon multiplicity distribution was measured in ALICE, including events with very high multiplicity, events also found by ALEPH and DELPHI experiments but without a proper explanation.

In this thesis a satisfactory method to study the events produced in atmospheric showers, was stablished, as well as an efficient simulation machinery

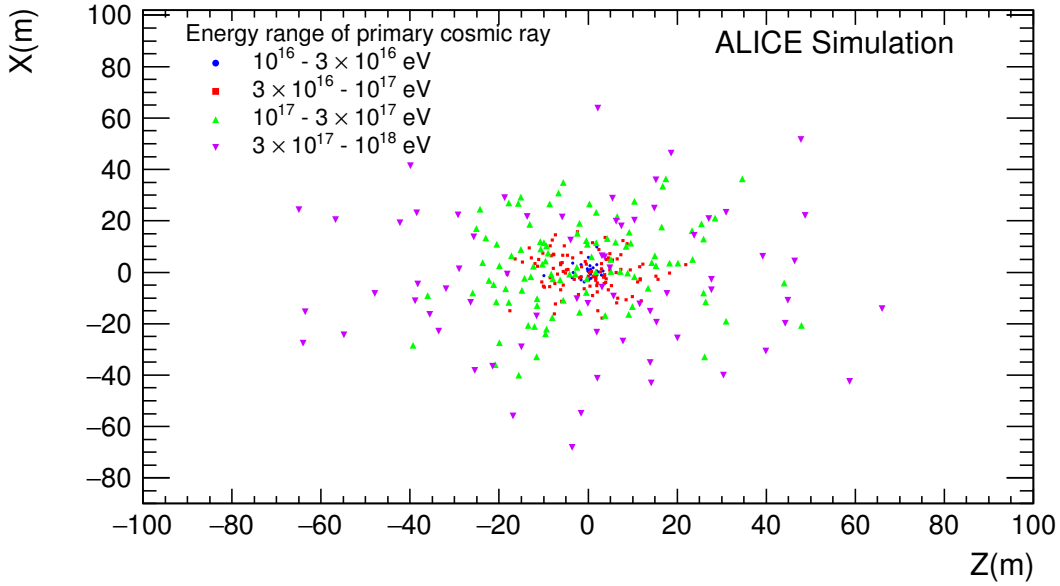

Figure 8.2: The spatial distribution of the cores of simulated EAS giving rise to more than 100 muons in the ALICE Time Projection Chamber. The simulation was for iron primaries in the energy range 10^{16} - 10^{18} eV and corresponds to the equivalent of 5 years of data taking .

allowing to produce the results to be compared with the observed data. This procedure put together important tools like CORSIKA to describe the EAS, a framework like GEANT3 to transport muons through the ALICE environment and its overburden, the AliRoot tool to simulate the detector response, and new programatic tools to accomplish the reconstruction of the complete muon trajectory in the TPC in a framework which was originally designed to reconstruct events with different track topology.

With all these tools, the MMD was satisfactorily explained in the range of low – intermediate multiplicities, using simulated cosmic showers produced by light component (proton) and heavy component (iron).

Conventional hadronic mechanisms with differences in their formulations were used to describe the hadronic interactions during the EAS evolution. The first step of our analysis concluded that primary cosmic rays have a mixed composition with an average mass that increases with energy. This is in agreement with most of the experiments working in the energy range of the knee. The reliability of cosmic data taken, at the relative shallow depth of ALICE, and its interpretation through standard hadronic models was so verified allowing us to face the study of HMM events.

As a second step, our analysis stated that only events produced by primary elements with energies above 10^{16} eV give rise to HMM events ($N_\mu > 100$). Then, a large amount of simulated data, corresponding to one year of live time were generated both with proton and iron primaries, to reduce the fluctuations in the rate of HMM events, in the energy range $10^{16} < E < 10^{18}$ eV.

The last step was the study of the observed rate of the HMM events. We concluded that this rate (5 events in 30.8 days) is well described by the predicted rate from Monte Carlo simulations using CORSIKA 7.350 and QGSJET II-04, by assuming a heavy composition at energies $E > 10^{16}$ eV.

The limited period of data taking (30.8 days) and the very low rate of HMM events, give rise to a large uncertainty in the measured rate of these events (almost 50%), preventing us from strong conclusions about the elements producing these events, although heavy nuclei are the most probable. Therefore, an explanation of the rate of HMM events, using a reasonable heavy composition and a description of the EAS given by conventional hadronic mechanisms, is for the first time compatible with the observed data.

Our results seem to be compatible with a knee of the energy spectrum due to the light composition followed by a spectral steepening of the other elements depending on their atomic number Z.

Bibliography

[1] **ALICE** Collaboration, K. Aamodt *et al.*, "The ALICE experiment at the CERN LHC," *JINST* **3** no. 8, (2008) S08002.

[2] Y. Akiba *et al.*, "The Hot QCD White Paper: Exploring the Phases of QCD at RHIC and the LHC," (2015) , arXiv:1502.02730 [nucl-ex].

[3] J. Alme *et al.*, "The ALICE TPC, a large 3-dimensional tracking device with fast readout for ultra-high multiplicity events," *Nucl. Instrum. Meth. A* **622** (2010) 316–367, arXiv:1001.1950 [physics.ins-det].

[4] M. Aglietta *et al.*, "The EAS size spectrum and the cosmic ray energy spectrum in the region 10^{15}-10^{16} eV," *Astropart. Phys.* **10** no. 1, (1999) 1–9.

[5] M. A. K. Glasmacher *et al.*, "The cosmic ray composition between 10^{14} and 10^{16} eV," *Astropart. Phys.* **12** no. 1, (1999) 1–17.

[6] T. Antoni *et al.*, "Electron, muon, and hadron lateral distributions measured in air showers by the KASCADE experiment," *Astropart. Phys.* **14** no. 4, (2001) 245–260.

[7] G. Battistoni *et al.*, "Cosmic-muon results from the NUSEX experiment," *Il Nuovo Cimento C* **9** no. 2, (1986) 196–209, 0390-5551.

[8] M. Ambrosio *et al.*, "Vertical muon intensity measured with MACRO at the Gran Sasso laboratory," *Phys. Rev. D* **52** no. 7, (1995) 3793–3802. http://link.aps.org/doi/10.1103/PhysRevD.52.3793.

[9] P. Kuusiniemi *et al.*, "Underground cosmic-ray experiment EMMA," *J. Phys.: Conf. Ser.* **409** no. 1, (2013) 012067. http://stacks.iop.org/1742-6596/409/i=1/a=012067.

[10] **HiRes** Collaboration, D. J. Bird *et al.*, "The Cosmic Ray spectrum observed by Fly's Eye," *Astrophys. J.* **424** (1994) 491–502.

[11] **Pierre Auger** Collaboration, R. W. Cronin, "The Pierre Auger Observatory Design Report (2^{nd} edition)," *Nucl. Phys. B, Proc. Suppl.* **28B** (1998) 213. http://www.auger.org.

[12] **KASCADE-Grande** Collaboration, W. D. Apel *et al.*, "The spectrum of high-energy cosmic rays measured with KASCADE-Grande," *Astrop. Phys.* **36** (2012) 183–194, arXiv:1206.3834 [astro-ph.HE].

[13] **Telescope Array** Collaboration, P. Tinyakov, "Latest results from the Telescope Array," *Nucl. Instrum. Meth. A* **742** no. 067, (2014) 29–34.

[14] C. Grupen *et al.*, "Measurements of the muon component of extensive air showers at 320 m.w.e. underground," *Nucl. Instrum. Meth.* **510** no. 1-2, (2003) 190–193.

[15] **DELPHI** Collaboration, J. Řidký and P. Travnicek, "Detection of muon bundles from cosmic ray showers by the DELPHI experiment," *Nucl. Phys. B, Proc. Suppl.* **138** (2005) 295–298.

[16] **L3** Collaboration, P. Achard *et al.*, "Measurement of the atmospheric muon spectrum from 20-GeV to 3000-GeV," *Phys. Lett.* **B598** (2004) 15–32, hep-ex/0408114 [nucl-ex].

[17] "LEP Design Report: Vol. 2. The LEP Main Ring," (1984) .

[18] S. Ostapchenko, "QGSJET-II: Towards reliable description of very high energy hadronic interactions," *Nucl. Phys. B, Proc. Suppl.* **151** (2006) 143–146, arXiv:hep-ph/0412332 [hep-ph].

[19] S. Ostapchenko, "Monte Carlo treatment of hadronic interactions in enhanced Pomeron scheme: I. QGSJET-II model," *Phys. Rev. D* **83** no. 1, (2011) 014018, arXiv:1010.1869 [hep-ph].

[20] D. Pacini, "La radiazione penetrante alla superficie ed in seno alle acque," *Nuovo Cim.* **Serie VI, Tomo 3** (1912) 93–100.

[21] V. F. Hess, "Über Beobachtungen der durchdringenden Strahlung bei sieben Freiballonfahrten," *Phys. Zeitschr.* **13** (1912) 1084–1091.

[22] R. A. Millikan and G. H. Cameron, "High frequency rays of cosmic origin," *Phys. Rev.* **28** no. 68, (1926) 851.

[23] W. Bothe and W. Kolhörster, "Das Wesen der Höhenstrahlung," *Phys. Zeitschr.* **56** (1929) 751–777.

[24] D. V. Skobelzyn, "Über eine Neue Art sehr schneller Beta-Strahlen," *Z. Phys.* **54** (1929) 686–703.

[25] P. Auger *et al.*, "Extensive Cosmic-Ray Showers," *Rev. Mod. Phys.* **11** (1939) 288.

[26] **Particle Data Group** Collaboration, S. Eidelman *et al.*, "Review of particle physics. Particle Data Group," *Phys. Lett. B* **592** (2004) 1–1109.

[27] S. P. Swordy, "The energy spectra and anisotropies of cosmic rays," *Space. Sci. Rev.* **99** (2001) 85–94.

[28] R. W. Clay, Z. Kurban, and N. R. Wild, "Cosmic Ray Related Undergraduate Experiments," *GAP Note 1998-061 (Technical and Scientific Notes about the Pierre Auger Project)* (1998) .

[29] J. W. Cronin, T. K. Gaisser, and S. P. Swordy, "Cosmic rays at the energy frontier," *Sci. Am.* **276** (1997) 32–37.

[30] J. Hörandel, "Models of the knee in the Energy Spectrum of Cosmic Rays," *Astropart. Phys.* **21** no. 3, (2004) 241–265, arXiv:astro-ph/0402356v2 [astro-ph].

[31] **Particle Data Group** Collaboration, J. Beringer *et al.*, "Review of Particle Physics (RPP)," *Phys. Rev. D.* **86** (2012) 010001.

[32] J. Simpson, "Elemental and isotopic composition of Galactic cosmic rays," *Annu. Rev. Nucl. Part. S.* **33** (1983) 323–381.

[33] A. A. Watson, "EARLY UNIVERSE: Cosmologists Celebrate the Death of Defects," *Science* **278** (1997) 574.

[34] **HiRes** Collaboration, D. J. Bird *et al.*, "Evidence for correlated changes in the spectrum and composition of cosmic rays at extremely high-energies," *Phys. Rev. Lett.* **71** (1993) 3401–3404.

[35] **HiRes** Collaboration, D. J. Bird *et al.*, "Detection of a cosmic ray with measured energy well beyond the expected spectral cutoff due to cosmic microwave radiation," *Astrophys. J.* **441** (1995) 144–150.

[36] D. Bindig, C. Bleve, and K.-H. Kampert, "Air shower development: impact of the LHC data," *Proceedings, 32nd International Cosmic Ray Conference (ICRC 2011)* **1** (2011) 161–164. http://inspirehep.net/record/1346047/files/v1_1284.pdf.

[37] **EAS-TOP** Collaboration, B. Alessandro, "Study of the composition around the knee through the electromagnetic and muon detectors data at EAS-TOP," *Proceedings of the 27th International Cosmic Ray Conference, Hamburg* **1** (2001) 124. http://galprop.stanford.edu/elibrary/icrc/2001/proceedings/ICRC2001/he_index.html.

[38] **EAS-TOP** Collaboration, M. Aglietta *et al.*, "The cosmic ray primary composition in the knee region through the EAS electromagnetic and muon measurements at EAS-TOP," *Astropart. Phys.* **21** (2004) 583–596.

[39] **EAS-TOP, MACRO** Collaboration, M. Bertaina, "The Proton, Helium and CNO Fluxes at $E_0 \cong 100$ TeV from the EAS-TOP (Cherenkov) and MACRO (TeV Muon) Data at the Gran Sasso Laboratories," *Proceedings of the 28th International Cosmic Ray Conference, Tsukuba* **1** (2003) 115–118. http://www-rccn.icrr.u-tokyo.ac.jp/icrc2003/PROCEEDINGS/PDF/29.pdf.

[40] **KASCADE** Collaboration, T. Antoni *et al.*, "KASCADE measurements of energy spectra for elemental groups of cosmic rays: Results and open problems," *Astropart. Phys.* **24** no. 1, (2005) 1–25, arXiv:astro-ph/0505413 [astro-ph].

[41] Y. A. Fomin *et al.*, "Nuclear composition of primary cosmic rays in the 'knee' region according MSU EAS array data," *J. Phys. G* **22** (1996) 1839–1849.

[42] O. A. Gress *et al.*, "The study of primary cosmic rays energy spectrum and mass composition in the energy range 0.5-50PeV with TUNKA

EAS Cherenkov array," *Nucl. Phys. B, Proc. Suppl.* **75** (1999) 299–301.

[43] L. Sveshnikova *et al.*, "Cosmic ray spectrum above the knee measured by the Tunka-133 experiment: special features and possible interpretations," *Proceedings of the 33th International Cosmic Ray Conference, Rio de Janeiro* (2014) 0304. http://www.cbpf.br/%7Eicrc2013/papers/icrc2013-0304.pdf.

[44] **AMANDA, SPASE** Collaboration, K. Rawlins, "Measurement of the cosmic ray composition at the knee with the SPASE-2/AMANDA-B10 detectors," *Proceedings of the 28th International Cosmic Ray Conference, Tsukuba* **1** (2003) 173–176. http://www-rccn.icrr.u-tokyo.ac.jp/icrc2003/PROCEEDINGS/PDF/44.pdf.

[45] M. A. K. Glasmacher *et al.*, "Energy spectra and composition near the knee," *Nucl. Phys. Proc. Suppl.* **75A** (1999) 241–243.

[46] **IceCube** Collaboration, T. K. Gaisser, "Primary spectrum and composition with IceCube/IceTop," *Cosmic Ray International Seminar: The status and the future of the UHE Cosmic Ray Physics in the post LHC era (CRIS 2015) Gallipoli, Italy, September 14-16, 2015* (2016) , arXiv:1601.06670 [astro-ph.HE]. http://www-rccn.icrr.u-tokyo.ac.jp/icrc2003/PROCEEDINGS/PDF/44.pdf.

[47] J. Hörandel, "On the knee in the energy spectrum of cosmic rays," *Astropart. Phys.* **19** no. 2, (2003) 193–220, arXiv:astro-ph/0210453 [astro-ph].

[48] E. G. Berezhko *et al.*, "Composition of cosmic rays accelerated in supernova remnants," *J. Exp. Theor. Phys.* **89** no. 3, (1999) 391–403. [Zh. Eksp. Teor. Fiz. 116, 737 (1999)].

[49] T. Stanev *et al.*, "Cosmic rays. IV. The spectrum and chemical composition above 10 GeV," *Astron. Astrophys.* **274** (1993) 902, astro-ph/9303006.

[50] K. Kobayakawa *et al.*, "Acceleration by oblique shocks at supernova remnants and cosmic ray spectra around the knee region," *Phys. Rev. D* **66** no. 8, (2002) 083004, astro-ph/0008209.

[51] L. G. Sveshnikova, "The knee in the Galactic cosmic ray spectrum and variety in Supernovae," *Astron. Astrophys.* **409** (2003) 799–807, astro-ph/0303159.

[52] S. P. Swordy, "Expectations for Cosmic Ray Composition Changes in the Region 10**14 to 10**16 eV," *Proceedings of the 24th International Cosmic Ray Conference, Rome* **2** (1995) 697.

[53] A. A. Lagutin *et al.*, "The "knee" in the primary cosmic ray spectrum as consequence of the anomalous diffusion of the particles in the fractal interstellar medium," *Nucl. Phys. B, Proc. Suppl.* **97** (2001) 267–270.

[54] V. S. Ptuskin *et al.*, "Diffusion and drift of very high energy cosmic rays in galactic magnetic fields," *Astron. Astrophys.* **268** no. 2, (1993) 726–735.

[55] S. Ogio and F. Kakimoto, "Advective Diffusion Propagation Model for Galactic Cosmic Rays above 10^{12} eV," *Proceedings of the 28th International Cosmic Ray Conference, Tsukuba* **1** (2003) 315–318. http://www-rccn.icrr.u-tokyo.ac.jp/icrc2003/PROCEEDINGS/PDF/80.pdf.

[56] J. Candia, S. Mollerach, and E. Roulet, "Cosmic ray spectrum and anisotropies from the knee to the second knee," *J. Cosmol. Astropart. Phys.* **5** (2003) 003, astro-ph/0302082.

[57] D. Kazanas and A. Nicolaidis, "Cosmic Ray "Knee": A Herald of New Physics?," *Proceedings of the 27th International Cosmic Ray Conference, Hamburg* **5** (2001) 1760–1763, arXiv:astro-ph/0103147 [astro-ph].

[58] D. Kazanas and A. Nicolaidis, "Letter: Cosmic Rays and Large Extra Dimensions," *Gen. Relat. Gravit.* **35** (2003) 1117–1123, hep-ph/0109247.

[59] M. Nagano and A. A. Watson, "Observations and implications of the ultrahigh-energy cosmic rays," *Rev. Mod. Phys.* **72** (2000) 689–732.

[60] K. Greisen, "End to the Cosmic-Ray Spectrum?," *Phys. Rev. Lett.* **16** (1966) 748–750.

[61] V. A. Kuzmin and G. T. Zatsepin, "On cosmic-ray interactions with protons," *Can. J. Phys.* **46** (1968) S617.

[62] R. A. Alpher, H. A. Bethe, and G. Gamow, "The Origin of Chemical Elements," *Phys. Rev.* **73** (1948) 803–804.

[63] A. A. Penzias and R. W. Wilson, "A Measurement of Excess Antenna Temperature at 4080 Mc/s," *Astrophys. J.* **142** (1965) 419–421.

[64] R. W. Clay, A. G. K. Smith, and J. L. Reid, "Cosmic ray induced noise in gravitational wave detectors," *Publ. Astron. Soc. Aust* **14** (1997) 195.

[65] A. Haungs *et al.*, "KCDC - The KASCADE Cosmic-ray Data Centre," *J. Phys. Conf. Ser.* **632** no. 1, (2015) , arXiv:1504.06696 [astro-ph.IM].

[66] **MASS91** Collaboration, R. Bellotti, "Balloon measurements of cosmic ray muon spectra in the atmosphere along with those of primary protons and helium nuclei over midlatitude," *Phys. Rev. D* **60** (1999) 052002, arXiv:hep-ex/9905012 [hep-ex].

[67] K. Greisen, "Cosmic Ray Showers," *Ann. Rev. Nucl. Sci.* **10** (1960) 63.

[68] M. Nagano *et al.*, "Energy spectrum of primary cosmic rays between $10^{14.5}$ and 10^{18} eV," *J. Phys. G* **10** (1984) 1295–1310.

[69] M. P. Pascale *et al.*, "Absolute spectrum and charge ratio of cosmic ray muons in the energy region from 0.2 GeV to 100 GeV at 600 m above sea level," *J. Geophys. Res-Space* **98** (1993) 3501–3507.

[70] P. K. F. Grieder, "Cosmic Rays at the Earth," *Elsevier Science* (2001) .

[71] S. Cecchini and M. Spurio, "Atmospheric muons: experimental aspects," *Geosci. Instrum. Method. Data Syst.* **1** (2012) 185–196, arXiv:1208.1171.

[72] B. C. Rastin, "An accurate measurement of the sea-level muon spectrum within the range 4 to 3000 GeV/c," *J. Phys. G Nucl. Part.* **10** (1984) 1609–1628.

[73] C. A. Ayre *et al.*, "Precise measurement of the vertical muon spectrum in the range 20-500 GeV/c," *J. Phys. G Nucl. Part.* **1** (1975) 584–600.

[74] H. Jokisch *et al.*, "Cosmic-ray muon spectrum up to 1 TeV at 75deg zenith angle," *Phys. Rev. D.* **19** (1979) 1368–1372.

[75] K. P. Beuermann and G. Wibberenz, "Secondary spectra of electrons and photons in the atmosphere," *Can. J. Phys.* **46** (1968) S1034.

[76] D. E. Groom *et al.*, "Muon stopping-power and range tables 10-MeV to 100-TeV," *Atom. Data Nucl. Data Tabl.* **78** (2001) 183–356.

[77] Y. Takahashi, "Elemental Abundance of High Energy Cosmic Rays," *Nucl. Phys. B, Proc. Suppl.* **60** (1998) 83–92.

[78] **RUNJOB** Collaboration, M. Hareyama *et al.*, "High Energy Galactic Cosmic Rays Observed by RUNJOB Experiment," *J. Phys. Conf. Ser.* **31** (2006) 159–160.

[79] **BESS** Collaboration, T. Sanuki, "Cosmic ray data and their interpretation: About BESS experiment," *Nucl. Phys. Proc. Suppl.* **175-176** (2008) 149–154.

[80] **CAPRICE** Collaboration, T. Mocchiutti, "Composition of cosmic ray particles in the atmosphere as measured by the CAPRICE98 balloon borne apparatus," *Proceedings of the 28th International Cosmic Ray Conference, Tsukuba* **1** (2003) 1627–1630.

[81] S. Coutu *et al.*, "Cosmic ray positrons: Are there primary sources?," *Astropart. Phys.* **11** (1999) 429–435, arXiv:astro-ph/9902162 [astro-ph].

[82] A. D. Panov, V. I. Zatsepin, and N. V. Sokolskaya, "Spectra of abundant nuclei in sources, according to the ATIC experiment," *Bull. Russ. Acad. Sci. Phys.* **79** no. 3, (2015) 285–288. [Izv. Ross. Akad. Nauk Ser. Fiz.79,no.3,318–321(2015)].

[83] **CREAM** Collaboration, H. S. Ahn *et al.*, "Measurements of the relative abundances of high-energy cosmic-ray nuclei in the TeV/nucleon region," *Astrophys. J* **715** (2010) 1400–1407.

[84] **PAMELA** Collaboration, W. Menn *et al.*, "PH, He, Li and Be Isotopes in the PAMELA-Experiment," *J. Phys. Conf. Ser.* **675** (2016) 032001.

[85] A. Chiavassa *et al.*, "KASCADE-Grande: The Grande array," *Proceedings of the 28th International Cosmic Ray Conference, Tsukuba* (2003) 989–992. http://www-rccn.icrr.u-tokyo.ac.jp/icrc2003/PROCEEDINGS/PDF/248.pdf.

[86] **Tibet ASgamma** Collaboration, M. Amenomori *et al.*, "Cosmic-ray energy spectrum around the knee observed with the Tibet air-shower experiment," *Astrophys. Space Sci. Trans.* **7** (2011) 15–20.

[87] **HiRes-MIA** Collaboration, T. Abu-Zayyad *et al.*, "Measurement of the cosmic ray energy spectrum and composition from 10**17-eV to 10**18.3-eV using a hybrid fluorescence technique," *Astrophys. J.* **557** (2001) 686, arXiv:astro-ph/0010652 [astro-ph].

[88] **AGASA** Collaboration, M. Takeda *et al.*, "Extension of the cosmic-ray energy spectrum beyond the predicted Greisen-Zatsepin-Kuzmin cutoff," *Phys. Rev. Lett.* **81** (1998) 1163, arXiv:astro-ph/9807193 [astro-ph].

[89] **HiRes** Collaboration, D. R. Bergman, "Observation of the GZK Cutoff by the HiRes Experiment," *Proceedings of the 30th International Cosmic Ray Conference* **4** (2007) 451–454. http://indico.nucleares.unam.mx/contributionDisplay.py?contribId=1128&confId=4.

[90] **AGASA** Collaboration, K. Shinozaki, "AGASA results," *Nucl. Phys. Proc. Suppl.* **151** (2006) 3–10.

[91] **Pierre Auger, Telescope Array** Collaboration, R. W. Cronin, "Pierre Auger Observatory and Telescope Array: Joint Contributions to the 34th International Cosmic Ray Conference (ICRC 2015)," *FERMILAB-CONF-15-495-AD-AE-CD-TD* (2015) , arXiv:1511.02103 [astro-ph.HE].

[92] **EAS-TOP, LVD** Collaboration, M. Aglietta *et al.*, "The high muon spectrum in Extensive Air Showers: first data from LVD and EAS-TOP at Gran Sasso," *Astrop. Phys.* **9** (1998) 185–192.

[93] **MACRO, EAS-TOP** Collaboration, M. Aglietta, M. Ambrosio, *et al.*, "The Primary cosmic ray composition between 10**15 and 10**16 eV

from extensive air showers electromagnetic and TeV muon data," *Astropart. Phys.* **20** (2004) 641–652, arXiv:astro-ph/0305325 [astro-ph].

[94] S. M. Kasahara *et al.*, "Study of cosmic ray composition in the knee region using multiple muon events in the Sudan 2 detector," *Phys. Rev. D* **55** (1997) 5282.

[95] V. N. Batakanov, R. V. Novoseltsev, and R. V. Novoseltseva, "Detection of muon groups with multiplicity $n_\mu > 1500$ at the Baksan underground scintillation telescope," *Astropart. Phys.* **8** (1997) 59–66.

[96] A. G. Bogdanov and other, "Energy spectrum of cosmic ray muons in 100 TeV energy region reconstructed from the BUST data," *Astropart. Phys.* **36** (2012) 224–236, arXiv:0911.1692 [astro-ph.HE].

[97] T. Enqvist *et al.*, "EMMA: A new underground cosmic-ray experiment," *Nucl. Phys. Proc. Suppl.* **175-176** (2008) 307–310.

[98] A. Ball *et al.*, "Search for cosmic ray coincidences with detectors in the LEP tunnel," *Astropart. Phys.* (1994) 513–523.

[99] **CMS** Collaboration, V. Khachatryan *et al.*, "Measurement of the charge ratio of atmospheric muons with the CMS detector," *Phys. Lett.* **B692** no. 2, (2010) 83–54.

[100] **CosmoALEPH** Collaboration, A. S. Müller, "Status of the COSMOLEP project," *Nucl. Phys. B, Proc. Suppl.* **52B** (1997) 261–263.

[101] V. Avati *et al.*, "Cosmic multi-muon events observed in the underground CERN-LEP tunnel with the ALEPH experiment," *Astropart. Phys.* **19** (2003) 513–523.

[102] N. N. Kalmykov and S. S. Ostapchenko, "The nucleus-nucleus interaction, nuclear fragmentation, and fluctuations of extensive air showers," *Phys. Atom. Nucl.* **56** no. 3, (1993) 346–353. Yad. Fiz. 56 (1993) 105-119.

[103] **DELPHI** Collaboration, J. Abdallah *et al.*, "Study of multi-muon bundles in cosmic ray showers detected with the DELPHI detector at

LEP," *Astropart. Phys.* **28** (2007) 273–286, arXiv:0706.2561 [astro-ph].

[104] O. C. Allkofer, W. D. Carstensen, and W. D. Day, "The absolute cosmic ray muon spectrum at sea level," *Phys. Lett. B.* **36** (1971) 425–427.

[105] **CMS** Collaboration, S. Chatrchyan *et al.*, "The CMS experiment at the CERN LHC," *JINST* **3** no. 8, (2008) S08001.

[106] P. A. Schreiner, J. Reichenbacher, and M. C. Goodman, "Interpretation of the underground muon charge ratio," *Astrop. Phys.* **32** no. 1, (2009) 61–71. http://www.sciencedirect.com/science/article/pii/S0927650509000875.

[107] **L3** Collaboration, B. Adeva *et al.*, "The construction of the L3 experiment," *Nucl. Instrum. Meth. A* **289** (1990) 35–102.

[108] A. Akindinov *et al.*, "Performance of the ALICE Time-Of-Flight detector at the LHC," *Eur. Phys. J. Plus* **128** no. 4, (2013) 44.

[109] E. Cuautle *et al.*, "ACORDE, The ALICE cosmic ray detector," *Proceedings of the 30th International Cosmic Ray Conference* **5** (2008) 1201–1204.

[110] R. Santoro *et al.*, "The ALICE Silicon Pixel Detector: readiness for the first proton beam," *J. Instrum.* **4** no. 03, (2009) P03023.

[111] **ALICE** Collaboration, "ALICE Technical Design Report of the Trigger, Data Acquisition, High-Level Trigger, Control System,". http://edms.cern.ch/document/456354/2.

[112] C. Richards-Serre, "Evaluation de la perte d'energie unitaire et du parcours pour des muons de 2 a 600-GeV dans un absorbant quelconque," *Technical Report* **CERN-71-18** (1971) .

[113] **ALICE** Collaboration, B. Abelev *et al.*, "Performance of the ALICE experiment at the CERN LHC," *Int. J. Mod. Phys. A* **29** no. 24, (2014) 1430044, arXiv:1402.4476 [nucl-ex].

[114] P. Billoir, "Progressive track recognition with a Kalman like fitting procedure," *Comput. Phys. Commun.* **57** (1989) 390–394.

[115] D. Heck *et al.*, "CORSIKA: A Monte Carlo code to simulate extensive air showers," *FZKA-6019* (1998) . http://bibliothek.fzk.de/zb/berichte/FZKA6019.pdf.

[116] **KASCADE** Collaboration, T. Antoni *et al.*, "The cosmic ray experiment KASCADE," *Nucl. Instr. Meth. A* **513** (2003) 490–510.

[117] D. Heck and T. Pierog, "Extensive air shower simulation with CORSIKA: A User's Guide (Version 6.99x from August 8, 2011),". http://www-ik.fzk.de/~corsika.

[118] D. Heck and T. Pierog, "Extensive air shower simulation with CORSIKA: A User's Guide (Version 7.350 from December, 2012),". http://www-ik.fzk.de/~corsika.

[119] J. Ranft, "DPMJET version II.5: Sampling of hadron hadron, hadron-nucleus and nucleus-nucleus interactions at accelerator and cosmic ray energies according to the two component dual parton model: Code manual," *SI-99-6* (1999) , arXiv:hep-ph/9911232 [hep-ph].

[120] K. Werner *et al.*, "Parton ladder splitting and the rapidity dependence of transverse momentum spectra in deuteron-gold collisions at RHIC," *Phys. Rev. C* **74** (2006) 044902, arXiv:hep-ph/0506232 [hep-ph].

[121] H. J. Drescher *et al.*, "Parton-Based Gribov-Regge Theory," *Phys. Rept.* **350** (2001) 93–289, arXiv:hep-ph/0007198 [hep-ph].

[122] R. S. Fletcher *et al.*, "SYBILL: An event generator for simulation of high-energy cosmic ray cascades," *Phys. Rev. D* **50** (1994) 5710–5731.

[123] K. Werner *et al.*, "Strings, pomerons, and the VENUS model of hadronic interactions at ultra relativistic energies," *Phys. Rept.* **232** (1993) 87–299.

[124] A. B. Kaidalov and K. A. Ter-Martirosyan, "Multiple production of hadrons at high-energies in the model of Quark-Gluon String," *Sov. J. Nucl. Phys.* **39** (1984) 979–1028. Yad. Fiz. 39 (1984) 1545-1558.

[125] S. Ostapchenko, "Air shower development: impact of the LHC data," *Proceedings, 32nd International Cosmic Ray Conference (ICRC 2011)*

2 (2011) 71.
http://inspirehep.net/record/1352304/files/v2_0681.pdf.

[126] R. Brun *et al.*, "GEANT Detector Description and Simulation Tool," *CERN Programming Library Long Writeup W5013* (1994) .